The Met Office Unified Model Global Atmosphere 7.0/7.1 and JULES Global Land 7.0 configurations

Walters, D., Baran, A. J., Boutle, I., Brooks, M., Earnshaw, P., Edwards, J., Furtado, K., Hill, P. ORCID: https://orcid.org/0000-0002-9745-2120, Lock, A., Manners, J., Morcrette, C., Mulcahy, J., Sanchez, C., Smith, C., Stratton, R., Tennant, W., Tomassini, L., Van Weverberg, K., Vosper, S., Willett, M., Browse, J., Bushell, A., Carslaw, K., Dalvi, M., Essery, R., Gedney, N., Hardiman, S., Johnson, B., Johnson, C., Jones, A., Jones, C., Mann, G., Milton, S., Rumbold, H., Sellar, A., Ujiie, M., Whitall, M., Williams, K. and Zerroukat, M. (2019) The Met Office Unified Model Global Atmosphere 7.0/7.1 and JULES Global Land 7.0 configurations. Geoscientific Model Development, 12 (5). pp. 1909-1963. ISSN 1991-9603 doi: https://doi.org/10.5194/gmd-12-1909-2019 Available at https://centaur.reading.ac.uk/83821/

Geosci. Model Dev., 12, 1909–1963, 2019
https://doi.org/10.5194/gmd-12-1909-2019

Geoscientific Model Development
Open Access
EGU

The Met Office Unified Model Global Atmosphere 7.0/7.1 and JULES Global Land 7.0 configurations

David Walters[1], Anthony J. Baran[1,2], Ian Boutle[1], Malcolm Brooks[1], Paul Earnshaw[1], John Edwards[1], Kalli Furtado[1], Peter Hill[3], Adrian Lock[1], James Manners[1], Cyril Morcrette[1], Jane Mulcahy[1], Claudio Sanchez[1], Chris Smith[1], Rachel Stratton[1], Warren Tennant[1], Lorenzo Tomassini[1], Kwinten Van Weverberg[1], Simon Vosper[1], Martin Willett[1], Jo Browse[4], Andrew Bushell[1], Kenneth Carslaw[7], Mohit Dalvi[1], Richard Essery[5], Nicola Gedney[6], Steven Hardiman[1], Ben Johnson[1], Colin Johnson[1], Andy Jones[1], Colin Jones[8], Graham Mann[7,8], Sean Milton[1], Heather Rumbold[1], Alistair Sellar[1], Masashi Ujiie[9], Michael Whitall[1], Keith Williams[1], and Mohamed Zerroukat[1]

[1]Met Office, FitzRoy Road, Exeter, EX1 3PB, UK
[2]School of Physics, Astronomy and Mathematics, University of Hertfordshire, Hatfield, AL10 9AB, UK
[3]Department of Meteorology, University of Reading, Reading, RG6 6BB, UK
[4]Centre for Geography, Society and the Environment, University of Exeter – Penryn Campus, Cornwall, TR10 9EZ, UK
[5]School of Geosciences, University of Edinburgh, Edinburgh, EH8 9XP, UK
[6]Met Office, Joint Centre for Hydrometeorological Research, Maclean Building, Wallingford, OX10 8BB, UK
[7]School of Earth and Environment, University of Leeds, Leeds, LS2 9JT, UK
[8]National Centre for Atmospheric Science, University of Leeds, Leeds, LS2 9JT, UK
[9]Numerical Prediction Division, Japan Meteorological Agency, 1-3-4 Otemachi, Chiyoda-ku, Tokyo 100-8122, Japan

Correspondence: David Walters (david.walters@metoffice.gov.uk)

Received: 15 November 2017 – Discussion started: 28 November 2017
Revised: 15 February 2018 – Accepted: 20 March 2018 – Published: 14 May 2019

Abstract. We describe Global Atmosphere 7.0 and Global Land 7.0 (GA7.0/GL7.0), the latest science configurations of the Met Office Unified Model (UM) and the Joint UK Land Environment Simulator (JULES) land surface model developed for use across weather and climate timescales. GA7.0 and GL7.0 include incremental developments and targeted improvements that, between them, address four critical errors identified in previous configurations: excessive precipitation biases over India, warm and moist biases in the tropical tropopause layer (TTL), a source of energy non-conservation in the advection scheme and excessive surface radiation biases over the Southern Ocean. They also include two new parametrisations, namely the UK Chemistry and Aerosol (UKCA) GLOMAP-mode (Global Model of Aerosol Processes) aerosol scheme and the JULES multi-layer snow scheme, which improve the fidelity of the simulation and were required for inclusion in the Global Atmosphere/Global Land configurations ahead of the 6th Coupled Model Intercomparison Project (CMIP6).

In addition, we describe the GA7.1 branch configuration, which reduces an overly negative anthropogenic aerosol effective radiative forcing (ERF) in GA7.0 whilst maintaining the quality of simulations of the present-day climate. GA7.1/GL7.0 will form the physical atmosphere/land component in the HadGEM3–GC3.1 and UKESM1 climate model submissions to the CMIP6.

1 Introduction

In this paper, we document the Global Atmosphere 7.0 configuration (GA7.0) of the Met Office Unified Model (UM; Brown et al., 2012) and the Global Land 7.0 configuration (GL7.0) of the Joint UK Land Environment Simulator (JULES) land surface model (Best et al., 2011; Clark et al., 2011). These are the latest iterations in the line of GA/GL configurations developed for use in global atmosphere/land and coupled modelling systems across weather and climate

timescales. This development is a continual process made up of small incremental changes to parameters and options within existing parametrisation schemes, the implementation of new schemes and options, and less frequent major changes to the structure of the model and the framework on which it is built. The Global Atmosphere 6.0 configuration (GA6.0; Walters et al., 2017) fell into the latter category, as it included a once-in-a-decade replacement of the model's dynamical core. To allow the configuration developers to concentrate on that change, the inclusion of other changes was limited to those that were known to be necessary alongside the dynamical core, or to significantly improve system performance measures, so as to make the dynamical core implementation easier. For this reason, GA7 sees the inclusion of a number of bottom-up developments to the atmospheric parametrisation schemes developed over several years that improve the fidelity and internal consistency of the model. These include an improved treatment of gaseous absorption in the radiation scheme, improvements to the treatment of warm rain and ice cloud, and an improvement to the numerics in the model's convection scheme. It also includes a number of top-down developments motivated by the findings of process evaluation groups (PEGs), which are tasked with understanding the root causes of model error. These changes include further developments in the model's microphysics and incremental improvements to our implementation of the dynamical core. In combination with the bottom-up developments discussed previously, these lead to large reductions in our four critical model errors, namely rainfall deficits over India during the South Asian monsoon, temperature and humidity biases in the tropical tropopause layer (TTL), deficiencies in the model's numerical conservation and surface flux biases over the Southern Ocean. Finally, GA7 and GL7 include new parametrisation schemes, which increase the complexity and fidelity of the model and introduce new functionality that was deemed necessary for the next generation climate modelling systems in which they will be used and which will form the UK's contribution to the 6th Coupled Model Intercomparison Project (CMIP6; Eyring et al., 2015). These new capabilities include a multi-moment modal representation of prognostic tropospheric aerosols, a multi-layer snow scheme and a seamless stochastic physics package, which will oversee the inclusion of stochastic physics terms in production UM climate simulations for the first time.

In Sect. 2 we describe GA7.0 and GL7.0, whilst in Sect. 3 we document how these differ from the last documented configurations: GA6.0 and GL6.0[1]. The development of these changes is documented using "trac" issue tracking software, so for consistency with that documentation, we list the trac ticket numbers (denoted by trac's # character) along with these descriptions. Section 4 includes an assessment of the configuration's performance in global weather prediction and atmosphere/land-only climate simulations. This illustrates the reduction of the critical model errors noted above, and highlights some improvements in simple weather prediction tests, but suggests that improvements are needed in the interaction between the model and its data assimilation before implementation for operational forecasting. In Sect. 5 we briefly describe GA7.1, which is based on the GA7.0 "trunk" configuration but includes a minimal set of changes for addressing the excessive aerosol forcing discussed in Sect. 4.5. As a result of this work, GA7.1 and GL7.0 are suitable for use as the physical atmosphere and land components in the HadGEM3–GC3.1 and UKESM1 climate models that will be submitted to the CMIP6.

2 Global Atmosphere 7.0 and Global Land 7.0

2.1 Dynamical formulation and discretisation

The UM's ENDGame dynamical core uses a semi-implicit semi-Lagrangian formulation to solve the non-hydrostatic, fully compressible deep-atmosphere equations of motion (Wood et al., 2014). The primary atmospheric prognostics are the three-dimensional wind components, virtual dry potential temperature, Exner pressure and dry density, whilst moist prognostics such as the mass mixing ratio of water vapour and prognostic cloud fields as well as other atmospheric loadings are advected as free tracers. These prognostic fields are discretised horizontally onto a regular longitude–latitude grid with Arakawa C-grid staggering (Arakawa and Lamb, 1977), whilst the vertical discretisation utilises a Charney–Phillips staggering (Charney and Phillips, 1953) using terrain-following hybrid height coordinates. The discretised equations are solved using a nested iterative approach centred about solving a linear Helmholtz equation. By convention, global configurations are defined on $2\times$ N longitudinal columns and $1.5\times$ N latitudinal rows of grid points for scalar variables, with the meridional wind variable held at the north and south poles and scalar and zonal wind variables first stored half a grid length away from the poles. This choice makes the grid-spacing approximately isotropic in the mid-latitudes and means that the integer N, which represents the maximum number of zonal 2 grid-point waves that can be represented by the model, uniquely defines its horizontal resolution; a model with $N = 96$ is said to have N96 resolution. Limited-area configurations use a rotated longitude–latitude grid with the pole rotated so that the grid's equator runs through the centre of the model domain. In the vertical, the majority of climate configurations

[1]Where the configurations remain unchanged from GA6.0/GL6.0 and their predecessors, Sect. 2 contains material which is unaltered from the documentation papers for those releases (i.e. Walters et al., 2011; Walters et al., 2014; Walters et al., 2017). In addition to the material herein, the Supplement to this paper includes a short list of model settings outside the GA/GL definition that are dependent on either model resolution or system application.

Table 1. Typical time step for a range of horizontal resolutions.

Grid	Nominal horizontal resolution	Typical time step
N96	135 km	20.0 min
N216	60 km	15.0 min
N320	40 km	12.0 min
N512	25 km	10.0 min
N640	20 km	7.5 min
N768	17 km	7.5 min
N1280	10 km	4.0 min

use an 85-level set labelled $\mathrm{L85}(50_\mathrm{t}, 35_\mathrm{s})_{85}$, which has 50 levels below 18 km (and hence at least sometimes in the troposphere), 35 levels above this (and hence solely in or above the stratosphere) and a fixed model lid 85 km above sea level. Limited-area climate simulations use a reduced 63-level set, $\mathrm{L63}(50_\mathrm{t}, 13_\mathrm{s})_{40}$, which has the same 50 levels below 18 km, with only 13 above and a lower model top at 40 km. Finally, numerical weather prediction (NWP) configurations use a 70-level set, $\mathrm{L70}(50_\mathrm{t}, 20_\mathrm{s})_{80}$ which has an almost identical 50 levels below 18 km and a model lid at 80 km but has a reduced stratospheric resolution compared to $\mathrm{L85}(50_\mathrm{t}, 35_\mathrm{s})_{85}$. Although we use a range of vertical resolutions in the stratosphere, a consistent tropospheric vertical resolution is currently used for a given GA configuration. A more detailed description of these level sets is included in the Supplement to this paper.

2.2 Structure of the atmospheric model time step

With ENDGame, the UM uses a nested iterative structure for each atmospheric time step within which processes are split into an outer loop and an inner loop. The semi-Lagrangian departure point equations are solved within the outer loop using the latest estimates for the wind variables. Appropriate fields are then interpolated to the updated departure points. Within the inner loop, the Coriolis, orographic and non-linear terms are solved along with a linear Helmholtz problem to obtain the pressure increment. Latest estimates for all variables are then obtained from the pressure increment via a back-substitution process; see Wood et al. (2014) for details. The physical parametrisations are split into slow processes (radiation, large-scale precipitation and gravity-wave drag – GWD) and fast processes (atmospheric boundary-layer turbulence, convection and land surface coupling). The slow processes are treated in parallel and are computed once per time step before the outer loop. The source terms from the slow processes are then added on to the appropriate fields before interpolation. The fast processes are treated sequentially and are computed in the outer loop using the latest predicted estimate for the required variables at the next, $n+1$ time step. A summary of the atmospheric time step is given in Algorithm 1. In practice two iterations are used for each of the outer and inner loops so that the Helmholtz problem is solved 4 times per time step. The prognostic aerosol scheme is included via a call to the UK Chemistry and Aerosol (UKCA) code after the main atmospheric time step; this call is currently performed once per hour. Finally, Table 1 contains the typical length of time step used for a range of horizontal resolutions.

Algorithm 1 Iterative structure of time step $n+1$. Here, we use two inner and two outer loops ($L = 2$, $M = 2$).

1: Given the solution at time step n, let the first estimate for a prognostic variable F at time level $n+1$ be $F^{n+1} = F^n$
2: Compute slow parametrised processes and time level n forcings R_F^n

3: **for** $m = 1, M$ **do** {*departure (outer-loop) iteration*}
4: Solve the trajectory equations to compute the next estimate of the departure points using the time level n and the latest estimate for time level $n+1$ wind fields
5: Interpolate R_F^n to departure points
6: Compute time level $n+1$ predictors F^*
7: Compute fast parametrised processes using latest $n+1$ predictor F^*
8: Evaluate time level n component of Helmholtz right hand side $\mathfrak{R}^n$

9: **for** $l = 1, L$ **do** {*non-linear (inner-loop) iteration*}
10: Evaluate non-linear and Coriolis terms R_F^*
11: Evaluate time level $n+1$ component of Helmholtz right hand side $\mathfrak{R}^*$
12: Solve the Helmholtz problem for the pressure increment π' and hence obtain the next estimate for $\pi^{n+1} \equiv \pi^n + \pi'$
13: Obtain the other prognostic variables at time level $n+1$ via back-substitution
14: **end for**

15: **end for**

2.3 Solar and terrestrial radiation

Shortwave (SW) radiation from the Sun is absorbed and reflected in the atmosphere and at the Earth's surface and provides energy to drive the atmospheric circulation. Longwave (LW) radiation is emitted from the planet and interacts with the atmosphere, redistributing heat, before being emitted into space. These processes are parametrised via the radiation scheme, which provides prognostic atmospheric temperature increments, prognostic surface fluxes and additional diagnostic fluxes. The SOCRATES (https://code.metoffice.gov.uk/trac/socrates, last access: 4 April 2019) radiative transfer scheme (Edwards and Slingo, 1996; Manners et al., 2015) is used with a new configuration for GA7. Solar radiation is treated in six SW bands and thermal radiation in nine LW bands, as outlined in Table 2. Gaseous absorption uses the correlated-k method with newly derived coefficients for all gases (except where indicated below) based on the HITRAN 2012 spectroscopic database (Rothman et al., 2013). Scaling of absorption coefficients uses a lookup table of 59

pressures with five temperatures per pressure level based around a mid-latitude summer profile. The method of equivalent extinction (Edwards, 1996; Amundsen et al., 2017) is used for minor gases in each band. The water vapour continuum is represented using laboratory results from the CAVIAR project (Continuum Absorption at Visible and Infrared wavelengths and its Atmospheric Relevance) between 1 and 5 µm (Ptashnik et al., 2011, 2012) and version 2.5 of the Mlawer–Tobin–Clough–Kneizys–Davies (MT_CKD-2.5) model (Mlawer et al., 2012) at other wavelengths.

Forty-one (41) k terms are used for the major gases in the SW bands. Absorption by water vapour (H_2O), carbon dioxide (CO_2), ozone (O_3), oxygen (O_2), nitrous oxide (N_2O) and methane (CH_4) is included. Ozone cross sections for the ultraviolet (UV) and visible bands come from Serdyuchenko et al. (2014) and Gorshelev et al. (2014), along with Brion–Daumont–Malicet (Daumont et al., 1992; Malicet et al., 1995) for the far UV. In the first SW band, a single k term is calculated for each 20 nm sub-interval from 200 to 320 nm, and in band 2, a single k term is calculated for each of the sub-intervals, 320–400 and 400–505 nm. This allows the incoming solar flux to be supplied on these finer wavelength bands for experiments concerning solar spectral variability. The solar spectrum uses data from the Naval Research Laboratory Solar Spectral Irradiance model (NRLSSI; Lean et al., 2005) as recommended by the SPARC/SOLARIS (Solar Influences for SPARC: Stratospheric Processes and their Role in Climate; http://solarisheppa.geomar.de/ccmi, last access: 4 April 2019) group. A mean solar spectrum for the period 2000–2011 is used when a varying spectrum is not invoked.

Eighty-one (81) k terms are used for the major gases in the LW bands. Absorption by H_2O, O_3, CO_2, CH_4, N_2O, CFC-11 (CCl_3F), CFC-12 (CCl_2F_2) and HFC134a (CH_2FCF_3) is included. For climate simulations, the atmospheric concentrations of CFC-12 and HFC134a are adjusted to represent absorption by all the remaining trace halocarbons. The treatment of CO_2 absorption for the peak of the 15 µm band (LW band 4) is as described in Zhong and Haigh (2000). An improved representation of CO_2 absorption in the "window" region (8–13 µm) provides a better forcing response to increases in CO_2 (Pincus et al., 2015). The method of "hybrid" scattering is used in the LW, which runs full scattering calculations for 27 of the major gas k terms (where their nominal optical depth is less than 10 in a mid-latitude summer atmosphere). For the remaining 54 k terms (optical depth > 10) much cheaper non-scattering calculations are run.

Of the major gases considered, only H_2O is prognostic; O_3 uses a zonally symmetric climatology, whilst other gases are prescribed using either fixed or time-varying mass mixing ratios and are assumed to be well mixed.

Absorption and scattering by the following prognostic aerosol species are included in both the SW and LW using the UKCA-Radaer scheme: sulfate, black carbon, organic carbon and sea salt. The aerosol scattering and absorption coefficients and asymmetry parameters are pre-computed for a wide range of plausible Mie parameters and stored in lookup tables for use during run time when the atmospheric chemical composition, including the mean aerosol particle radius and water content, are known. As the aerosol species are internally mixed within the modal aerosol scheme (see Table 4) the refractive indices of each mode are calculated online as a volume-weighted mean of the component species contributing to that mode. The component refractive indices are documented in the Appendix of Bellouin et al. (2013). Nucleation mode particles are neglected, as they are not expected to contribute significantly to the atmospheric optical properties. The parametrisation of cloud droplets is described in Edwards and Slingo (1996) using the method of "thick averaging". Padé fits are used for the variation with effective radius, which is computed from the number of cloud droplets. In configurations using prognostic aerosol, cloud droplet number concentrations are not calculated within the radiation scheme itself but are calculated by the UKCA-Activate scheme (West et al., 2014), which is based on the activation scheme of Abdul-Razzak and Ghan (2000). Note that in simulations using climatological rather than prognostic aerosol, the approach described here is not yet available, and instead we use CLASSIC (Coupled Large-scale Aerosol Simulator for Studies in Climate; Bellouin et al., 2011) aerosol climatologies and the calculation of optical properties and cloud droplet concentrations described in Sect. 2.3 of Walters et al. (2017). Both prognostic and climatological simulations of mineral dust also use the CLASSIC scheme. This is discussed in more detail in Sect. 3.8. The parametrisation of ice crystals is described in Baran et al. (2016). Full treatment of scattering is used in both the SW and LW. The sub-grid cloud structure is represented using the Monte Carlo independent column approximation (McICA) as described in Hill et al. (2011), with the parametrisation of sub-grid-scale water content variability described in P. G. Hill et al. (2015).

Full radiation calculations are made every hour using the instantaneous cloud fields and a mean solar zenith angle for the following 1 h period. Corrections are made for the change in solar zenith angle on every model time step as described in Manners et al. (2009). The emissivity and the albedo of the surface are set by the land surface model. The direct SW flux at the surface is corrected for the angle and aspect of the topographic slope as described in Manners et al. (2012).

2.4 Large-scale precipitation

The formation and evolution of precipitation due to grid scale processes is the responsibility of the large-scale precipitation – or microphysics – scheme, whilst small-scale precipitating events are handled by the convection scheme. The microphysics scheme has prognostic input fields of temperature, moisture, cloud and precipitation from the end of the previous time step, which it modifies in turn. The microphysics used is a single-moment scheme based on Wilson and Ballard (1999), with extensive modifications. The warm rain

Table 2. Spectral bands for the treatment of incoming solar (SW) radiation (left) and thermal (LW) radiation (right).

SW Band	Wavelength (nm)	LW Band	Wave number (cm^{-1})	Wavelength (μm)
1	200–320	1	1–400	25–10 000
2	320–505	2	400–550	18.18–25
3	505–690	3	550–590 and 750–800	12.5–13.33 and 16.95–18.18
4	690–1190	4	590–750	13.33–16.95
5	1190–2380	5	800–990 and 1120–1200	8.33–8.93 and 10.10–12.5
6	2380–10 000	6	990–1120	8.93–10.10
–	–	7	1200–1330	7.52–8.33
–	–	8	1330–1500	6.67–7.52
–	–	9	1500–2995	3.34–6.67

scheme is based on Boutle et al. (2014b) and includes a prognostic rain formulation, which allows three-dimensional advection of the precipitation mass mixing ratio and an explicit representation of the effect of sub-grid variability on autoconversion and accretion rates (Boutle et al., 2014a). We use the rain-rate-dependent particle size distribution of Abel and Boutle (2012) and fall velocities of Abel and Shipway (2007), which combine to allow a better representation of the sedimentation and evaporation of small droplets. We also make use of multiple sub-time steps of the precipitation scheme, with one call to the scheme for every 2 minutes of the model time step. This is required to achieve a realistic treatment of in-column evaporation. With prognostic aerosol, we use the UKCA-Activate aerosol activation scheme (West et al., 2014) to provide the cloud droplet number for autoconversion, where only soluble aerosol species (which can be composed of sulfate, sea salt, black carbon and organic carbon) contribute to the droplet number. When using climatological aerosol, the cloud droplet number is the same as that used in the radiation scheme. Ice cloud parametrisations use the generic size distribution of Field et al. (2007) and mass–diameter relations of Cotton et al. (2013).

2.5 Large-scale cloud

Cloud appears on sub-grid scales well before the humidity averaged over the size of a model grid box reaches saturation. A cloud parametrisation scheme is therefore required to determine the fraction of the grid box which is covered by cloud and the amount and phase of condensed water contained in this cloud. The formation of cloud will convert water vapour into liquid or ice and release latent heat. The cloud cover and liquid and ice water contents are then used by the radiation scheme to calculate the radiative impact of the cloud and by the large-scale precipitation scheme to calculate whether any precipitation has formed.

The parametrisation used is the prognostic cloud fraction and prognostic condensate (PC2) scheme (Wilson et al., 2008a, b) along with the cloud erosion parametrisation described by Morcrette (2012) and critical relative humidity parametrisation described in Van Weverberg et al. (2016). PC2 uses three prognostic variables for the water mixing ratio – vapour, liquid and ice – and a further three prognostic variables for the cloud fraction – liquid, ice and mixed phase. The following atmospheric processes can modify the cloud fields: SW radiation, LW radiation, boundary-layer processes, convection, precipitation, small-scale mixing (cloud erosion), advection and changes in atmospheric pressure. The convection scheme calculates increments to the prognostic liquid and ice water contents by detraining condensate from the convective plume, whilst the cloud fractions are updated using the non-uniform forcing method of Bushell et al. (2003). One advantage of the prognostic approach is that cloud can be transported away from where it was created. For example, anvils detrained from convection can persist and be advected downstream long after the convection itself has ceased. The radiative impact of convective cores, which hold condensate not detrained into the environment, is represented by diagnosing a convective cloud amount (CCA) and convective cloud water (CCW) where the convection is active on a particular time step. The CCA and CCW then get combined with the PC2 cloud fraction and condensate variables before these get passed to McICA to calculate the radiative impact of the combined cloud fields. Finally, the production of supercooled liquid water in a turbulent environment is parametrised following Furtado et al. (2016).

2.6 Sub-grid orographic drag

The effect of local and mesoscale orographic features not resolved by the mean orography, from individual hills to small mountain ranges, must be parametrised. The smallest scales, where buoyancy effects are not important, are represented by an effective roughness parametrisation in which the roughness length for momentum is increased above the surface roughness to account for the additional stress due to the sub-grid orography (Wood and Mason, 1993). The effects of the remainder of the sub-grid orography (on scales where buoyancy effects are important) are parametrised by a drag scheme which represents the effects of low-level-flow block-

ing and the drag associated with stationary gravity waves (mountain waves). This is based on the scheme described by Lott and Miller (1997) but with some important differences, described in more detail in Vosper (2015).

The sub-grid orography is assumed to consist of uniformly distributed elliptical mountains within the grid box, described in terms of a height amplitude, which is proportional to the grid-box standard deviation of the source orography data, anisotropy (the extent to which the sub-grid orography is ridge like, as opposed to circular), the alignment of the major axis and the mean slope along the major axis. The scheme is based on two different frameworks for the drag mechanisms: bluff body dynamics for the flow-blocking and linear gravity waves for the mountain-wave drag component.

The degree to which the flow is blocked and so passes around, rather than over the mountains is determined by the Froude number, $F = U/(NH)$ where H is the assumed sub-grid mountain height (proportional to the sub-grid standard deviation of the source orography data) and N and U are respectively measures of the buoyancy frequency and wind speed of the low-level flow. When F is less than the critical value, F_c, a fraction of the flow is assumed to pass around the sides of the orography, and a drag is applied to the flow within this blocked layer. Mountain waves are generated by the remaining proportion of the layer which the orography pierces through. The acceleration of the flow due to wave stress divergence is exerted at levels where wave breaking is diagnosed. The kinetic energy dissipated through the flow-blocking drag, the mountain-wave drag and the non-orographic gravity-wave drag (see Sect. 2.7 below) is returned to the atmosphere as a local heating term.

2.7 Non-orographic gravity-wave drag

Non-orographic sources – such as convection, fronts and jets – can force gravity waves with non-zero phase speed. These waves break in the upper stratosphere and mesosphere, depositing momentum, which contributes to driving the zonal mean wind and temperature structures away from radiative equilibrium. Waves on scales too small for the model to sustain explicitly are represented by a spectral sub-grid parametrisation scheme (Scaife et al., 2002), which by contributing to the deposited momentum leads to a more realistic tropical quasi-biennial oscillation (QBO). The scheme, described in more detail in Walters et al. (2011), represents processes of wave generation, conservative propagation and dissipation by critical-level filtering and wave saturation acting on a vertical wave number spectrum of gravity-wave fluxes following Warner and McIntyre (2001). Momentum conservation is enforced at launch in the lower troposphere, where isotropic fluxes guarantee zero net momentum, and by imposing a condition of zero vertical wave flux at the model's upper boundary. In between, momentum deposition occurs in each layer where reduced integrated flux results from erosion of the launch spectrum, after transformation by conservative propagation, to match the locally evaluated saturation spectrum.

2.8 Atmospheric boundary layer

Turbulent motions in the atmosphere are not resolved by global atmospheric models but are important to parametrise in order to give realistic vertical structure in the thermodynamic and wind profiles. Although referred to as the "boundary-layer" scheme, this parametrisation represents mixing over the full depth of the troposphere. The scheme is that of Lock et al. (2000) with the modifications described in Lock (2001) and Brown et al. (2008). It is a first-order turbulence closure mixing adiabatically conserved heat and moisture variables, momentum and tracers. For unstable boundary layers, diffusion coefficients (K profiles) are specified functions of height within the boundary layer, related to the strength of the turbulence forcing. Two separate K profiles are used, one for surface sources of turbulence (surface heating and wind shear) and one for cloud-top sources (radiative and evaporative cooling). The existence and depth of unstable layers is diagnosed initially by two moist adiabatic parcels, one released from the surface, the other from cloud-top. The top of the K profile for surface sources and the base of that for cloud-top sources are then adjusted to ensure that, from the resultant buoyancy flux, the magnitude of the buoyancy consumption of turbulence kinetic energy is limited to a specified fraction of buoyancy production, integrated across the boundary layer. This can permit the cloud layer to decouple from the surface (Nicholls, 1984). This same energetic diagnosis is used to limit the vertical extent of the surface-driven K profile when cumulus convection is diagnosed (through comparison of cloud and sub-cloud layer moisture gradients), except that in this case no condensation is included in the diagnosed buoyancy flux because that part of the distribution is handled by the convection scheme (which is triggered at the cloud base). Mixing across the top of the boundary layer is through an explicit entrainment parametrisation that can either be resolved across a diagnosed inversion thickness or, if too thin, is coupled to the radiative fluxes and the dynamics through a sub-grid inversion diagnosis. If the thermodynamic conditions are right, cumulus penetration into a stratocumulus layer can generate additional turbulence and cloud-top entrainment in the stratocumulus by enhancing evaporative cooling at the cloud top. There are additional non-local fluxes of heat and momentum in order to generate more vertically uniform potential temperature and wind profiles in convective boundary layers. Primarily for stable boundary layers and in the free troposphere, diffusion coefficients are also calculated using a local Richardson number scheme based on Smith (1990), with the final coefficients being the maximum of this and the non-local ones described above. The stability dependence in unstable boundary layers uses the "conventional function" of Brown (1999) that gives only weak enhancement over neu-

tral mixing, as we expect the non-local scheme to be most appropriate in this regime. The stability dependence in stable boundary layers is given by the "sharp" function over sea and by the "MES-tail" function over land (which matches linearly between an enhanced mixing function at the surface and "sharp" at 200 m and above), as defined in Brown et al. (2008). This additional near-surface mixing is motivated by the effects of surface heterogeneity, such as those described in McCabe and Brown (2007). The resulting diffusion equation is solved implicitly using the monotonically damping, second-order-accurate, unconditionally stable numerical scheme of Wood et al. (2007). The kinetic energy dissipated through the turbulent shear stresses is returned to the atmosphere as a local heating term.

2.9 Convection

The convection scheme represents the sub-grid-scale transport of heat, moisture and momentum associated with cumulus cloud within a grid box. The UM uses a mass-flux convection scheme based on Gregory and Rowntree (1990) with various extensions to include down-draughts (Gregory and Allen, 1991) and convective momentum transport (CMT). The current scheme consists of three stages: (i) convective diagnosis to determine whether convection is possible from the boundary layer; (ii) a call to the shallow or deep convection scheme for all points diagnosed deep or shallow by the first step; and (iii) a call to the mid-level convection scheme for all grid points.

The diagnosis of shallow and deep convection is based on an undilute parcel ascent from the near surface for grid boxes where the surface buoyancy flux is positive and forms part of the boundary-layer diagnosis (Lock et al., 2000). Shallow convection is then diagnosed if the following conditions are met: (i) the parcel attains neutral buoyancy below 2.5 km or below the freezing level, whichever is higher, and (ii) the air in model levels forming a layer of the order of 1500 m above this has a mean upward vertical velocity less than $0.02\,\mathrm{m\,s^{-1}}$. Otherwise, convection diagnosed from the boundary layer is defined as deep.

The deep convection scheme differs from the original Gregory and Rowntree (1990) scheme in using a convective available potential energy (CAPE) closure based on Fritsch and Chappell (1980). Mixing detrainment rates now depend on relative humidity (RH) and forced detrainment rates adapt to the buoyancy of the convective plume (Derbyshire et al., 2011). The CMT scheme uses a flux gradient approach (Stratton et al., 2009).

The shallow convection scheme uses a closure based on Grant (2001) and has larger entrainment rates than the deep scheme consistent with cloud-resolving model (CRM) simulations of shallow convection. The shallow CMT uses flux–gradient relationships derived from CRM simulations of shallow convection (Grant and Brown, 1999).

The mid-level scheme operates on any instabilities found in a column above the top of deep or shallow convection or above the lifting condensation level (LCL). The scheme is largely unchanged from Gregory and Rowntree (1990), but uses the Gregory et al. (1997) CMT scheme and a CAPE closure. The mid-level scheme operates mainly either overnight over land when convection from the stable boundary layer is no longer possible or in the region of mid-latitude storms. Other cases of mid-level convection tend to remove instabilities over a few levels and do not produce much precipitation.

The timescale for the CAPE closure, which is used for deep and mid-level convection schemes, varies according to the large-scale vertical velocity. The values used vary from the shortest value equal to the convection time step when the ascent is strongest, with a maximum of either 4 h for mid-level convection or a minimum of either 4 h or a timescale from a surface flux closure for deep convection.

2.10 Atmospheric aerosols and chemistry

As discussed in Walters et al. (2011), the precise details of the modelling of atmospheric aerosols and chemistry is considered as a separate component of the full Earth system and remains outside the scope of this document. The aerosol species represented and their interaction with the atmospheric parametrisations is, however, part of the Global Atmosphere component and is therefore included. Systems including prognostic aerosol modelling do so using the GLOMAP-mode (Global Model of Aerosol Processes) aerosol scheme described in Mann et al. (2010), which is included in the UM as part of the UKCA coupled chemistry and aerosol code. The scheme simulates speciated aerosol mass and number in 4 soluble modes covering the sub-micron to super-micron aerosol size ranges (nucleation, Aitken, accumulation and coarse modes) as well as an insoluble Aitken mode. The prognostic aerosol species represented are sulfate, black carbon, organic carbon and sea salt. For more details see Sect. 3.8. Mineral dust is simulated using the CLASSIC dust scheme described in Woodward (2011). Systems not including prognostic aerosols use a three-dimensional monthly climatology for each aerosol species to model both the direct and indirect aerosol effects. Ideally, this should use the same aerosol species and parametrisation of the direct and indirect aerosol effects as we use for the prognostic scheme. As this capability has not yet been developed for GLOMAP-mode, however, we continue to use climatologies based on the CLASSIC aerosol scheme (Bellouin et al., 2011) as described in Walters et al. (2017). In addition to the treatment of these tropospheric aerosols, we include a simple stratospheric aerosol climatology based on Cusack et al. (1998). We also include the production of stratospheric water vapour via a simple methane oxidation parametrisation (Untch and Simmons, 1999).

2.11 Land surface and hydrology: Global Land 7.0

The exchange of fluxes between the land surface and the atmosphere is an important mechanism for heating and moistening the atmospheric boundary layer. In addition, the exchange of CO_2 and other greenhouse gases plays a significant role in the climate system. The hydrological state of the land surface contributes to impacts such as flooding and drought as well as providing freshwater fluxes to the ocean, which influences ocean circulation. Therefore, a land surface model needs to be able to represent this wide range of processes over all surface types that are present on the Earth.

The Global Land configuration uses a community land surface model, JULES (Best et al., 2011; Clark et al., 2011), to model all of the processes at the land surface and in the subsurface soil. A tile approach is used to represent sub-grid-scale heterogeneity (Essery et al., 2003b), with the surface of each land grid box subdivided into five types of vegetation (broadleaf trees, needle-leaved trees, temperate C_3 grass, tropical C_4 grass and shrubs) and four non-vegetated surface types (urban areas, inland water, bare soil and land ice). The ground beneath the vegetation is coupled to the vegetation canopy by longwave radiation and turbulent sensible heat exchanges. JULES also uses a canopy radiation scheme to represent the penetration of light within the vegetation canopy and its subsequent impact on photosynthesis (Mercado et al., 2007). The canopy also interacts with falling snow. Snow buries the canopy for most vegetation types, but the interception of snow by needle-leaved trees is represented with separate snow stores on the canopy and on the ground. This impacts the surface albedo, the snow sublimation and the snowmelt (Essery et al., 2003a). The vegetation canopy code has been adapted for use with the urban surface type by defining an "urban canopy" with the thermal properties of concrete (Best, 2005). This has been demonstrated to give improvements over representing an urban area as a rough bare soil surface. Similarly, this canopy approach has also been adopted for the representation of lakes. The original representation was through a soil surface that could evaporate at the potential rate (i.e. a permanently saturated soil), which has been shown to have incorrect seasonal and diurnal cycles for the surface temperature (Rooney and Jones, 2010). By defining an "inland water canopy" and setting the thermal characteristics to those of a suitable mixed layer depth of water (≈ 5 m), a better diurnal cycle for the surface temperature is achieved.

Surface fluxes are calculated separately on each tile using surface similarity theory. In stable conditions we use the similarity functions of Beljaars and Holtslag (1991), whilst in unstable conditions we take the functions from Dyer and Hicks (1970). The effects on surface exchange of both boundary-layer gustiness (Godfrey and Beljaars, 1991) and deep convective gustiness (Redelsperger et al., 2000) are included. Temperatures at 1.5 m and winds at 10 m are interpolated between the model's grid levels using the same similarity functions, but a parametrisation of transitional decoupling in very light winds is included in the calculation of the 1.5 m temperature.

SW radiation fluxes use a "first guess" snow-free albedo for each land surface type, which can then be nudged towards an imposed grid-box mean value taken from a climatology. This nudging is neither performed in climate change simulations nor in any other simulations with dynamic vegetation. The grid-box mean albedo of the land surface is further modified in the presence of snow. The albedo of the ocean surface is a function of the wavelength, the solar zenith angle, the 10 m wind speed and the chlorophyll content according to the Jin et al. (2011) parametrisation. The emitted LW radiation is calculated using a prescribed emissivity for each surface type.

Soil processes are represented using a four-layer scheme for the heat and water fluxes with hydraulic relationships taken from van Genuchten (1980). These four soil layers have thicknesses from the top down of 0.1, 0.25, 0.65 and 2.0 m. The impact of moisture on the thermal characteristics of the soil is represented using a simplification of Johansen (1975), as described in Dharssi et al. (2009). The energetics of water movement within the soil is accounted for, as is the latent heat exchange resulting from the phase change of soil water from liquid to solid states. Sub-grid-scale heterogeneity of soil moisture is represented using the large-scale hydrology approach (Gedney and Cox, 2003), which is based on the topography-based rainfall–runoff model TOPMODEL (Beven and Kirkby, 1979). This enables the representation of an interactive water table within the soil that can be used to represent wetland areas and increases surface runoff through heterogeneity in soil moisture driven by topography.

A river routing scheme is used to route the total runoff from inland grid points both out to the sea and to inland basins, where it can flow back into the soil moisture. Outflow at inland basin points with saturated soils is distributed evenly across all sea outflow points. In coupled model simulations the resulting freshwater outflow is passed to the ocean, where it is an important component of the thermohaline circulation, whilst in atmosphere/land-only simulations this ocean outflow is purely diagnostic. River routing calculations are performed using the TRIP (Total Runoff Integrating Pathways) model (Oki and Sud, 1998), which uses a simple advection method (Oki, 1997) to route total runoff along prescribed river channels on a $1^\circ \times 1^\circ$ grid using a 3 h time step. Land surface runoff accumulated over this time step is mapped onto the river routing grid prior to the TRIP calculations, after which soil moisture increments and total outflow at river mouths are mapped back to the atmospheric grid (Falloon and Betts, 2006). This river routing model is not currently being used in limited-area or NWP implementations of the Global Atmosphere/Global Land.

2.12 Stochastic physics

A key component of many ensemble prediction systems (EPSs) is the use of stochastic physics schemes to represent model error emerging from unrepresented or coarsely resolved processes such as numerical diffusion or fluctuations in the impact of physical parametrisations on the large-scale fields. The addition of unresolved variability around the deterministic solution adds spread between ensemble members and has been shown to improve ensemble predictions in the medium range (Palmer et al., 2009; Tennant et al., 2011) as well as on seasonal (Weisheimer et al., 2011) and decadal timescales (Doblas-Reyes et al., 2009). The increase in the model's internal variability also helps to improve the model's climatology, through a noise-drift-induced process. In particular, there is strong evidence of the positive impact of stochastic physics schemes on specific processes such as mid-latitude blocking (Berner et al., 2012), the Madden–Julian Oscillation (MJO; Madden and Julian, 1971; Weisheimer et al., 2014) and North Atlantic weather regimes (Dawson and Palmer, 2015).

In GA7, we use a standardised package of stochastic physics schemes (Sanchez et al., 2016) based on an improved version of the stochastic kinetic energy backscatter scheme version 2 (SKEB2; Tennant et al., 2011) and the stochastic perturbation of tendencies scheme (SPT) with additional constraints designed to conserve energy and water. SKEB2 adds forcing to the large-scale flow to represent the backscatter of small-scale kinetic energy lost via numerical diffusion, whilst the SPT stochastically scales the output of physical parametrisations to represent variability about their mean predictions. Despite the positive impact of these stochastic physics schemes on EPS and climate model performance, their formulation lacks a sound physical basis. For this reason, these schemes are not used in deterministic forecast systems, which are designed to forecast the best possible single prediction of the atmosphere's future state.

2.13 Global atmospheric energy correction

Long climate simulations of the Unified Model include an energy correction scheme, designed to ensure that numerical errors, inconsistent geometric assumptions and missing processes do not lead to any spurious drift in the atmosphere's total energy. The scheme accumulates the net flux of energy through the upper and lower boundaries of the atmosphere over a period of 1 day and calculates the difference between this and the change in the atmosphere's internal energy. Any drift is compensated by the addition of a globally uniform temperature increment, which is applied at every time step for the following day. In GA7, the magnitude of these corrections is typically $\lesssim 0.6\,\mathrm{W\,m^{-2}}$.

2.14 Ancillary files and forcing data

In the UM, the characteristics of the lower boundary, the values of climatological fields, and the distribution of natural and anthropogenic emissions are specified using ancillary files. Use of correct ancillary file inputs can play as important a role in the performance of a system as the correct choice of many options in the parametrisations described above. For this reason, we consider the source data and processing required to create ancillaries as part of the definition of the Global Atmosphere/Global Land configurations.

Table 3 contains the main ancillaries used as well as references to the source data from which they are created.

3 Developments since Global Atmosphere/Global Land 6.0

The previous section provides a general description of all of the GA7.0 and GL7.0 configurations. In this section, we describe in more detail how these configurations differ from the previously documented configurations of GA6.0 and GL6.0.

3.1 Dynamical formulation and discretisation

3.1.1 Cubic Hermite interpolation and improved conservative advection for moist prognostics (GA ticket #135)

In GA6, the semi-Lagrangian interpolation to the departure point for moist prognostic variables was performed via bicubic interpolation in the horizontal and quintic interpolation in the vertical. The latter choice is one that has been made in global UM configurations for some time and was originally chosen to improve the fit to sharp discontinuities around the tropopause. For ENDGame's prognostic temperature variable, virtual dry potential temperature, the vertical interpolation used a cubic Hermite formulation, which it still uses in GA7. This is formed by matching the data and its derivative at the two levels closest to the departure point (rather than using the data at the four closest levels) and results in a spline interpolation with a continuous first derivative. The derivatives are estimated by fitting a quadratic polynomial to the data on three consecutive levels and evaluating its derivative at the central level. Formally, this is lower order than quintic (or even cubic Lagrange) interpolation, so the solution will be less accurate in general. The continuity of the first derivative, however, gives advection increments that correctly cancel under small amplitude oscillatory displacement in regions of strong gradients, such as at the tropopause. In GA7, we apply this same vertical interpolation algorithm to all moist prognostic variables. The impact of this change is marked as "q vertical interpolation – advection" in Fig. 7 of Hardiman et al. (2015), which shows that in an atmosphere/land-only climate simulation at N96 horizontal resolution (≈ 135 km in the mid-latitudes), this reduces

Table 3. Source datasets used to create standard ancillary files used in GA7.0/GL7.0.

Ancillary field	Source data	Notes
Land mask and fraction	System dependent	
Mean and sub-grid orography	GLOBE 30″; Hastings et al. (1999)	Fields filtered before use
Land usage	IGBP; Loveland et al. (2000)	Mapped to nine tile types
Soil properties	HWSD; Nachtergaele et al. (2008) STATSGO; Miller and White (1998) ISRIC-WISE; Batjes (2009)	Three datasets blended via optimal interpolation
Leaf area index	MODIS collection 5	4 km data (Samanta et al., 2012) mapped to five plant types
Plant canopy height	IGBP; Loveland et al. (2000)	Derived from land usage and mapped to five plant types
Bare soil albedo	MODIS; Houldcroft et al. (2008)	
Snow-free surface albedo	GlobAlbedo; Muller et al. (2012)	Spatially complete white sky values
TOPMODEL topographic index	Marthews et al. (2015)	
SST and sea ice	System or experiment dependent	
Sea surface chlorophyll content	GlobColour; Ford et al. (2012)	
Ozone	SPARC-II; Cionni et al. (2011)	Zonal mean field used[a]
GLOMAP-mode emissions and fields		Only required for prognostic aerosol simulations
Main primary emissions	CMIP5; Lamarque et al. (2010)	Includes SO_2, DMS (land), black carbon from fossil fuel, organic carbon from fossil fuel
Biomass burning	GFED3.1; van der Werf et al. (2010)	10-year monthly means
Volcanic SO_2 emissions	Andres and Kasgnoc (1998)	
Gas-phase aerosol precursors	UKCA tropospheric chemistry simulations O'Connor et al. (2014)	
Ocean DMS concentrations	Kettle et al. (1999)	
CLASSIC aerosol climatologies	System or experiment dependent	Used when prognostic fields not available
TRIP river paths	1° data from Oki and Sud (1998)	Adjusted at coastlines to ensure correct outflow

[a] This is expanded to a "zonally symmetric" 3-D field in limited-area simulations on a rotated pole grid.

the bias in lower-stratospheric water vapour by $\approx 50\,\%$. This change also improves the dynamical core's internal consistency as it means that we use the same three-dimensional interpolation algorithms for temperature and moisture.

For systems enforcing the mass conservation of moist prognostics (which we formally treat as a system-dependent option in the Global Atmosphere configuration) we change the algorithm used from that described in Zerroukat (2010) to the optimised conservative filter scheme (OCF; Zerroukat and Allen, 2015). The OCF seeks to find a weighted conservative solution between the high-order semi-Lagrangian solution discussed above and a lower-order (trilinear) solution, where the weights are optimised such that the conservative solution stays as close as possible to the high-order one whilst achieving conservation. This particular change has little impact on the moisture biases in the lower stratosphere but makes the conservation algorithm for moisture consistent with that used for atmospheric composition fields (see Sect. 3.8).

3.1.2 Conservative advection of mass-weighted potential temperature (GA ticket #146)

For an adiabatic flow, virtual dry potential temperature (θ_{vd}) is constant within a fluid parcel moving with the flow. Additionally, the product of θ_{vd} and the density of dry air ρ_{d} is also conserved, i.e.

$$\frac{\partial(\rho_{\mathrm{d}}\theta_{\mathrm{vd}})}{\partial t} + \nabla.(\rho_{\mathrm{d}}\theta_{\mathrm{vd}}\boldsymbol{u}) = 0. \quad (1)$$

In the ENDGame formulation, however, the fluid flow is not discretised in a conservative form; even in the absence of diabatic sources and sinks, the semi-implicit semi-Lagrangian time step does not satisfy the discrete form of Eq. (1), which leads to a spurious source of energy, as discussed in Sect. 5.4.3 of Walters et al. (2017).

In GA7, we address this by applying the same OCF conservation-recovery algorithm discussed above in the context of moist prognostics to the θ_{vd} field; unlike the conservation of moist prognostics, however, this is not treated as a system-dependent option and is applied in all systems using GA7. This improves the warm biases in the tropical tropopause layer, as discussed in Hardiman et al. (2015). By removing this spurious source of energy, it also reduces the

size of (and resolution dependence in) the global energy correction step used in long climate simulations, as described in Sect. 2.13.

3.1.3 Reduction of solver tolerance in the iterative Helmholtz solver (GA ticket #153)

As discussed in Sect. 2.1 and 2.2, an important part of the ENDGame time step is the iterative solution of the linear Helmholtz problem to determine the model's pressure field. The approach is said to have reached its solution when a global normalised residual term (the solver "norm") is smaller than a predetermined small value, or "tolerance". The smaller the tolerance, the more accurate the solution, albeit at the cost of requiring more iterations to reach it. In GA6, the solver tolerance was set to 1×10^{-3}, which was thought a suitable balance between accuracy and computational cost. At horizontal resolutions at or above about N512 (≈ 25 km in the mid-latitudes), however, global GA6 simulations suffered from numerical noise in the meridional wind near the poles in the topmost few levels (i.e. at altitudes of 65 km and above). The underlying cause of this noise is not known, but it was noted that local calculations of the solver norms have shown that these are largest close to the poles. Although the cause and effect is unclear, reducing the global solver tolerance by 2 orders of magnitude makes the noise almost imperceptible, but this is at the cost of increasing model run time by over 50 %. Reducing by only a single order of magnitude, however, significantly reduces this noise, whilst only increasing run time by ≈ 15 %. For this reason, in GA7 we have implemented this compromise and use a solver tolerance of 1×10^{-4}.

3.2 Solar and terrestrial radiation

3.2.1 Improved treatment of gaseous absorption (GA ticket #16)

GA7 includes an updated treatment of gas absorption with newly derived correlated-k coefficients for all gases as described in Sect. 2.3. Generation and validation of the gas absorption coefficients involved the creation of two configurations: a high wavelength resolution reference configuration (for offline comparison and diagnostic use) and a low-resolution broadband configuration for use in the full model. The reference configurations contain 300 bands in the LW and 260 bands in the SW (SOCRATES spectral files: sp_lw_300_jm2, sp_sw_260_jm2) and are based on the same data sources as the broadband files (primarily HITRAN 2012). These were validated against independent line-by-line codes and were subsequently used as a reference to verify the performance of the broadband configurations (SOCRATES spectral files: sp_lw_ga7, sp_sw_ga7) over a range of atmospheric conditions and greenhouse gas forcing scenarios.

The resulting SW treatment improves the representation of H_2O, CO_2, O_3, and O_2 absorption compared to GA6 and also now includes absorption from N_2O and CH_4. Changes result in increased atmospheric absorption and reduced surface (clear-sky) fluxes reducing errors compared to reference results from the Continual Intercomparison of Radiation Codes (CIRC; Oreopoulos et al., 2012).

The new LW treatment improves the representation of all gases resulting in reduced clear-sky outgoing LW radiation (OLR) and increased downward surface flux. In particular, improvements to the treatment of the water vapour continuum significantly improve the downward LW surface fluxes in regions of low humidity. The stratospheric heating rates, in particular the stratospheric water vapour forcing, are significantly improved, addressing errors described by Maycock and Shine (2012). There is also a significant improvement in the CO_2 forcing, especially for CO_2 concentrations of 4 times the present-day value and above. Figure 1 compares the errors in LW fluxes for various CO_2 concentrations based on the clear-sky atmospheric profiles used for CIRC. In both the SW and LW regions there is a significant improvement in the band-by-band breakdown of absorption compared to GA6 where cancellation of errors between different bands was important. This should improve the interaction with band-by-band aerosol, cloud, and surface properties such as the albedo of the sea.

3.2.2 Improved treatment of sub-grid-scale cloud water content variability (GA ticket #15)

In order to represent the radiative effects of sub-grid-scale water content variability, the radiation scheme uses the McICA as described in Hill et al. (2011). In the McICA, the variability of water content within a grid box is determined by a fractional standard deviation (f), which is equal to the standard deviation of cloud water content in a grid box divided by its mean value. The transmission of radiation through a cloud is a convex function of the cloud water content such that increasing the value of f decreases the radiative effect of a cloud, whilst decreasing f has the opposite effect (e.g. Shonk and Hogan, 2010). In GA6, we used a globally constant value of $f = 0.75$, but in reality, the water content variability itself is variable and the magnitude of f has been linked to cloud type, cloud fraction, wind shear and domain size (e.g. Hogan and Illingworth, 2003; Oreopoulos and Cahalan, 2005; Hill et al., 2012). At GA7, we include some of these effects by determining f from the parametrisation of P. G. Hill et al. (2015). In the interests of physical consistency, this parametrisation is also used in the warm rain part of the microphysics scheme. The implementation of the P. G. Hill et al. (2015) parametrisation results in f that depends on cloud fraction, vertical layer thickness, and whether or not the cloud is convective, where convective cloud is identified based on the activation of the convection scheme.

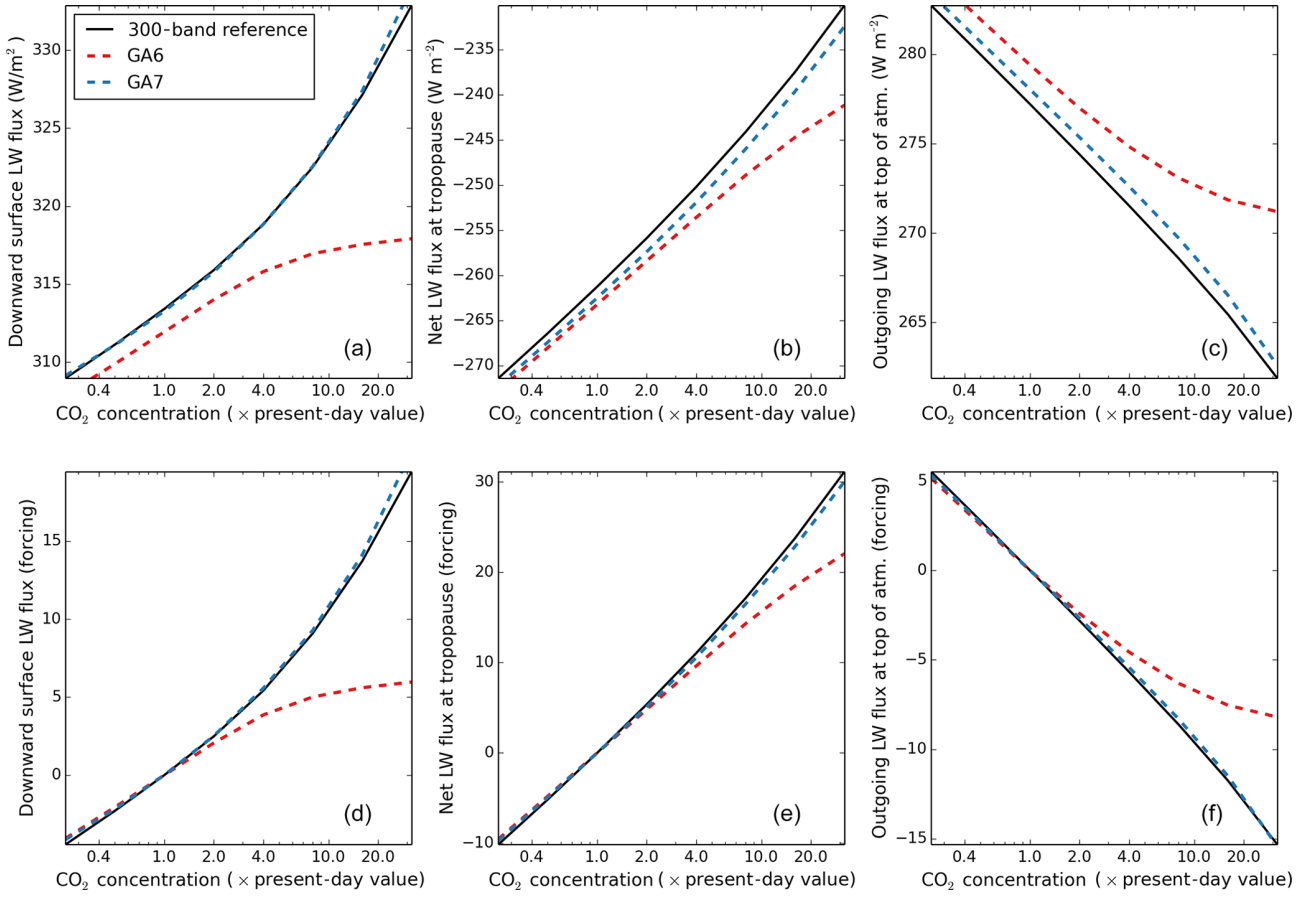

Figure 1. Comparison of LW flux errors due to changes in CO_2 concentration using GA6 and GA7 gaseous absorption compared to a 300-band LW reference configuration. Plots show an average response over the four clear-sky atmospheric profiles used for CIRC (Oreopoulos et al., 2012) which represent a broad range of water vapour path lengths. The top row shows the actual mean fluxes over the four profiles, whilst the bottom row shows the flux differences compared to a run using present-day CO_2.

The implementation of this scheme in GA7 included one change from that described in P. G. Hill et al. (2015), whereby the grid-box size dependency was replaced by a fixed effective resolution of ≈ 100 km. It was discovered during testing that adjusting the sub-grid variability with resolution led to a large resolution sensitivity in cloud properties because the model did not resolve extra variability at the same rate as which the parametrisation removed it. This is because the parametrisation is based on observed variability, whilst the model resolves features at an effective resolution far greater than the grid-box length (of the order of $10\Delta x$). Therefore, for GA configurations at resolutions ≥ 10 km, the effective resolution required in the parametrisation is ≈ 100 km. As the parametrisations do not show much change in variability beyond this, and the data used to construct them become increasingly sparse, it was felt simplest to use the same value in all GA resolutions.

3.2.3 Consistent ice optical and microphysical properties (GA ticket #17)

In GA7, we parametrise the scalar optical properties of ice crystals using the scheme described in Baran et al. (2016). This is based on an ensemble model of ice crystals developed by Baran and Labonnote (2007), where the bulk ice optical properties are derived by averaging habit-dependent scalar optical properties over an assumed particle size distribution function (PSD). This approach has the advantage that it is possible to generate ice optical properties from PSDs with the same microphysical assumptions used in the model's microphysics scheme; the same mass of ice is passed into each scheme, and the bulk scalar ice optical properties are parametrised as a function of ice mass and temperature as described in Baran et al. (2016). This improves the self-consistency within the model in a way that is generally not achieved with scalar optical properties determined from an ice crystal effective dimension as was done in GA6 and in most other atmospheric models; as a result, those models

usually assume inconsistent PSDs and mass–diameter relations in the microphysics and radiation schemes.

The difference between the Baran et al. (2016) scheme implemented in GA7 and the Baran et al. (2014) scheme that was originally proposed is that in the original scheme, the derived optical properties are fitted to be functions of the spectral band (see Table 2) and the model's prognostic ice water mass mixing ratio only, whilst in GA7, and in Baran et al. (2016), there is an additional functional relationship to the atmospheric temperature (fitted to data sampled between −80 and 0 °C). This relationship to temperature was included to improve the temperature error in the tropical tropopause layer, which is highly sensitive to the specification of the scalar ice optical properties (Hardiman et al., 2015).

3.3 Large-scale precipitation

3.3.1 Revised ice-microphysical properties (GA ticket #11)

The representation of the ice PSD has been improved by adopting the parametrisation developed by Field et al. (2007). The mass–diameter relation of ice crystals is similarly updated to new, more accurate measurements (Cotton et al., 2013), and the ice crystal fall speeds are changed to be within the range of values reported in the literature. This PSD is derived from a much larger dataset of in situ cloud measurements than that used in GA6, and the data were corrected, as much as possible, for the effects of ice particle shattering during the measurement process. Similarly, the new mass–diameter relation was derived from measurements obtained with instruments designed to mitigate against the effects of shattering. Contamination of the GA6 PSD by shattering artefacts leads to an overestimation of small particle sizes; convective-scale case studies suggest that this causes the microphysical characteristics of simulated cloud to be poorly predicted (Furtado et al., 2015).

The new PSD has several practical advantages. Firstly, it allows a unified representation of ice cloud in the microphysics and radiation schemes (see Sect. 3.2.3), an approach that was previously hampered by the effects of small particle sizes on SW reflectance from cloud tops. Secondly, case studies show that it works well with a realistic choice of particle fall speeds (Furtado et al., 2015). By contrast, in GA6, fall speeds that lay outside the range of available data were used in order to obtain realistic ice water contents. The main effects of the new parametrisation are on ice water content and specific humidity in the upper troposphere, which are shown to improve the simulation of the tropical tropopause layer (Hardiman et al., 2015). Moreover, when combined with the reduction in cirrus spreading discussed in Sect. 3.4.4, the new ice microphysics improves comparisons between modelled ice cloud radiative properties and satellite observations.

3.3.2 New warm rain microphysics (GA ticket #52)

In GA7, the warm rain part of the large-scale precipitation scheme has been almost completely rewritten. The autoconversion and accretion parametrisations are now those of Khairoutdinov and Kogan (2000), following work by Boutle and Abel (2012) to demonstrate that this significantly improves the amount of precipitation produced by marine stratocumulus and leads to improvements in the cloud cover, liquid water content and boundary-layer structure. In addition to this, improvements to the evaporation and sedimentation code have removed some undesirable consequences of the previous implementation, such as significant evaporation of rain inside cloud and an explicit non-conservation of rainwater. A. A. Hill et al. (2015) demonstrated that this new scheme significantly improves the representation of aerosol–cloud precipitation interactions relative to the scheme used in GA6.

The new scheme also includes an explicit representation of how sub-grid variability affects microphysical process rates, based on Boutle et al. (2014a). The local process rates are upscaled to the grid-box size based on parametrisations of the hydrometeor fractional standard deviation within a grid box, given by P. G. Hill et al. (2015) for cloud and Boutle et al. (2014a) for rain. Note this means that for cloud water content, the same parametrisation of sub-grid variability is used consistently in the radiation and microphysics. Without parametrisation of the sub-grid variability, the model would underestimate autoconversion and accretion rates, and it would not be possible to implement the Khairoutdinov and Kogan (2000) parametrisations. The parametrisation of the sub-grid rain fraction has also been improved, ensuring this is set consistently by either the fraction of autoconverting cloud or melting snow when rain is created. To avoid the need to advect this quantity, when rain is advected into a grid box which was previously rain-free, the rain fraction is set to the fraction of cloud directly above it, as that is likely to be the cloud from which the rain originated and will have been advected by the cloud scheme. The implementation of this scheme in GA7 uses a fixed effective resolution of ≈ 100 km rather than the grid-box size dependency described in Boutle et al. (2014a). The reasons for this are discussed in Sect. 3.2.2.

Figure 2 summarises the effect of this change on low cloud and light rain. It has been noted elsewhere that previously, like many general circulation models (GCMs), the UM had too much rain in the lightest rain rate category (Bodas-Salcedo et al., 2008; Stephens et al., 2010). This is shown by the large frequency of radar returns in the −30–0 dBZ range below 2 km for GA6, in stark contrast to the observations from CloudSat. The inclusion of the new warm microphysics scheme considerably improves this bias, with simulated radar returns now a very good match to CloudSat observations below 2 km. The complete GA7 package shows similar improvements, effectively removing the long-standing model bias of excessive light rain.

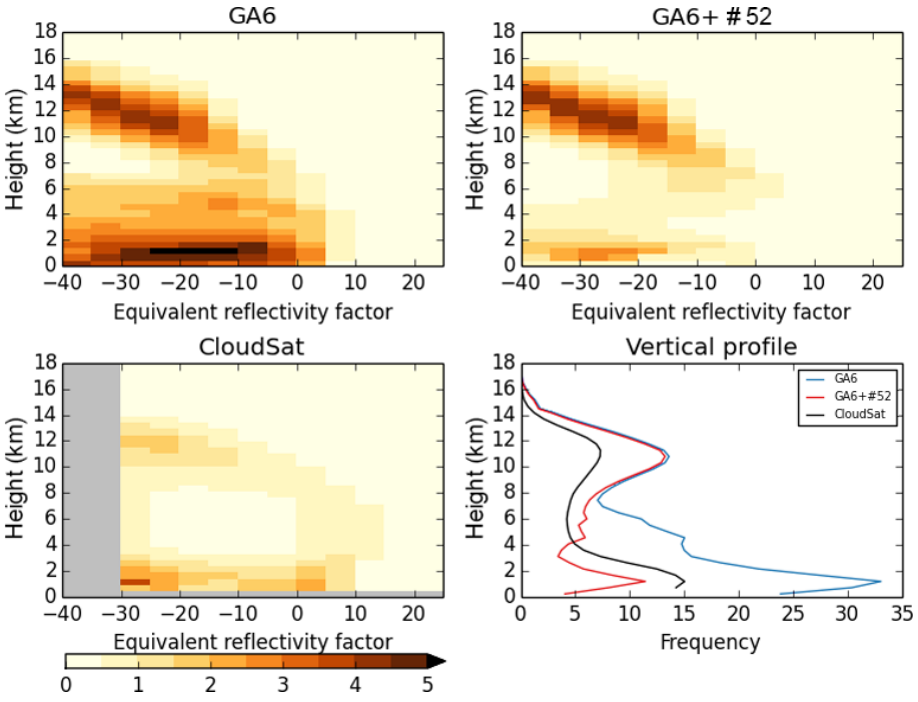

Figure 2. Histograms of height vs. 94 GHz radar reflectivity over a trade cumulus region (130–160° W, 0–20° S), showing climatologies of CloudSat observations and simulated CloudSat data from 20-year N96 atmosphere/land-only climate simulations using GA6.0 and GA6.0 plus the new warm microphysics scheme.

3.4 Large-scale cloud

3.4.1 Including the radiative impact of convective cores (GA ticket #44)

In the PC2 cloud scheme, the impact of convective cloudiness is represented by source terms that couple the convection scheme to PC2 in a manner following Tiedtke (1993) and Wilson et al. (2008a). As a convective plume rises, it mixes with its environment and detrains cloudy air, which updates the prognostic cloud compensate and fraction fields that are subsequently used in the radiation scheme. As a result, it is only once condensate has detrained from the convective plume that it will have a radiative impact, whilst the radiative effect of the core of the convective updraught is ignored. This was originally justified by the fact that the fraction of the grid box occupied by the convective updraughts in a mass-flux convection scheme is assumed to be small. However, for some convective cloud types, such as shallow fair-weather cumulus, cloud may not detrain much into the environment but still has a significant radiative impact. To include the impact of this cloud, we use a convective cloud model from GA7 to include the radiative impact of the convective cores themselves. For shallow convection, the CCA is calculated from the cloud-base mass flux divided by the convective velocity scale following Grant and Lock (2004). This is then modified by a shape function that has its maximum value at the cloud base, its minimum at the cloud top and decreases exponentially with height. For mid-level or deep convection, the CCA is calculated from the convective precipitation rate, P, using CCA$= a + b \ln P$, following Slingo (1987), where $a = 0.3$ and $b = 0.025$. The convection scheme also calculates a profile of CCW. The profiles of the CCA and CCW are then combined with the PC2 cloud fields before being passed to the cloud generator used by McICA to calculate the radiative impact of the cloud. The models for the CCA and CCW were originally developed to represent the cloud in the entire convective column (and not just the core of the convective updraught) so the value of the CCA is scaled down before being combined with the PC2 cloud. Empirically chosen independent scaling factors are applied to the CCA from deep, mid-level and shallow convection. The original values proposed were 0.1, 0.1 and 0.5 respectively, although the latter value was subsequently tuned down to 0.2, as discussed in Sect. 3.11; no scaling is applied to CCW in GA7. Note also that the CCA and CCW are not added to the prognostic cloud fields themselves and hence are not advected by the flow; instead, they are only radiatively active on the time steps in which convection has been diagnosed.

3.4.2 Consistent treatment of phase change for convective condensate passed to PC2 (GA ticket #58)

One benefit of using PC2 for modelling cloud created from detrained convective condensate is that this allows a con-

sistent treatment of cloud, independent of the source of the cloud itself. The microphysical assumptions in the generation of cloud from large-scale processes and convective processes, however, are currently independent. Whilst the microphysical assumptions in the convection scheme are far simpler than those used elsewhere in the model, it is still beneficial to ensure consistency at the level to which this is possible. One inconsistency identified in the GA6 treatment of convective cloud is in the phase of condensate passed from the convection scheme to PC2. To avoid an abrupt change of phase, in GA6 the phase of condensate detrained from convection scaled linearly from 100 % liquid at 0 °C to 100 % ice at −20 °C; in PC2, however, the maximum temperature at which ice could form was −10 °C. Here, we improve this consistency by reducing the upper limit at which ice can be formed by convection to −10 °C so that there are matching assumptions in the large-scale cloud and convection schemes.

3.4.3 Turbulence-based critical relative humidity (GA ticket #89)

The PC2 cloud scheme uses a critical relative humidity (RH_{crit}) to determine when to initiate cloud in cloud-free grid boxes with increasing RH and to remove cloud from fully cloud-filled grid boxes in which RH is reduced. In previous GA configurations, RH_{crit} was a constant global value for each model level, which is a simplification, but is tunable to global mean cloud distributions. This is undesirable for future climate projections, however, as these could show large changes in global cloud and RH distributions, which might not be handled correctly in these cloud initiation and removal processes. Therefore, in GA7 we have implemented a method for calculating a variable RH_{crit} based on sub-grid turbulence.

The method is discussed in Van Weverberg et al. (2016), and involves parametrising the sub-grid variance and covariance of temperature and humidity in terms of the resolved vertical gradients and the sub-grid mixing length, eddy diffusivity and turbulent kinetic energy (TKE) calculated by the boundary-layer parametrisation. The TKE is diagnosed from the vertical velocity variance, σ_w^2, which is given by

$$\sigma_w^2 = K_m \tau_{turb}^{-1}, \tag{2}$$

where K_m is the eddy diffusivity for momentum and $\tau_{turb}^{-1} = \max(\tau_{surf}^{-1}, \tau_{sc}^{-1}) + \tau_{sbl}^{-1}$ is a turbulence timescale, calculated following Suselj et al. (2012) as a combination of convective and stable boundary-layer timescales. The stable timescale is given by $\tau_{sbl} = N/0.7$, where N is the Brunt–Väisälä frequency. The convective timescales are derived following the large-eddy simulations (LESs) of Holtslag and Moeng (1991) and are given by

$$\tau_{surf} = \frac{C_{ws}^{2/3} \kappa z_h}{1.33 w_m}, \tag{3a}$$

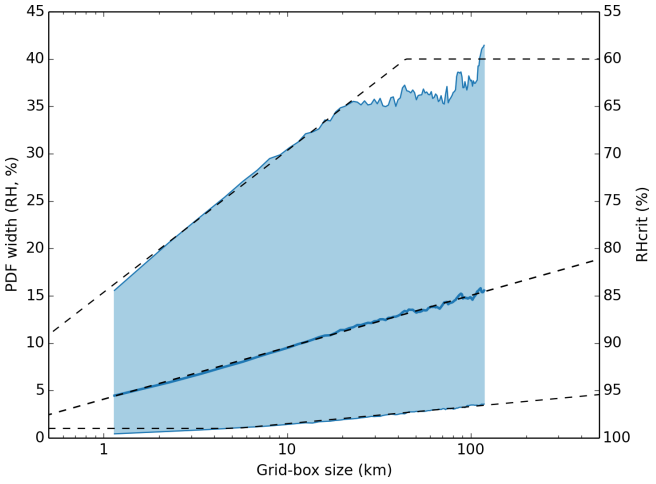

Figure 3. Mean and 5th and 95th percentiles (central line and edges of the blue shaded region) of RH_{crit} as a function of flight length from aircraft observations, and fits to the data (dashed lines) used in the model parametrisation.

$$\tau_{sc} = \frac{g_1 \kappa z_{ml}}{1.33 V_{sc}}, \tag{3b}$$

where κ is the von Kármán constant; z_h and z_{ml} are the surface and cloud-top driven mixed layer depths; and w_m and V_{sc} are surface and cloud-top velocity scales, $C_{ws} = 0.25$ and $g_1 = 0.85$. Strictly speaking, whilst σ_w^2 is the major component of TKE in a GCM, this is not a good approximation near the surface. The vertical velocity variance must tend to zero near the surface, but the TKE remains high due to continuity as horizontal fluctuations converge or diverge near the base of vertical fluctuations. To represent this, we set the TKE, e, equal to σ_w^2, but we hold it constant below the maximum value of the surface-driven non-local component to K_m.

To ensure numerical stability of the scheme, we constrain the calculated RH_{crit} value to lie between a maximum and minimum value. These values are calculated from aircraft observations of cumulus and stratocumulus cloud in the VOCALS (Wood et al., 2011) and RICO (Rauber et al., 2007) campaigns. Using all available flight data, Fig. 3 shows the mean RH_{crit} as a function of the flight leg length (grid-box size) and the 5th and 95th percentiles of the data. We use fits to these as the maximum and minimum allowed values of RH_{crit}.

Finally, in a change from the original implementation of Wilson et al. (2008a), because the RH_{crit} has been calculated based on the assumption of a triangular probability density function (PDF), we assume this shape when initiating cloud in PC2 rather than the previously used top-hat PDF. Van Weverberg et al. (2016) has shown that the parametrisation of RH_{crit} is a reasonable match to independent lidar observations, and the implementation shows no degradation to GA6

performance, with the desired benefit of being less tuned to the present-day climate.

3.4.4 Removal of redundant complexity when dealing with ice cloud (GA ticket #98)

PC2 deals with falling ice cloud condensate by increasing the ice cloud fraction in the layer where the frozen condensate falls. The increased ice cloud fraction is larger than that in the layer above to represent some lateral displacement of the vertically projected falling ice due to shear-generated fall streaks. In configurations GA4–GA6, this calculation was modified to use the local shear in the model's winds rather than a globally constant value. This led to an unrealistic reduction in mean ice cloud fraction, which was mitigated by introducing a cirrus spreading term that increased the frozen cloud fraction, C_{ff}, via

$$\partial C_{\mathrm{ff}}/\partial t = 2r(C_{\mathrm{ff}} - C_{\mathrm{ff}}^2), \tag{4}$$

where r is the cirrus spreading rate. The $C_{\mathrm{ff}} - C_{\mathrm{ff}}^2$ term ensures that ice cloud spreads more slowly when there is little cloud present or as the grid box approaches an overcast state. In GA6, this rate was set to $r = 1.0 \times 10^{-3}\,\mathrm{s}^{-1}$.

Separately, in order to avoid the model producing regions of extensive ice cloud fraction when the ice water content was very low, GA6 included a term in the ice cloud fraction tendency which ensured that if the in-cloud ice water content (grid-box mean ice water content divided by ice cloud fraction) was less than $1.0 \times 10^{-6}\,\mathrm{kg\,kg}^{-1}$, the ice cloud fraction would be reduced accordingly. In GA6, both of these terms were necessary for the model to achieve a realistic distribution of ice cloud fraction, but in some regions, they were found to be acting in strong opposition. As part of the development of the package of cloud changes in GA7, we originally planned to reduce the cirrus spreading rate to a value very close to zero; in tuning the final GA7 configuration as described in Sect. 3.11, this was increased to a final value of $r = 1.0 \times 10^{-5}\,\mathrm{s}^{-1}$. This is still small enough to allow us to remove the minimum in cloud ice water content.

3.4.5 Turbulent production of liquid water in mixed-phase cloud (GA ticket #120)

Many atmospheric models are known to have problems producing and maintaining supercooled liquid and mixed-phase cloud, which instead is preferentially glaciated into ice-only cloud (Illingworth et al., 2007; Klein et al., 2009). A lack of liquid water in cold cloud has been implicated as a major contributor to severe model biases, particularly in the Southern Hemisphere storm-tracks, where observations suggest that nature produces an abundance of supercooled liquid water (Williams et al., 2013; Bodas-Salcedo et al., 2014). In this region, too little modelled supercooled liquid leads to too little SW radiation reflected out to space and hence too much solar heating of the sea surface. This can lead to a host of problems in the simulation of the coupled Earth system (see Hyder et al., 2018, for a review).

Motivated by these factors, Field et al. (2014) developed a new approach for parametrising the production of liquid water in mixed-phase cloud. They analytically solve the dynamics of supersaturation fluctuations in turbulent mixed-phase cloud under the action of adiabatic lifting by turbulent air-motions, exchange of air between the cloud and its environment, and the depletion of supersaturation by microphysical growth of the ice phase; this solution is used to calculate a probability distribution of supersaturation. The liquid-cloud properties (water content and cloud fraction) are then calculated as moments of this distribution. The distribution is Gaussian, with mean and variance specified in terms of the parameters that describe the turbulence and the state of any pre-existing ice cloud. The parametrisation was tested against LESs of mixed-phase cloud with which it was found to be in good agreement (Hill et al., 2014).

The Field et al. (2014) parametrisation was implemented in the UM by Furtado et al. (2016). To close the model, the sub-grid probability distribution is specified using the diagnostic of vertical velocity variance from the boundary-layer scheme, Eq. (2), and the ice PSD from the microphysics scheme. The inclusion of the parametrisation was shown to increase the amount of supercooled liquid and mixed-phase cloud, which improved the simulation of a case study of Arctic stratus and reduced biases in outgoing SW radiation over the Southern Ocean. However, the parametrisation performed poorly in the tropics, where it led to an over-production of liquid water in warm cloud. The was traced to assumptions in the model which limit its validity to regimes where liquid condensation is relatively small. Therefore, in GA7, the scheme is only used for temperatures below 0 °C, where this approximation can be shown to be reasonable (Furtado et al., 2016). Above 0 °C, liquid condensation is handled by the PC2 cloud initialisation scheme, which in GA7 uses the turbulence based $\mathrm{RH_{crit}}$ scheme described above.

3.5 Sub-grid orographic drag

Introduction of heating due to gravity-wave dissipation (GA ticket #87)

In GA7, we introduce terms for the conversion of kinetic energy to frictional heating, where drag is exerted on the flow, which were neglected in previous releases of the GA configuration. This includes heating corresponding to gravity-wave breaking (in both the orographic and non-orographic schemes) and low-level-flow blocking drag, thus improving the energy conservation of the model[2]. The frictional heating

[2]Frictional heating from drag in the boundary-layer scheme was already included and has been since GA3.

can be written as

$$\frac{\partial T}{\partial t} = -\frac{1}{c_\mathrm{p}}\left(u\frac{\partial u}{\partial t} + v\frac{\partial v}{\partial t}\right), \tag{5}$$

where T is temperature, c_p is the specific heat capacity at constant pressure and the $\partial/\partial t$ terms are the total tendencies due to the (orographic and non-orographic gravity-wave) drag schemes. The heating term is small in a global average sense. In the lower troposphere, where the dominant contribution comes from flow-blocking drag, global mean values are typically only $\sim 10^{-2}\,\mathrm{K\,day^{-1}}$ at N96 resolution, although locally, values can be as large as $10\,\mathrm{K\,day^{-1}}$ over the major mountain ranges. In the middle atmosphere, the heating comes from gravity-wave dissipation. Maxima associated with orographic gravity waves are typically between 10 and $20\,\mathrm{K\,day^{-1}}$ at heights of 50 km in the winter hemisphere over major orography. At higher levels, the contribution from the non-orographic gravity-wave drag provides more widespread heating, with global mean heating rates at 65 km of $\sim 1\,\mathrm{K\,day^{-1}}$.

3.6 Atmospheric boundary layer

3.6.1 Revised dependence of boundary-layer entrainment on decoupling (GA ticket #13)

The parametrisation of turbulent entrainment through the top of cloudy boundary layers involves sources from both cloud top (radiative and evaporative cooling) and the surface (positive buoyancy fluxes and wind shear). When the cloud layer is decoupled from the surface, this implies that the stratification associated with the decoupling inversion will restrict the surface-driven turbulence from affecting the cloud layer, and in particular from driving entrainment at the cloud top. Currently this impact of decoupling is diagnosed to occur when $\Delta\theta_\mathrm{vl}$ exceeds 0.5 K, where θ_vl is the adiabatically conserved virtual potential temperature in cloud-free air, which is used as a simplified measure of buoyancy. Single-column model (SCM) comparisons with LESs of the transition from stratocumulus to trade cumulus (e.g. Neggers et al., 2017) show that this leads to a sudden and substantial decrease in parametrised entrainment in the SCM that is not seen in the LES. Here, we make this abrupt transition more gradual by still including the entire impact of the surface contribution for $\Delta\theta_\mathrm{vl} < 0.5$ K but weighting this down linearly until there is no contribution above $\Delta\theta_\mathrm{vl} = 1$ K. Note that this comparison with LES implies that some surface-driven entrainment should continue for longer during the decoupling process and will thus potentially lead to additional thinning of stratocumulus during the day.

3.6.2 Forced convective cloud and resolved mixing across the boundary-layer top (GA ticket #83)

Prior to GA7, the parametrised boundary-layer entrainment flux was implemented simply at the flux level at the top of the mixed layer, implying that the vertical resolution was insufficient to resolve the distribution of this flux across the capping inversion. As vertical resolution becomes finer, this approach becomes increasingly untenable. In addition, for relatively weak inversions capping strongly surface-heated boundary layers (which occur commonly in desert regions), capping inversions can easily extend over 1 km and so should already be resolved (e.g. Garcia-Carreras et al., 2015).

To distribute the entrainment fluxes across the capping inversion, its thickness, Δz_i, must first be diagnosed. Assuming that this thickness is largely determined by the height to which turbulent thermals impinging into the stable stratification aloft can penetrate, an energetic argument (Beare, 2008) implies the following:

$$6.3 w_\mathrm{m}^2 = \int_{z_h}^{z_h+\Delta z_i} b\,\mathrm{d}z, \tag{6}$$

where w_m is the boundary-layer velocity scale ($w_\mathrm{m}^3 = u_*^3 + 0.25 w_*^3$, w_* is the convective velocity scale and u_* the friction velocity) and b is the buoyancy, taken here from the convective diagnosis parcel. Note that the empirical constant in Eq. (6) is actually the same as Beare's value of 2.5 because the definition of w_m^3 here differs by a factor of 4 (and $6.3 \approx 2.5 \times 4^{2/3}$). The integration over the depth of the inversion is calculated working upwards from the level of neutral buoyancy, z_h, assuming piecewise linear variation between grid levels. Note that if this predicts that a boundary-layer parcel has sufficient energy to penetrate any convective inhibition, and so reaches the level of free convection, then the convection scheme is triggered. As a result, this represents a significant change in this triggering.

If Δz_i is thicker than the model grid spacing (and the convection scheme has not been triggered), the entrainment fluxes across the inversion are implemented as a standard down-gradient diffusive flux, with the diffusion coefficient K_h between levels k and $k+1$ given by

$$K_h|_{k+\frac{1}{2}} = \frac{-\overline{w'\theta'_\mathrm{vl}}}{(\theta_{\mathrm{vl}k+1} - \theta_{\mathrm{vl}k})/(z_{k+1} - z_k)}.$$

Within the inversion, $\overline{w'\theta'_\mathrm{vl}}$ is assumed to decrease from the standard parametrised entrainment flux at the inversion base ($\overline{w'\theta'_\mathrm{vl}}|_\mathrm{entr}$) to zero at the inversion top following a cosine function, i.e.

$$\overline{w'\theta'_\mathrm{vl}} = \overline{w'\theta'_\mathrm{vl}}|_\mathrm{entr} \cos\left(\pi\frac{z'}{2}\right), \tag{7}$$

where $z' = (z - z_h)/\Delta z_i$ is the scaled height within the inversion.

At points where the convection scheme is triggered, the top of the surface-based turbulently mixed layer was formerly capped at the LCL so that the only mixing across

the cumulus cloud base was through the convection scheme. This was seen to lead to errors in the mean profiles across the LCL, with the most extreme, if rare, examples including superadiabatic lapse rates and large decreases in moisture. Using the boundary-layer parametrisation to couple cloud and sub-cloud layers has the numerical advantage of being solved implicitly but is also consistent with LES evidence that turbulence continues to show characteristics of the sub-cloud layer across the cloud-base transition region (Grant and Lock, 2004). It is also consistent with the above resolved approach to boundary-layer entrainment fluxes to implement a (potentially) resolved profile of fluxes across the top of the sub-cloud layer in cumulus-capped regimes. This then requires a method of diagnosing the top of the surface-driven K profile in these regimes that avoids double counting the moist convective transport in the cloud layer that will be handled by the convection scheme. The approach adopted is to extend the algorithm used to diagnose boundary-layer decoupling, which limits the buoyancy consumption of turbulence kinetic energy, but the latent heat release is excluded from the diagnosed buoyancy flux. Conceptually the boundary-layer scheme can be thought of as representing the cloud-free transport in grid boxes containing cumulus cloud. Idealised clear-sky convective boundary layers (where the magnitude of the entrainment buoyancy flux is a fraction, A_1, of the surface flux) suggest that the ratio of the integrated buoyancy consumption to production is A_1^2, which, consistent with the entrainment parametrisation, is taken to be 0.05.

Now that the thickness of the capping inversion has been parametrised, this allows forced convective cloud to be represented. This cloud forms in undulations of the top of convective boundary layers but remains too shallow to reach its level of free convection (and become fully fledged cumulus cloud). They currently require special treatment because these sub-grid undulations of the capping inversion can typically imply a rather bimodal moisture distribution, consisting of moist boundary-layer domes surrounded by intrusions of very dry free-tropospheric air. From a survey at the Southern Great Plains Atmospheric Radiation Measurement (ARM) site, Zhang and Klein (2013) found that almost 40 % of summertime fair-weather shallow cumulus cloud was of this forced type and so would likely make a significant contribution to the radiation budget. A simple approach to represent them is adopted here. A profile of the equilibrium-forced cloud fraction is parametrised as varying linearly in height between a cloud-base value, at the LCL of the convection diagnosis parcel, and a cloud-top value top of 0.1. The cloud-base cloud fraction is parametrised as varying linearly with cloud depth, between a minimum of 0.1 and a maximum of 0.3 for cloud depths between 100 and 300 m, based loosely on the observations of Zhang and Klein (2013). The cloud top is taken to be the top of the boundary-layer inversion (at $z_h + \Delta z_i$) or, in cumulus-capped regimes, the top of the surface-driven K profile. The in-cloud liquid water content at the top of the inversion is taken to be that of the adiabatic convection diagnosis parcel, with linear interpolation used between the lifting condensation level and inversion top. To allow for sub-adiabatic water content (due to lateral mixing or microphysical processes) the in-cloud water content can be reduced by a factor that has been set to 0.5 in GA7. Increments are calculated, as necessary, to increase the prognostic cloud fraction and water content variables to these forced convective cloud fraction and liquid water content profiles at the end of the time step.

3.7 Convection

3.7.1 Introduction of the 6A convection scheme (GA ticket #64)

Major changes to parametrisations in the UM are indicated by incrementing the version of the scheme, with each version denoted by a number and letter combination. GA6 used the 5A version of the convection scheme; the parcel ascent calculations in the 5A scheme and its predecessors were originally developed at a time when model resolution, particularly in the vertical, and the demand for accuracy in the parcel ascent were lower both than they are currently and than they are expected to be in the future. Motivated by this, a review of the 5A convection scheme was undertaken, and areas where improvements could be made were identified. These improvements were implemented in the 6A convection scheme, which is used in GA7. The main improvements made between the 5A and 6A convection schemes are the following:

- The calculation of forced detrainment assumes that (i) the detrained mass is saturated and is neutrally buoyant with respect to the environment and that (ii) the remaining convective plume is buoyant and saturated. These conditions result in implicit equations for the potential temperature of the detrained mass and the residual plume. In the 5A convection scheme, a single iteration is used to solve each of these implicit equations, whereas the 6A scheme uses three iterations.

- After the convective parcel is lifted from one level to the next in a dry ascent, it is brought to saturation. This involves solving for potential temperature at saturation at a given pressure, $\theta^{\mathrm{P,sat}}$, from

$$c_{\mathrm{p}}\Pi\left(\theta^{\mathrm{P,sat}} - \theta^{\mathrm{P,dry}}\right) = L\left(q^{\mathrm{P,dry}} - q_{\mathrm{sat}}\left(\theta^{\mathrm{P,sat}}\right)\right), \qquad (8)$$

  where c_{p} is the specific heat capacity at constant pressure; Π is the Exner pressure; $\theta^{\mathrm{P,dry}}$ and $q^{\mathrm{P,dry}}$ are the potential temperature and specific humidity, respectively, of the parcel after dry ascent; and q_{sat} is the specific humidity at saturation. This calculation is performed iteratively, where the 5A convection scheme uses two iterations and the 6A scheme uses three iterations, to bring this closer to convergence. Unlike the

5A scheme, the 6A convection scheme also allows the evaporation of parcel condensate if the parcel becomes sub-saturated after entrainment and the dry ascent.

- The calculation of forced detrainment allows an ensemble of plumes with a distribution of buoyancies to be represented by a single convective plume for which only the mean buoyancy is explicitly calculated (Derbyshire et al., 2011). The convective ascent is therefore terminated when the forced detrainment reduces the mass flux to a small value, i.e. when the large majority of the implied ensemble of plumes have terminated after becoming negatively buoyant. To that end, the ascent in the 6A scheme will terminate when the mass flux falls below 5 % of its value at the cloud base, which replaces the arbitrary small value in the 5A scheme, or when the forced detrainment needs to detrain more than 95 % of its mass. As before, shallow convection will terminate at the top of its diagnosed parcel ascent.

- Building on the convective "safety checks" introduced at GA6, the 6A convection scheme applies additional checks to ensure that the parcel ascent is valid. In particular, the cloud-base mass flux after closure needs to be greater than zero, convection needs to be at least three levels thick, and there needs to be at least some latent heat release during the ascent (i.e. purely dry convection is not permitted).

- A turbulent heating term to account for the loss of kinetic energy due to the convective momentum transport is added, similar to that described for sub-grid orographic drag in Sect. 3.5.

- We introduce a local correction to conserve water and energy in the column. Without this, the convection scheme will introduce small errors in the water and energy budgets from (i) truncation error in the discretisation and (ii) the convection scheme assuming hydrostatic balance and a shallow atmosphere (i.e. that the horizontal area of the grid boxes does not increase with height), whilst the full model does not. To account for these small errors, the 6A scheme applies a correction to total column water and energy to ensure that the column integrals of these quantities is the same after the call to convection as they were before.

The 6A convection scheme diagnoses convective ascents that are usually deeper than those from the 5A scheme. It also removes occasional vertical grid-scale noise in its increments to the model's prognostic fields. This is demonstrated in the results of the SCM simulations presented in Fig. 4.

Both of these effects are due primarily to the iterative convective parcel ascent calculations. Deeper convection translates into the tops of the deepest tropical cloud being beneficially higher. Figure 5 shows a comparison of the height of

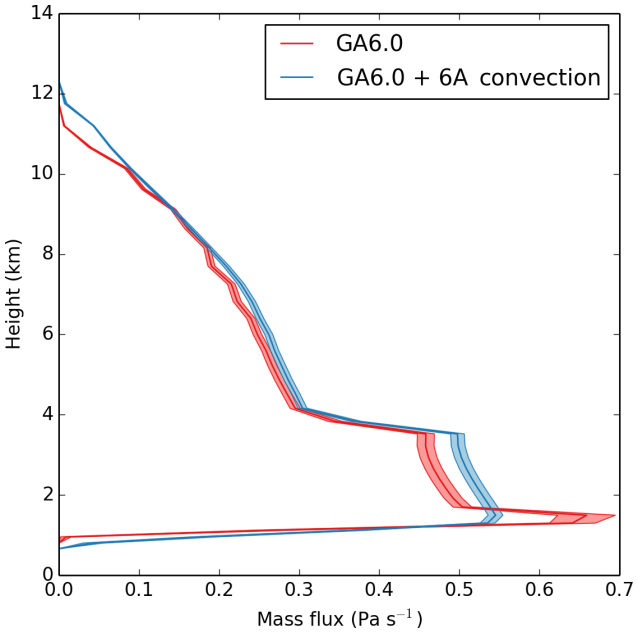

Figure 4. Profiles of mean convective mass flux from a pair of 100-member SCM ensembles using the GA6 configuration and the 6A convection scheme. The initial profiles and forcings are for an idealised diurnal cycle over tropical land (described in detail as experiment "r76" in Table 1 of Stirling and Stratton, 2012). The profiles are for 4 h means centred on local noon; the thick lines show the time-averaged ensemble mean and the shading shows ±2 times the standard error in the ensemble mean.

tropical cloud in an N96 atmosphere/land-only climate simulation and in CALIPSO observations, which shows that the cloud top height in the 6A convection scheme is in better agreement with observations than in GA6; a similar improvement is seen throughout the tropics. Note, however, that this does not affect errors in other aspects of the cloud simulation; for these, we rely on the other changes in GA7 (Williams and Bodas-Salcedo, 2017).

Finally, in addition to the changes itemised above, the 6A convection scheme includes an amount of code tidying and re-factoring that does not lead to any scientific differences but means that this provides as a more suitable baseline for future development.

3.7.2 CAPE closure for deep and mid-level convection dependent on large-scale vertical velocity (GA ticket #84)

Prior to GA7, the deep and mid-level convection schemes used a fixed CAPE timescale, only shortened if very high vertical velocities were detected in a column. As discussed in Sect. 4.1.1 of Walters et al. (2017), the choice of a fixed timescale to suit both NWP and climate needs has been difficult, with NWP favouring a shorter timescale that improves the predictive skill of the model and climate modellers pre-

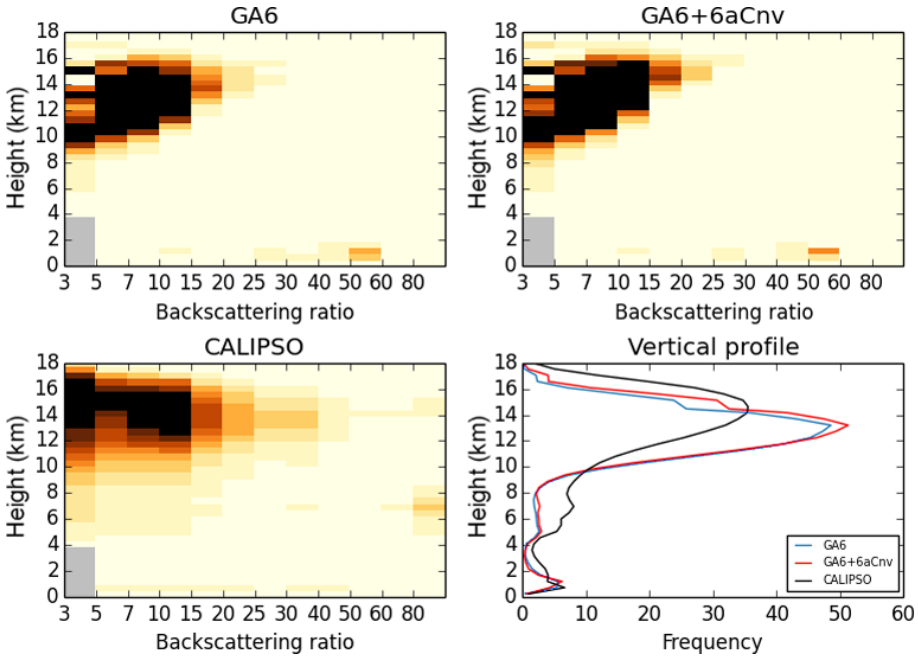

Figure 5. Histograms of height vs. 532 nm lidar backscatter ratio over the tropical warm pool, showing CALIPSO observations and simulated climatologies of CALIPSO data from 20-year N96 atmosphere/land-only climate simulations using GA6.0 and GA6.0 plus the 6A convection scheme.

ferring a longer timescale that reduces intermittent behaviour and improves the mean climatology.

The UM convection scheme uses the dilute CAPE from the buoyant convective ascent, so we require a CAPE timescale for the dilute CAPE. An analysis of a few days of data from two 1.5 km resolution simulations from the CASCADE project (Pearson et al., 2014), one over western Africa and the other over the Indian Ocean, enabled us to investigate the deep convection by coarse gridding the data to $(150\,\mathrm{km})^2$ and $(30\,\mathrm{km})^2$ by area-averaging 100×100 or 20×20 grid points respectively. The fraction of buoyant and cloudy grid points and their properties relative to the mean were calculated, enabling us to estimate the dilute CAPE for deep convection.

Figure 6 shows the distribution of CAPE timescales. It is clear that the CAPE timescale is not fixed and varies with resolution, with longer timescales being more frequent at coarser resolution; this explains why finding a fixed CAPE timescale for a model used across a range of resolutions is not easy. Our analysis of the data found a relationship between the mass-weighted mean vertical velocity and the dilute CAPE timescale such that

$$\tau_{\mathrm{CAPE}} = a w_{\mathrm{LS}}^{b}, \tag{9}$$

where w_{LS} is the mass-weighted mean vertical velocity over the depth of the deep or mid-level convection and $a = 0.08$, $b = -0.7$, derived from a fit to the CASCADE data. The model w_{LS} can be negative or very small, giving a very long CAPE timescale. In this case, for the deep convection scheme, an upper limit is derived from the surface-based closure used in the shallow scheme (Grant, 2001). In the mid-level scheme, an upper limit of 4 h is used. Both deep and mid-level convection have a lower limit set to the model convection time step.

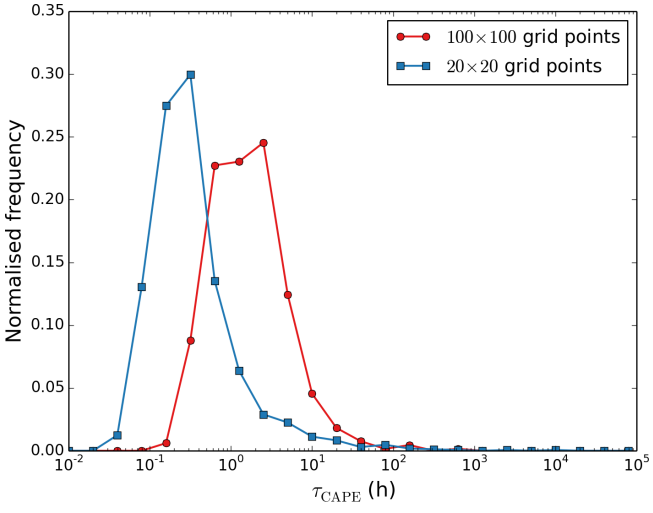

Figure 6. Normalised frequency distribution of convective timescale of deep convection from analysis of a small region of the Indian Ocean at resolutions of 100×100 and 20×20.

Table 4. The aerosol size distribution in GLOMAP-mode including aerosol modes represented and the range of radii that these include, their geometric standard deviation, and aerosol species contributing to each mode. Species represented are sulfate, black carbon, organic carbon and sea salt.

Aerosol mode	Radii (nm)	σ_g	Species
Nucleation sol.	0–5	1.59	SO_4, OC
Aitken sol.	5–50	1.59	SO_4, BC, OC
Accumulation sol.	50–250	1.40	SO_4, BC, OC, SS
Coarse sol.	250–5000	2.00	SO_4, BC, OC, SS
Aitken insol.	5–50	1.59	BC, OC

3.8 Atmospheric aerosols and chemistry

Introduction of the UKCA GLOMAP-mode aerosol scheme (GA ticket #60)

In previous GA configurations, tropospheric aerosol was treated using either prognostic aerosol simulations or monthly mean climatologies from the CLASSIC aerosol scheme (Bellouin et al., 2011). In GA7, the simulation of prognostic aerosol is performed using the GLOMAP-mode[3] (Mann et al., 2010). Whilst CLASSIC was a simple mass-based bulk aerosol scheme, GLOMAP-mode models the aerosol number, size distribution, composition and optical properties from a more detailed, physically based treatment of aerosol microphysics and chemistry. This is expected to improve the representation of aerosol radiative effects and aerosol–cloud interactions (e.g. Bellouin et al., 2013) and was viewed as a requirement in GA7 so that GLOMAP-mode could be used as the atmospheric aerosol component of the UK's next Earth system model, UKESM1.

Speciated aerosol mass and number are simulated in five variable size modes representing soluble nucleation, Aitken, accumulation and coarse size ranges as well as an insoluble Aitken mode. As outlined in Sect. 2.10, the prognostic aerosol species represented are sulfate (SO_4), black carbon (BC), organic carbon (OC) and sea salt (SS), with species within each mode treated as an internal mixture. The size ranges covered by each mode and aerosol species contributing to each mode are illustrated in Table 4. The variable size distribution allows the median dry radius of each mode to change within these size ranges, whilst the standard deviation, σ_g, of each mode is fixed.

In full chemistry–aerosol simulations such as those used for Earth system modelling, aerosol precursor gases required for the production of SO_4 and secondary organic aerosols are provided by the UKCA stratospheric–tropospheric chemistry scheme (Morgenstern et al., 2009; O'Connor et al., 2014). In physical model simulations, such as in the GA/GL climate simulations presented below, we use a simplified offline oxidant chemistry scheme in which the required chemical oxidant fields (such as O_3, OH, NO_3 and HO_2) are provided as monthly mean climatologies derived from an online chemistry simulation. GLOMAP-mode can simulate aerosol microphysical processes such as the nucleation of SO_4 aerosol, cloud processing, mode merging, coagulation within and between modes, and condensational growth of existing particles due to uptake from gas-phase sulfuric acid and secondary organic vapours. Aerosol water content is simulated prognostically, which combined with the internal mixing of aerosols within modes, leads to a more realistic treatment of the aerosol optical properties than the previous CLASSIC scheme. The direct radiative impact of the aerosols is modelled using the UKCA-Radaer scheme outlined in Sect. 2.3. Cloud condensation nuclei are activated into cloud droplets using the UKCA-Activate aerosol activation scheme (West et al., 2014). In addition to the GLOMAP-mode species listed in Table 4, we continue to model mineral dust separately using the CLASSIC dust scheme (Woodward, 2011), although a modal framework for the emission of mineral dust is being developed for future implementation.

One of the aerosol optical properties that is well observed in both ground-based and satellite observations is the aerosol optical depth (AOD). Figure 7 illustrates that the annual mean climatology of AOD in an N96 GA7/GL7 atmosphere/land-only climate simulation matches these observations well in both the mean value and its geographical distribution.

To illustrate the suitability of using GLOMAP-mode simulations to diagnose the concentration of cloud condensation nuclei, Fig. 8 compares observed and simulated monthly mean aerosol number concentration of particles with a diameter greater than 50 nm (N50) from the same simulation presented in Fig. 7a.

The simulated aerosol number is in reasonable overall agreement with the observations, with approximately 60 % of the data agreeing within a factor of 2. The regional breakdown highlights good performance in relatively clean air regions such as the Arctic, Antarctica and ocean basins, although the model underestimates N50 in more polluted regions such as North America, Europe and Asia. It is a point of ongoing discussion whether the current approach of targeting high-pollution events with observational campaigns leads to biases in comparisons of models to observations for these events (Reddington et al., 2017; Schutgens et al., 2017).

The two-moment modal scheme represents a significant increase in complexity versus the single-moment CLASSIC scheme. This additional complexity leads to improvements in the aerosol simulation but increases the computational cost of the model, with the run time to solution in an atmosphere/land-only climate simulation at N96 resolution increasing by about 50 %. In future, it may be desirable to develop a traceable hierarchy of aerosol complexity within the GLOMAP-mode framework, which would reduce the expense of some physical climate model simulations and

[3] GLOMAP-mode is included in the UM code base as part of the UK Chemistry and Aerosol (UKCA) code.

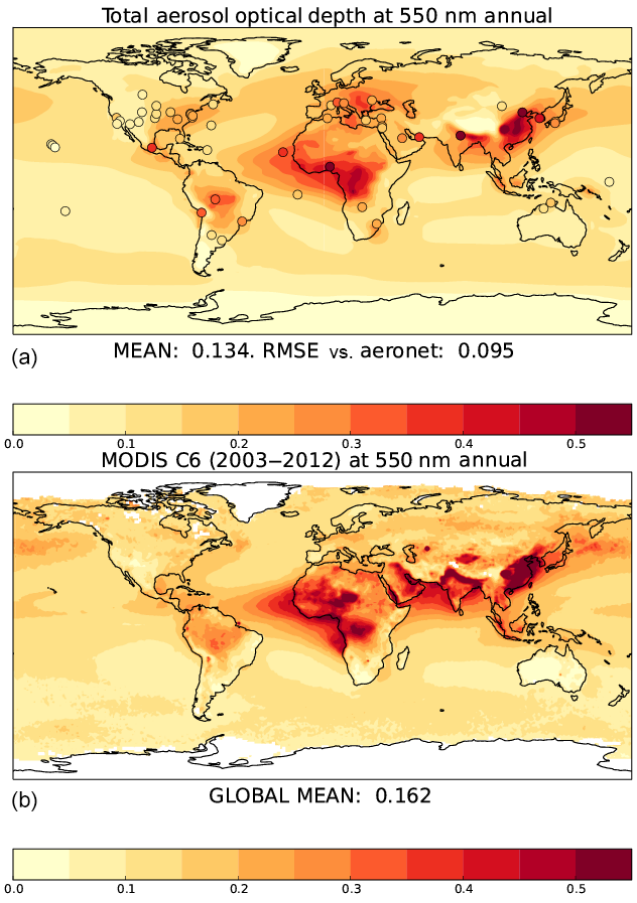

Figure 7. Annual mean AOD at 550 nm from a 20-year N96 atmosphere/land-only GA7/GL7 climate simulation **(a)** and satellite observations from the Moderate Resolution Imaging Spectrometer (MODIS; **b**). The annual mean MODIS observations are derived from monthly mean level 3 products from MODIS Aqua Collection 6 (Sayer et al., 2014) and cover the period 2003–2012. An annual mean climatology of level 2 AOD observations at 500 nm from the ground-based AERONET sun photometer network (Holben et al., 2001) at 67 worldwide locations are overlaid on the GA7 spatial plot.

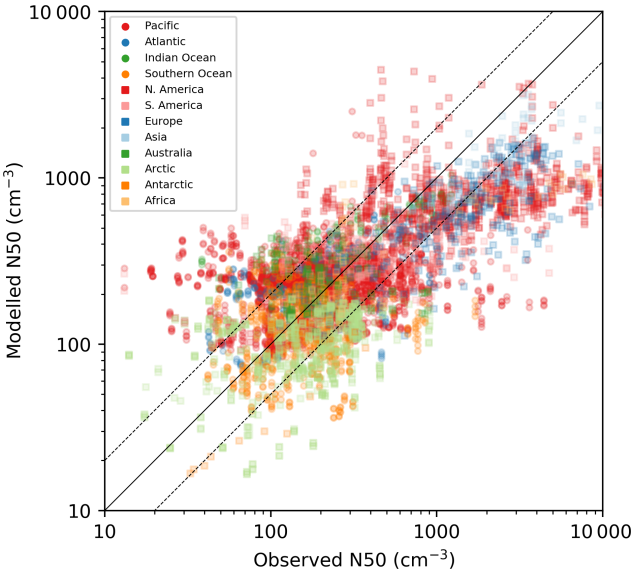

Figure 8. Monthly mean simulated N50 from the simulation presented in Fig. 7 versus observations from campaign and ground station data collated via the Global Aerosol Synthesis and Science Project (see references for details; GASSP, 2017; Reddington et al., 2017). For a detailed description of the data sets used, see Appendix A. The data are harmonised and averaged to monthly means (assuming that observations are representative of the month) and compared with the model on the model grid. Different colours and symbols denote data from different regions.

allow implementation in systems not currently using prognostic aerosol, such as NWP and seasonal forecasting systems. Another temporary limitation of GLOMAP-mode – and its interaction with the UM physics via Radaer and Activate – is that the code does not yet work with climatological aerosol fields, which we currently require in these systems without prognostic aerosol. In these simulations, therefore, we continue to use climatologies from the CLASSIC aerosol scheme and the calculation of optical properties and cloud droplet concentrations that were used in GA6 as described in Sect. 2.3 of Walters et al. (2017). Whilst this is far from ideal, in parallel climate simulations using the prognostic GLOMAP-mode and climatological CLASSIC aerosols (not shown, for brevity), the model's climatological radiation fluxes are broadly similar. This traceability between prognostic GLOMAP-mode simulations and CLASSIC climatologies was an imposed constraint on the implementation of GLOMAP-mode in GA7 that will allow us to continue to support a seamless Global Atmosphere configuration across a variety of modelling systems. This constraint on further development of the configurations can eventually be relaxed once we can use aerosol climatologies derived from GLOMAP-mode in Radaer and Activate.

3.9 Land surface and hydrology: Global Land 7.0

3.9.1 Introduction of the multi-layer snow scheme (GL ticket #4)

In GL6 and before its development, JULES used a simple snow scheme, described in Best et al. (2011), in which lying snow and the topmost soil layer are represented as a single thermal layer; because the snow in this scheme had no independent thermal store, this is labelled as a "zero-layer" scheme. This was a major deficiency in the configuration, as it allowed the surface layer of the atmosphere direct access to heat within the soil and thus poorly represented the insulating effect of the snowpack in the real world (Slater et al., 2017). In GL7, we introduce a new snow scheme based on the multi-layer scheme also described in Best et al. (2011). In stand-alone land surface simulations, where JULES is driven

by near-surface meteorological fields, soil temperatures and permafrost extent are substantially improved by using the multi-layer scheme (Burke et al., 2013). However, the additional degrees of freedom introduced by coupling the scheme to an atmospheric model impose more stringent constraints on the parametrisation and have led to a number of enhancements being introduced to improve the scheme in the coupled atmosphere–land system.

The multi-layer snow scheme works by accumulating snow in the topmost snow layer until this reaches a specified maximum thickness, when the layer is split into two. As the snowpack deepens, subsequent snow is accumulated in the lower layer until it reaches its maximum thickness and splits again. The maximum permitted number of snow layers is set to three, which earlier tests suggested was sufficient for representing the snowpack with reasonable fidelity. The maximum thickness of the first and second snow layers are set to 0.04 and 0.12 m respectively, which is reduced from the values of 0.1 and 0.2 m in the original scheme. Any snow beyond the combined 0.16 m thickness of the first two layers is held in the third layer. For deep snow, this means that the thinnest layers are at the top. For reasons of numerical stability, the original zero-layer scheme is still used when the thickness of the snowpack is less than the thickness of the first snow layer. The reduction of this layer from 0.1 to 0.04 m, therefore, reduces this use of the zero-layer scheme and allows the snowpack to respond more rapidly to changes in atmospheric conditions.

The density of fresh snow is set to $109\,\mathrm{kg\,m^{-3}}$, following Vionnet et al. (2012) but omitting their dependence on temperature and wind speed. The thermal conductivity is parametrised using the formula given by Calonne et al. (2011), replacing that of Yen (1981). Unlike the original parametrisation, this improved formula includes the effect of thermal conduction through the air in the snowpack, which is significant in newly fallen snow. Although the original scheme allows for temperature-dependent mechanical compaction of the snow, temperature gradient metamorphism is not included. In the GL7 implementation, we introduce a parametrisation for rapid densification of fresh snow by equi-temperature metamorphism (i.e. the rounding of irregular snow grains due to the vapour pressure being higher on convex than on concave surfaces) based on Anderson (1976). This causes a significant increase in the density of fresh snow on the timescale of a few days, and omitting it would result in prominent cold biases across the Northern Hemisphere. The effect of temperature gradient metamorphism is still omitted, however, which remains a topic for future research. A rate of unloading of snow from needle-leaved trees that is dependent on wind speed has been introduced and adjusted to give a typical unloading timescale of 2 days in the Canadian boreal forest (MacKay and Bartlett, 2006). Rainwater and meltwater from snow on the canopy are also allowed to infiltrate into the snowpack, rather than bypassing it as in the original version of the scheme. Finally, a new parametrisation of the snow albedo, based on a two-stream model of radiative transfer through the snowpack and a prognostic snow grain size, has also been introduced.

The largest impact of the new scheme on the model's climatology comes from its insulation of the soil beneath the snowpack. Figure 9 shows that in December–February (DJF), the near-surface air over the Northern Hemisphere snowpack is generally colder, as the heat flux from the soil into the atmosphere is reduced, whilst in March–May (MAM) the air is warmer, as the snow-melt over warmer soils leads to less cooling from below. It also shows that the annually integrated effect of this additional insulation is a significantly warmer soil layer, which improves a long-standing model bias and is expected to be highly desirable for the simulation of permafrost.

3.9.2 Further improvements to land surface albedo (GL ticket #30)

In both GL6 and GL7, the snow-free SW albedo of the land surface is calculated for each grid box, which is a weighted average of the albedos of the different surface types. The albedo of bare soil is input as ancillary data, described in Sect. 2.14, whilst the other non-vegetated surface types have a constant first guess albedo. The albedo of vegetated surface types varies between the bare soil albedo and a full leaf albedo depending on the leaf area index (LAI) of that vegetation type. Additionally, when the land surface properties are fixed – rather than evolving as occurs in Earth system simulations using interactive vegetation – the albedos of each tile are scaled, within physical limits, so that the grid-box mean snow-free albedo matches that of an observed climatology.

In GL6, these albedos were independent of wavelength, whilst in GL7, a limited spectral variability has been added by applying separate calculations for the photosynthetically active radiation (PAR) and near-infrared radiation (NIR) using the canopy radiation model of Sellers (1985). When the albedos are scaled, they are compared to climatologies of the grid-box mean PAR and NIR albedos, and the input albedos or leaf reflectivity and scattering coefficients are changed accordingly using a predictor–corrector step to account for the slight non-linearity in the canopy radiation model. Again, the albedos and reflectivities are kept within physical limits.

Alongside this change, the minimum albedo of the urban tile was reduced from 0.16 to 0.05 to better match observed albedos in urban areas. Finally, the generation of the data of land surface types was slightly amended; this process takes the 17 land surface types from the International Geosphere–Biosphere Programme dataset (IGBP; Loveland et al., 2000) and maps them to the nine land surface types used in JULES. In GL7, the amount of bare soil present in the grassland, cropland, and crop and natural mosaic IGBP classes was reduced, as we believe that the original mappings used increased bare soil values to account for seasonally barren veg-

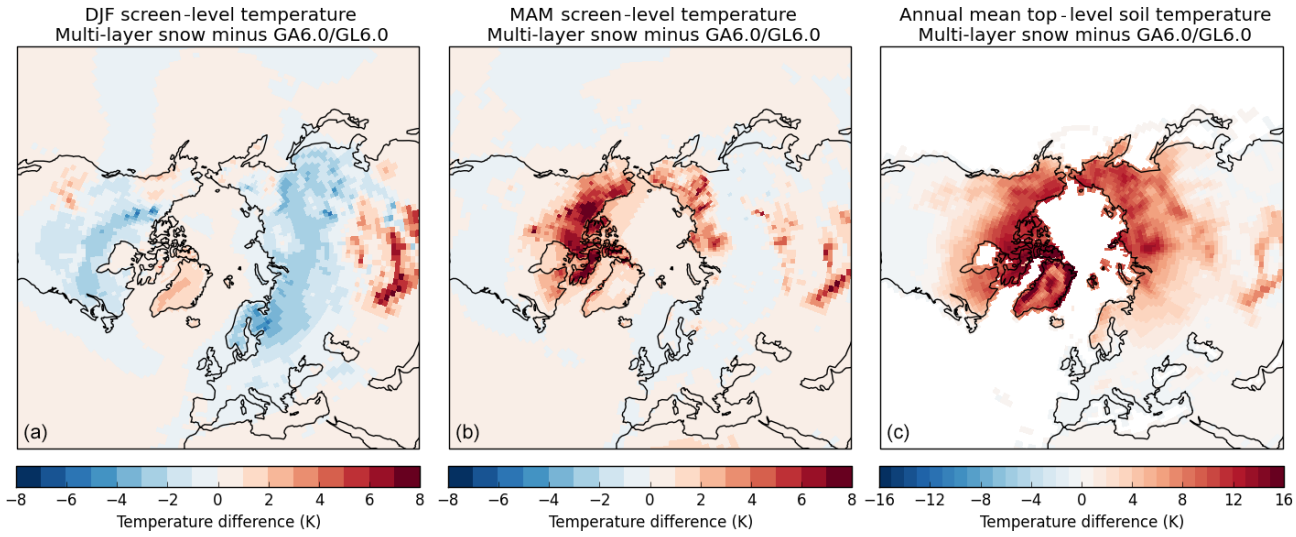

Figure 9. The difference in mean DJF screen-level temperature **(a)**, mean MAM screen-level temperature, **(b)** and annual mean topmost level soil temperature **(c)** from a 20-year N96 atmosphere/land-only climate simulation with and without GL7's multi-layer snow scheme. The baseline simulation is GA6.0/GL6.0.

etation, which is now accounted for in the time-varying LAI. The mappings used in GL7 are shown in Table 5.

3.9.3 Improved parametrisation of the ocean surface albedo (GL ticket #43)

GL6 parametrised the ocean surface albedo (OSA) with the method of Barker and Li (1995) in which OSA is a function solely of the solar zenith angle, accounting for the glitter of the sea surface (Cox and Munk, 1954). In addition to this, hardwired scaling factors were applied for each of the SW bands in Table 2 to enforce a spectral variation.

GL7 implements the OSA parametrisation of Jin et al. (2011), which has the advantage of including an additional dependence on wavelength as well as on the 10 m wind speed and chlorophyll content. The wavelength and chlorophyll-content dependency of the optical properties are taken from lookup tables of data from Jin et al. (2011).

The wind speed dependency represents two effects. Firstly, an increased wind speed leads to an increase in the number and size of ocean waves on the sea surface, which in turn increases the variability of the incident angle of reflection at the surface (sea surface "glitter"). This leads to a higher albedo at low solar zenith angles and a lower albedo it at higher zenith angles. Secondly, an increased wind speed leads to the breaking of waves, which creates whitecaps; these are represented by assigning a fraction of the model grid box as ocean foam with an albedo of 0.55. Finally, the spectral variability across the SW bands in Table 2 is represented by calculating the average of the OSA for 50 wavelengths within each band.

The chlorophyll content is prescribed via a new ancillary field, which contains a periodic monthly climatology based on GlobColour ocean colour data. The GlobColour products merge ocean colour observations from the MERIS, Moderate Resolution Imaging Spectrometer (MODIS) Aqua and SeaWiFS sensors and derive sea surface chlorophyll-*a* concentration (Maritorena et al., 2010). The climatology was created by averaging the GlobColour data from 1998–2007 onto a $1^\circ \times 1^\circ$ grid. An extrapolation was then performed to fill grid points with no satellite observations. The creation of these climatology files is described in Ford et al. (2012).

3.9.4 Use of atmospheric rain fractions in surface hydrology (GL ticket #45)

In previous GL configurations, the fraction of a grid box over which rain was assumed to fall on the land surface was set to 1.0 for large-scale rain and 0.3 for convective rain (Best et al., 2011). This information is used in the calculations of canopy throughfall and evaporation, surface infiltration, and runoff. Atmospheric changes introduced at GA7 have allowed these rain fractions to be more accurately calculated, and therefore we use this information consistently within the surface scheme. The large-scale rain fraction is now given by the scheme introduced in Sect. 3.3.2, whilst the convective rain fraction is given by the maximum convective core area from the scheme introduced in Sect. 3.4.1.

3.9.5 Implement surface roughness from the COARE4.0 Algorithm (GL ticket #31)

In JULES, the momentum roughness length over the sea surface ($z_{0,\mathrm{m}}(\mathrm{sea})$) is given by

$$z_{0,\mathrm{m}}(\mathrm{sea}) = 0.11\frac{\nu}{u_*} + \alpha_{\mathrm{ch}}\frac{{u_*}^2}{g}, \tag{10}$$

Table 5. Mapping from IGBP classification to JULES land surface types in GL7 (%). The abbreviated headers are broadleaf trees, needleleaved trees, temperate C_3 grass, tropical C_4 grass, shrubs, urban areas, inland water, bare soil and land ice surface types respectively. Values that have changed are marked in bold with GL6 values in brackets.

IGBP code	IGBP name	BL	NL	C3g	C4g	SH	UR	IW	BS	LI
1	Evergreen needleleaf forest	0.0	70.0	20.0	0.0	0.0	0.0	0.0	10.0	0.0
2	Evergreen broadleaf forest	85.0	0.0	0.0	10.0	0.0	0.0	0.0	5.0	0.0
3	Deciduous needleleaf forest	0.0	65.0	25.0	0.0	0.0	0.0	0.0	10.0	0.0
4	Deciduous broadleaf forest	60.0	0.0	5.0	10.0	5.0	0.0	0.0	20.0	0.0
5	Mixed forest	35.0	35.0	20.0	0.0	0.0	0.0	0.0	10.0	0.0
6	Closed shrublands	0.0	0.0	25.0	0.0	60.0	0.0	0.0	15.0	0.0
7	Open shrublands	0.0	0.0	5.0	10.0	35.0	0.0	0.0	50.0	0.0
8	Woody savannah	50.0	0.0	15.0	0.0	25.0	0.0	0.0	10.0	0.0
9	Savannah	20.0	0.0	0.0	75.0	0.0	0.0	0.0	5.0	0.0
10	Grassland	0.0	0.0	**85.0** (70.0)	**10.0** (15.0)	5.0	0.0	0.0	**0.0** (10.0)	0.0
11	Permanent wetland	0.0	0.0	80.0	0.0	0.0	0.0	20.0	0.0	0.0
12	Cropland	0.0	0.0	**85.0** (75.0)	5.0	0.0	0.0	0.0	**10.0** (20.0)	0.0
13	Urban and built up	0.0	0.0	0.0	0.0	0.0	100.0	0.0	0.0	0.0
14	Cropland/natural vegetation mosaic	**7.5** (5.0)	**7.5** (5.0)	**60.0** (55.0)	15.0	10.0	0.0	0.0	**0.0** (10.0)	0.0
15	Snow and ice	0.0	0.0	0.0	0.0	0.0	0.0	0.0	0.0	100.0
16	Barren or sparsely vegetated	0.0	0.0	0.0	0.0	0.0	0.0	0.0	100.0	0.0
17	Water bodies	0.0	0.0	0.0	0.0	0.0	0.0	100.0	0.0	0.0

where u_* is friction velocity. The first term, dominant in low-wind conditions, accounts for the kinematic viscosity of air ν (Smith, 1988), whilst the second term is the Charnock relation in which α_{ch} is the Charnock parameter (Charnock, 1955) and g is the acceleration due to gravity. Previous GL configurations used a constant Charnock parameter of $\alpha_{\mathrm{ch}} = 0.018$; observational evidence, however, suggests that younger waves are rougher (Donelan et al., 1993) such that the Charnock parameter should be correlated with the wind speed. Such a parametrisation is implemented in the COARE (Coupled Ocean–Atmosphere Response Experiment) family of bulk flux algorithms (Edson et al., 2013), so in GL7 we implement the roughness parametrisation used in COARE4.0 (Edson, 2009), in which the Charnock parameter increases with wind speed up to $22\,\mathrm{m\,s^{-1}}$. Above this wind speed, the roughness length is capped as there are few observations and surface exchange at very high wind speeds is not well understood (Soloviev et al., 2014). JULES uses a single roughness length for scalar variables; we adopt the COARE4.0 moisture roughness length for this, which is identical to that used in COARE3.0 (Fairall et al., 2003). Finally, note that we have only implemented the roughness lengths from the COARE algorithm, and other aspects of surface exchange, such as the similarity functions, follow those standard in JULES.

3.9.6 Revised roughness lengths for sea ice (GL ticket #38)

In the presence of sea ice, the roughness length of the non-land portion of a model grid box is taken as a weighted average of $z_{0,\mathrm{m}}$(sea) (discussed above) and of fixed roughness lengths for pack ice and marginal ice, with the weightings taken as a function of the ice fraction. As discussed in Walters et al. (2017), for GL6.0, a pragmatic decision was made to adopt values of 3.2 mm for pack ice and 100 mm for marginal ice, following earlier practice in operational weather forecasting. As further noted in that publication, these values are high compared to observational estimates, particularly for pack ice. Subsequent investigation has shown that performance is substantially unaffected if the value for pack ice is reduced to 0.5 mm, which is more comparable with the observed values, whilst performance is degraded by reducing the value for marginal ice. In GL7.0, therefore, we use roughness lengths of 0.5 and 100 mm for pack ice and marginal ice respectively. Investigation of surface exchange over marginal ice continues.

3.10 Stochastic physics

Introduction of a standardised stochastic physics package (GA ticket #117)

Prior to GA7, the use of stochastic physics schemes in the global UM was defined as a system-dependent option, which remained outside of the definition of the Global Atmosphere configuration. This means that different EPSs have used different representations of stochastic physics as they have seen fit. The global component of the Met Office Global and Regional Ensemble Prediction System (MOGREPS-G; Bowler et al., 2008) has used SKEB2 (Tennant et al., 2011) to represent model error emerging from upscale transfers of energy from truncated or highly diffused scales. It has also used the random parameters scheme version 2 (RP2; Bowler et al., 2009) to represent the structural uncertainty of a parametri-

sation's key parameters, such as the convection scheme's entrainment rate or coefficients in the gravity-wave drag. The Global Seasonal prediction system (GloSea; MacLachlan et al., 2014) has employed SKEB2 only, whilst to date, long-range climate projections have not used any stochastic physics schemes.

As discussed in Sect. 2.12, the role of stochastic physics in the performance of our prediction systems is increasing as the importance of EPSs across all timescales is growing and the impact of stochastic parametrisations on the model's climatology is better understood. For this reason, we have developed a standardised package of stochastic physics schemes that has been included for the first time in GA7. The two main components of this package are an improved version of SKEB2 and the replacement of RP2 by the SPT, both of which are described in detail in Sanchez et al. (2016). The changes to SKEB2 are a replacement of the Smagorinsky numerical dissipation mask by a biharmonic formulation, which is more representative of the numerical dissipation caused by the semi-Lagrangian interpolation to the departure point in global models with horizontal resolutions of $\mathcal{O}$ (10–100 km). The convective mask also now includes a resolution-dependent coefficient, which reduces the impact of this term at higher resolutions. Both changes to SKEB2 improve its response to resolution, and as with increased resolution, the model is less dissipative, so the error that SKEB2 is designed to overcome is itself reduced. This "scale awareness" is particularly improved in the tropics, where the original scheme was quite insensitive to resolution; in addition, at lower resolution, the changes lead to larger perturbations in the tropical free troposphere and in the atmospheric boundary layer globally (see Sect. 3 of Sanchez et al., 2016). The SPT scheme adds variability to the model parametrisations by perturbing their diagnosed tendencies rather than their internal parameters as is done in RP2. This is achieved by scaling increments in the radiation scheme, large-scale precipitation, sub-grid orographic drag, and convective heating and moistening (although not convective momentum transport). Increments from the boundary-layer scheme and increments from all other schemes in the lowest eight levels (i.e. below ≈ 660 m) remain unscaled to maintain model stability. For similar reasons, the scaling is tapered between level 9 and level 15 (i.e. between ≈ 660 and 1700 m), and large perturbations are capped in grid boxes with large standard deviations in the sub-grid orography field. The potential impact of SPT is greater than that of RP2 as it can add fluctuations to represent sub-grid and structural uncertainties of the parametrisations rather than just including uncertainty in the inputs to deterministic parametrisations. The stochasticity of both SKEB2 and SPT is applied via a first-order autoregressive forcing pattern with a 6 h decorrelation timescale and was applied spatially between horizontal wave numbers 20 and 60. Finally, to allow SPT to be used in long climate integrations, where the conservation of energy and moisture are important, an additional constraint is applied to the scheme to conserve both water vapour and moist static energy in the column, as described in Appendix B of Sanchez et al. (2016).

The stochastic physics package has been tested in a 1-month trial (run from mid-November to mid-December 2012) of short-range (3 day) ensemble forecasts with 12 members per 6-hourly cycle run at N216 horizontal resolution (≈ 60 km in the mid-latitudes). The control ensemble uses GA6.1/GL6.1 (Walters et al., 2017) with the operational SKEB2 and RP2 stochastic physics, whilst the test replaces this with the standardised stochastic physics package described above. The largest impact of the new stochastic physics package is in the tropics. Figure 10 shows spread–skill relationships for 850 hPa tropical temperature and wind speed (i.e. the comparison of the ensemble control and ensemble mean root-mean-square errors (RMSEs) versus radiosondes compared to the internal spread of the ensemble). In an ideal ensemble, the spread of the ensemble and the RMSE of the ensemble mean should match. For both parameters, the GA7 stochastic physics package shows increased spread without increasing the ensemble mean error, although the difference between the spread and error is still quite large in this small and simple ensemble test.

However, the new configuration does produce slightly worse probabilistic scores on the mid-latitude boundary layer (not shown), as neither SKEB2 or SPT include perturbations to near-surface fields, which are perturbed in the boundary-layer parameters included in RP2. In climate simulations, the use of stochastic physics improves some long-standing climate biases, particularly, in the tropics, which indicates that the coarse representation of sub-grid fluctuations has a beneficial impact on the model's tropical climatology. Figure 11, which is reproduced from Sanchez et al. (2016), shows the reduction in errors in June–August (JJA) outgoing LW radiation with the stochastic physics package at a number of resolutions.

That publication also describes improvements to other tropical errors, such as precipitation and circulation, which is consistent with the tropical improvements seen in other systems such as the European Centre for Medium-Range Weather Forecasts (ECMWF) Integrated Forecasting System (Weisheimer et al., 2014).

Finally, whilst stochastic schemes such as SKEB2 and SPT aim to provide a reasonable representation of the main sources of model error and thus produce a better distribution of weather states, they do so by inflating the variability in the current over-deterministic formulations. Whilst this leads to improvements in the reliability of an EPS or a climate simulation, these schemes are deficient in their representation of individual processes such that they will degrade the evolution of an individual forecast event such as the trajectory of an individual mid-latitude cyclone (Sanchez et al., 2013). For this reason, the stochastic physics package is not currently planned for inclusion in deterministic forecast systems, and the use (or lack) of stochastic physics remains a system-dependent option; when a system uses GA7 with

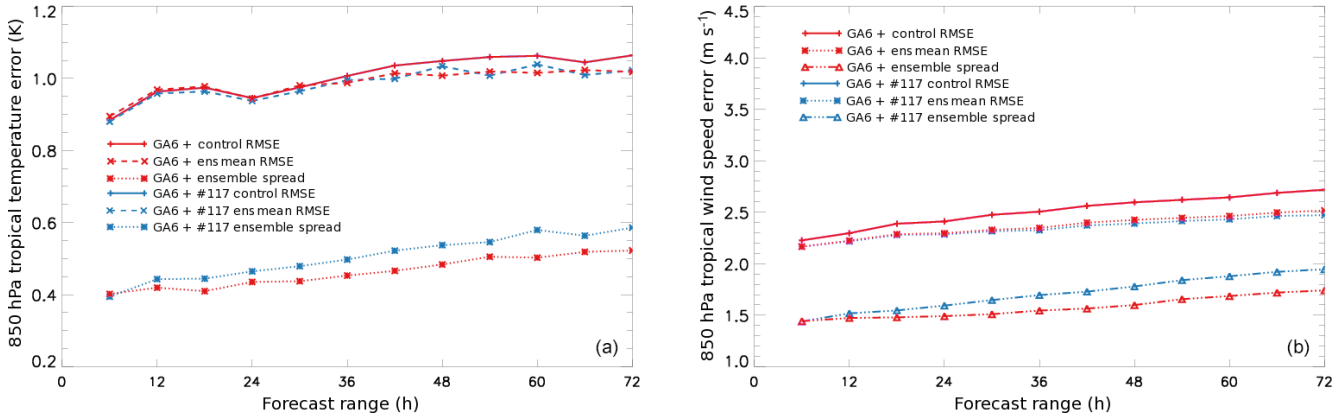

Figure 10. Ensemble error and skill for tropical temperature **(a)** and wind speed **(b)** versus radiosonde observations at 850 hPa in an N216 ensemble with the operational MOGREPS-G and GA7 stochastic physics package.

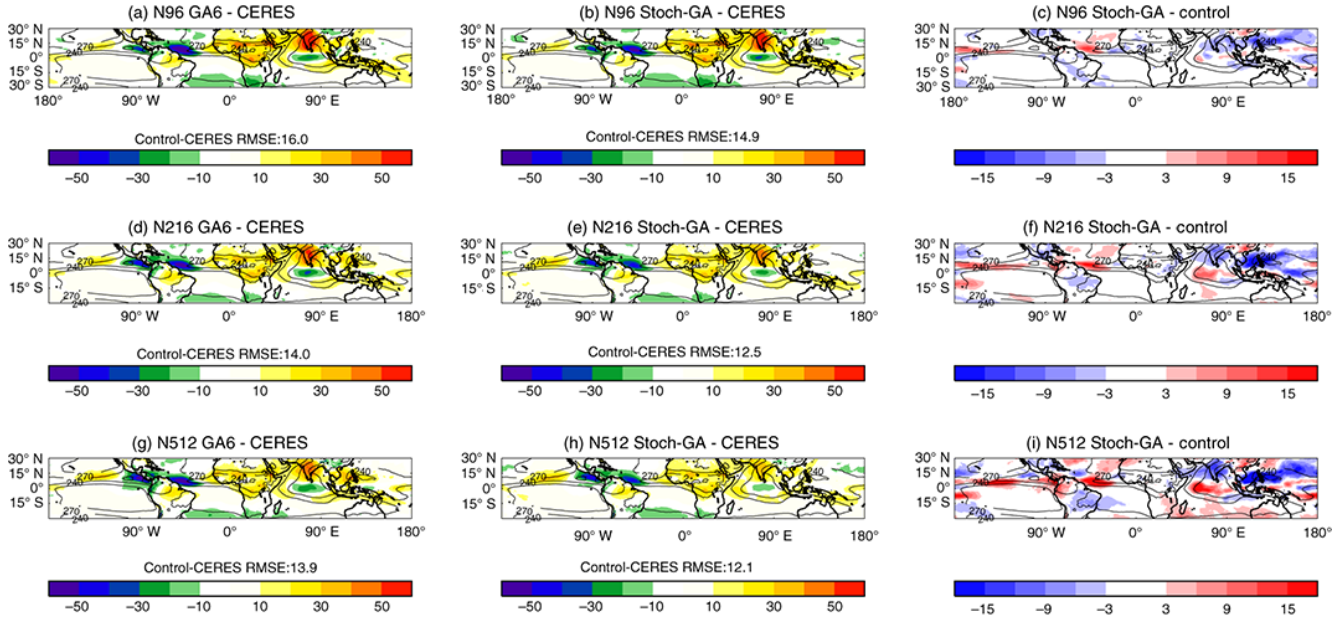

Figure 11. Mean June–August (JJA) top-of-atmosphere outgoing LW radiation (OLR) errors ($W m^{-2}$) from 20-year atmosphere/land-only climate simulations compared to Clouds and the Earth's Radiant Energy System (CERES) Energy Balanced and Filled (EBAF) dataset (Loeb et al., 2009). The columns from left to right are GA6.0 controls, GA6 plus the stochastic physics package (labelled Stoch-GA) and the difference between the two, whilst the rows from top to bottom are from simulations at N96, N216 and N512 resolution. This figure is reproduced from Sanchez et al. (2016).

stochastic physics, however, it will now be expected to use the schemes described above. In the longer term, we expect the use of more physically based parametrisation schemes with implicit stochastic elements – such as those presented in Eckermann (2011), Plant and Craig (2008) or Bengtsson et al. (2013) and Bengtsson and Körich (2016) – to overtake the use of the current, more ad hoc schemes. We would expect these more physically based stochastic schemes to be used in all prediction systems.

3.11 Tuning of the configuration

Tuning plays an important part in the process of developing any atmospheric model. Individual parametrisations will include input parameters that must be constrained using either direct observational estimates and evidence based on other modelling studies or by constraining their outputs to fall within the bounds of observational or theoretical uncertainty. For coupled climate models in particular, the balance of certain budget terms, such as the mean incoming and outgoing SW and LW radiation fluxes at the top of the atmosphere

(TOA), need to balance to a precision that is greater than the uncertainty in its individual components to stop the model from drifting into an unrealistic state (this is described briefly in Box 9.1 in Chapter 9 of Working Group I's contribution to the Intergovernmental Panel on Climate Change Fifth Assessment Report; IPCC, 2013). Recently, the topic of tuning, the parameters tuned and the constraints that they are tuned to has received some attention in the literature (e.g. Hourdin et al., 2017; Schmidt et al., 2017) and is now accepted as an important aspect of model development that should be documented as part of a model description.

Here, we outline the tuning that took place in the development of the GA7.0 configuration. Because the development of the Global Atmosphere configurations is incremental, we limit this description to developments that took place in the increment documented herein; we do not document the tuning that took place in the development of GA6 or before, but the approach used in those developments was consistent with that described here. As discussed above, the bottom-up development of individual parametrisation schemes will also include a certain amount of parameter tuning, and it is assumed that this is documented in the publications describing those parametrisations. We include here, however, where we have deliberately altered an input parameter in an existing or proposed parametrisation.

The majority of tuning performed in the development of the GA configurations is motivated by taking a subjective overview of a large number of objectives measures. These primarily consist of NWP verification scores measured against observations and analyses and climate metrics derived from comparing a large basket of mean fields and modes of model variability from present-day climate simulations with observational and reanalysis datasets. Currently, the Met Office does not run climate change simulations which involve feedbacks (such as historical simulations with time-evolving forcing) during its model development process. It does, however, perform effective radiative forcing (ERF) tests. Proposed scientific developments to the configuration have their individual impact tested by running low-resolution present-day atmosphere/land-only simulations on both NWP and climate timescales. The impact of each change is assessed and recorded, and any unexpected or severely detrimental impact may lead the GA development team to reject a change. At this stage, we might recommend the retuning of individual parameters, although no such tuning was performed on the changes accepted into GA7.

In the next stage of development, we study the combined impact of changes by building up collections (or packages) of changes into development configurations and assess these at both NWP and climate timescales. In the development of these packages, and in particular in the final stages before the definition of the final configuration, there are two schemes that are routinely retuned because of their sensitivity to both uncertain input parameters and changes in other aspects of the model. The mineral dust emission scheme is highly sensitive to changes in surface roughness or near-surface winds. Whilst the parametrisation described in Woodward (2011) is based on detailed studies of the process of mineral dust lofting, the mapping of the model's grid-box and time-step mean values of parameters such as the near-surface friction velocity or uppermost soil level moisture content onto point-like, instantaneous surface-layer values relies on the use of arbitrary scaling parameters. These are tuned to emergent observable quantities such as dust aerosol optical depth and near-surface concentrations in instrumented locations. Similarly, for the non-orographic GWD scheme described in Sect. 2.7, there is no a priori estimate for the amplitude of launched gravity waves required to represent the breaking of sub-grid waves and those on larger scales that have been unrealistically damped by the model's large-scale dynamics. Instead, this is tuned so that the period of the model's QBO matches that observed in reanalyses. The tuning applied to the dust scheme and the non-orographic GWD scheme is described in Table 6.

When package configurations contain errors that are deemed not to be acceptable in the final configuration, or appear to be due to an imbalance between individual changes in the package, we consider either retuning the model's input parameters or, where appropriate, implementing additional developments proposed for later model upgrades that were not ready (or not considered high enough priority) when planning the scope of the current release. In this tuning, however, we still insist that parameters are altered only within the estimation of their uncertainty and with the agreement of the parametrisation developers. When the problem being addressed is one of balance (e.g. the balance between TOA incoming SW and outgoing SW and LW radiation) we try to improve the balance by altering the component of the budget that we believe is most in error, ideally in the geographical region that has the largest local error. We try not to bring the model into balance by adjusting standard "tuning knobs" that affect these balances, such as a global scaling to model cloud amounts. In the development of GA7, one measure that caused particular concern was the climatological temperature and humidity bias in and above the TTL. Hardiman et al. (2015) discuss the importance of this bias and the role of various physical and numerical processes in its development. In developing GA7, the introduction of consistent ice optical and microphysical properties (GA ticket #17) was originally proposed via the scheme described in Baran et al. (2014), and the detrimental impact on the TTL temperature bias led to the additional developments made in Baran et al. (2016). The inclusion of cubic Hermite interpolation for moist prognostic variables (as part of GA ticket #135) was motivated primarily by its reduction of moisture biases above the tropical tropopause. Also, the reduction of the adaptive detrainment in the deep convection scheme included in Table 7 was motivated by its improvement in both TTL temperature and moisture biases.

Table 6. Original GA6.0 and final GA7.0 values of parameters in schemes routinely tuned as part of GA development.

Scheme	Variable	Parameter description	GA6 value	Tuned GA7 value
Non-orographic GWD	ussp_launch_factor	Multiplicative tuning used to set the "launched spectrum-scale factor" compared to the original coded value of $3.42 \times 10^{-9}\,s^{-2}$	1.2	1.3 (N96) 1.2 (N216+)
Dust emission	horiz_d	Global (multiplicative) tuning for dust emission.	2.50	2.25
	us_am	Multiplicative tuning applied to diagnosed friction velocity on input to dust emission scheme.	1.45	1.45 (N96) 1.40 (N216+)

Table 7. Initially proposed and final values of parameters tuned to improve cloud and radiation interactions in GA7.0.

Scheme	Variable	Parameter description	Initial value	Tuned value
Boundary layer	forced_cu_fac	Scaling factor applied to in-cloud water content diagnosed for forced convective cloud in GA ticket #83.	1.0	0.5
	dec_thres_cu	Buoyancy flux threshold for cumulus sub-cloud layers in GA ticket #83.	Not used.	0.05
	zhloc_depth_fac	Fraction of the cloud layer through which to continue a test on the Richardson number, used to diagnose a "shear dominated" BL (Bodas-Salcedo et al., 2012).	0.3	0.4
Large-scale cloud	two_d_fsd_factor	1-D–2-D conversion factor used in calculation of the fraction standard deviation (f) in GA ticket #15.	1.414	1.5
	cff_spread_rate	Cirrus spreading rate (r) discussed in GA ticket #98.	$1 \times 10^{-9} s^{-1}$	$1 \times 10^{-5} s^{-1}$
	mp_dz_scal	Scaling factor for the mixing length in GA ticket #120 (labelled β_1 in Furtado et al., 2016).	2.0	1.0
Convection	r_det	"Adaptiveness" of the detrainment scheme used for deep convection (Derbyshire et al., 2011).	0.9	0.8
	cca_sh_knob	Fraction of diagnosed shallow convective cloud amount passed to the radiation scheme to represent the convective core in GA ticket #44.	0.5	0.2

All other parameters tuned in the development of GA7.0 are also included in Table 7. The majority of these changes were designed to reduce the reflectivity of Northern Hemisphere low cloud (and hence reduce present-day climatological biases in reflected SW radiation) whilst maintaining the improved reduction in a positive surface SW radiation bias in the Southern Hemisphere (described in Sect. 4). The asymmetry in the SW radiation biases in both GA6 and GA7 is discussed in more detail below. The tuning of the adaptive detrainment parameter r_det, however, highlights the final aspect of tuning, which is tuning in the context of the coupled model. Like most coupled modelling centres, the Met Office primarily develops their atmospheric model to perform optimally when forced by observed sea surface temperatures (SSTs) and develops their ocean model to perform optimally with observed atmospheric fluxes. We run the coupled model routinely during the development of the component models, so as to monitor the impact of component model development on the coupled system, and we also accept that there is often a requirement of tuning the coupled model. At the point of this tuning, however, we aim not to degrade the fidelity of the uncoupled component models. The main atmospheric tuning motivated by the performance of the coupled model was the value of r_det = 0.8. Reducing this as far as 0.7 improved the TTL temperature biases but degraded the SSTs of the coupled model in the North Pacific due to its impact on the atmospheric turbulent fluxes. The final compromise value included in Table 7 was found to still give some improvement to the TTL biases whilst keeping the North Pacific biases within an acceptable range.

4 Model evaluation

4.1 General climatological assessment

The assessment of GA7.0/GL7.0 is performed by testing the new configuration in a large number of systems, many of which are listed at the end of this paper in Table 9. For the purpose of this paper, we focus on assessing the model in atmosphere/land-only climate simulations and forecast-only NWP case studies. A top-level summary of the impact of the new configuration on the model's climatology is presented in Fig. 12. This shows normalised assessment criteria (i.e. the ratio of spatial RMSE for a number of time-meaned fields) from a pair of 27-year atmosphere/land-only climate simulations at N216 resolution (≈ 60 km in the mid-latitudes).

In general, the quality of the simulation according to these measures is fairly similar to that in GA6.0, with the majority of measures that are outside the range of observational uncertainty changing by less than 15 %. The fields that lie furthest from the observations, i.e. where the difference between the model and the observations is much larger than the observational uncertainty, continue to include the model's tropical precipitation rates. This is in contrast to the extratropical precipitation rates, where the spatial disagreement between the model's mean precipitation and observations is smaller than the spatial difference between observational datasets. There is a small improvement in the errors over tropical land (where the error in GA6 is most in disagreement with the observations) but a small increase in the error over the ocean.

Figure 13 shows the annual mean precipitation rate compared to the Global Precipitation Climatology Project (GPCP), which is the primary precipitation climatology used in Fig. 12. This shows a reduction in the intensity of oceanic precipitation along the intertropical convergence zone (ITCZ), with an increase in precipitation over tropical land. This redistribution of precipitation from tropical ocean to tropical land is generally an improvement, but the hydrological cycle of the model remains too active, with the global mean precipitation rate of $3.16\,\mathrm{mm\,day^{-1}}$ being outside the range of observational estimates of between $2.61\,\mathrm{mm\,day^{-1}}$ (Adler et al., 2003) and $3.12\,\mathrm{mm\,day^{-1}}$ (Legates and Willmott, 1990b). Also, there are some regions, such as the maritime continent, where these changes are not an improvement; this will be discussed in more detail below.

One of the larger impacts on the model's climatological large-scale circulation comes from the introduction of the 6A convection scheme in GA ticket #64. As discussed in Sect. 3.7.1, the more accurate iterative detrainment calculation allows the deep convection to be deeper, and hence the upper branch of the Hadley circulation (i.e. the divergent flow returning air poleward from the top of convection in the ITCZ) reaches slightly higher up in the atmosphere. Figure 14 shows the zonal mean of the JJA meridional wind from the N216 atmosphere/land-only climate simulations discussed above. In this season, the ITCZ is in its northernmost position, and the strongest branch of the Hadley circulation is to the south of this over the Equator. The difference between the two simulations shows that there is reduced southerly flow in the lower half of the returning circulation (i.e. below 200 hPa), which improves the bias vs. ERA-Interim. Above this, there is a small signal that the deepest convection is slightly deeper, as the weak bias in the returning flow is reduced in GA7.0. However, there is also a signal that there is some reduction in the weak bias in the lowest regions of the returning flow below 300 hPa, which suggests a beneficial increase in the variability in the height of the outflow from deep convection.

Most of the physics changes described in Sect. 3 have an impact on either the simulation of cloud or its interaction with the model's radiation schemes. Williams and Bodas-Salcedo (2017) present a detailed evaluation of the model's cloud fields by comparing a large number of cloud diagnostics with three-dimensional satellite data and synoptic observations. They note that GA7.0 significantly reduces the amount of thin, often sub-visual cirrus cloud which, in GA6.0, was extended from thicker cloud through overactive cirrus spreading; this is improved in GA7.0 via GA ticket #98. There is a reduction in excessive hydrometeor fraction in the mid-latitude boundary layer, which is largely due to the removal of excess drizzle by the new warm rain microphysics (GA ticket #52). Finally, they note that whilst the GA7.0 simulation of stratocumulus cloud is reasonable, there is too little moderately reflective cloud and too much optically thick cloud in these regions, which results in the in-cloud albedo being generally too high. Both the large amount of cirrus cloud and the excess drizzle in GA6 are problems that have previously been noted by operational forecasters using output from the UM, so we expect these problems to be improved when a configuration based on GA7 is implemented.

The net impact of these cloud changes on the top-of-atmosphere SW radiation fields is shown in Fig. 15, which compares the reflected SW from the N216 climate simulations discussed above.

The impact of GA7.0 is generally beneficial with a reduction in both the largest positive biases in the tropics and the widespread negative bias over the Southern Ocean. The low bias in reflected SW over the Southern Ocean in both GA6.0 and GA7.0 contributes to a large SST bias in this region in coupled model simulations. In coupled simulations using GA6.0 (not shown) these biases locally reach values as large as 6 K, which made us designate this as a critical error in GA6.0. This is significantly improved in coupled simulations using GA7.0, which are discussed in more detail in Williams et al. (2018). Both the bottom panels of Fig. 15 highlight the issue of asymmetry between the SW errors in the Northern and Southern hemispheres; in general, simulations with GA6.0 show too much reflected SW in the Northern Hemisphere and too little in the Southern Hemisphere.

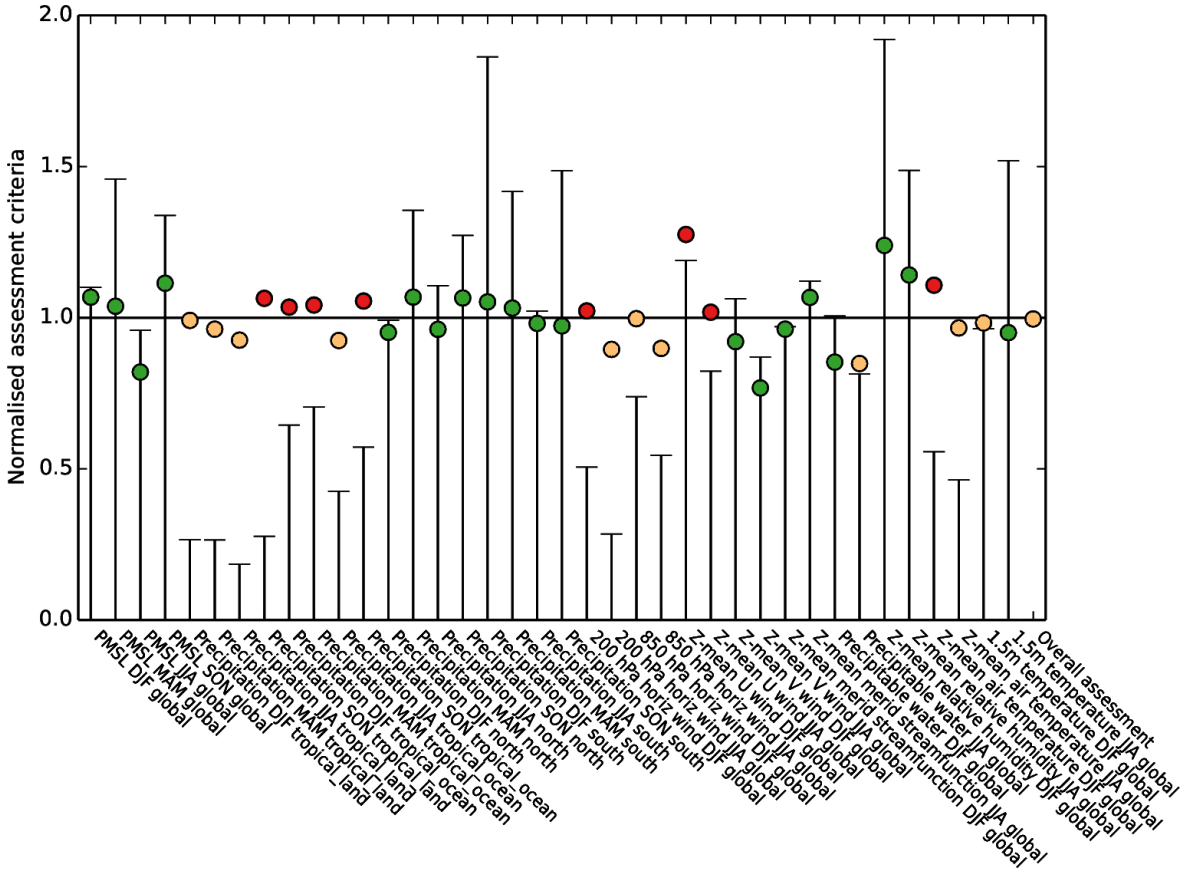

Figure 12. Normalised assessment criteria (ratio of mean field RMSEs) for a number of atmospheric fields from a GA7.0/GL7.0 atmosphere/land-only climate simulation at N216 horizontal resolution compared to an equivalent simulation using GA6.0/GL6.0. Statistics shown are for seasons DJF, MAM, JJA and September–November (SON) and for global, tropical land (land points between 30° N and 30° S), tropical ocean (sea points between 30° N and 30° S), north (30–90° N) and south (30–90° S) regions. The observation datasets used are HadSLP2 pressure at mean sea level (Allan and Ansell, 2006), GPCP precipitation (Adler et al., 2003), SSMI precipitable water (Wentz and Spencer, 1998) and CRUTEM3 1.5 m temperature (Brohan et al., 2006), whilst the remaining climatologies are from ERA-Interim reanalyses (Berrisford et al., 2009). The whisker bars are observational uncertainty, which is calculated by comparing these with alternative datasets; these are ERA-40 pressure at mean sea level and precipitable water (Uppala et al., 2005), CMAP precipitation (Xie and Arkin, 1997), Legates and Willmott (1990a) 1.5 m temperature and MERRA reanalyses for everything else (Bosilovich, 2008). Green circles denote fields for which the RMSE lies within observational uncertainty, whilst light orange or red circles denote fields for which the RMSE is not within observational uncertainty and for which the RMSE is improved or degraded respectively.

This is slightly improved in GA7.0, with a larger increase in reflected SW over the Southern Ocean than over the North Pacific and North Atlantic, but as discussed in Sect. 3.11, this required some care during the tuning of the final configuration, and there are still slight increases in error over these Northern Hemisphere oceans. An important component of the Southern Ocean bias is believed to be due to microphysical processes, in particular to a shortfall in the amount of supercooled liquid water. This is represented slightly better in GA7.0 with the turbulent production of liquid water in mixed-phase cloud (GA ticket #120), but the model still converts the resulting liquid water too quickly into ice, which is a subject of ongoing research. More recently, the strength of the aerosol–cloud interaction has also been highlighted as an important contributor to this asymmetry. This is discussed in more detail in Sect. 4.5. Figure 16 shows the equivalent plot for outgoing LW radiation.

Generally, the impacts are smaller than in the SW, although there is a small increase in the global mean OLR (of about $1.5\,\mathrm{Wm}^{-2}$); this improves the bias versus the Clouds and the Earth's Radiant Energy System (CERES) Energy Balanced and Filled (EBAF) dataset over the sea but increases the bias over tropical land. The exception to this is the Indian subcontinent, which is significantly improved and will be discussed in more detail below.

The combined impact of changes to the top-of-atmosphere radiation budget (and other processes) on the model's temperature structure are shown in Fig. 17.

This shows the annual mean GA6.0 and GA7.0 temperature biases versus ERA-Interim both in the N216 simula-

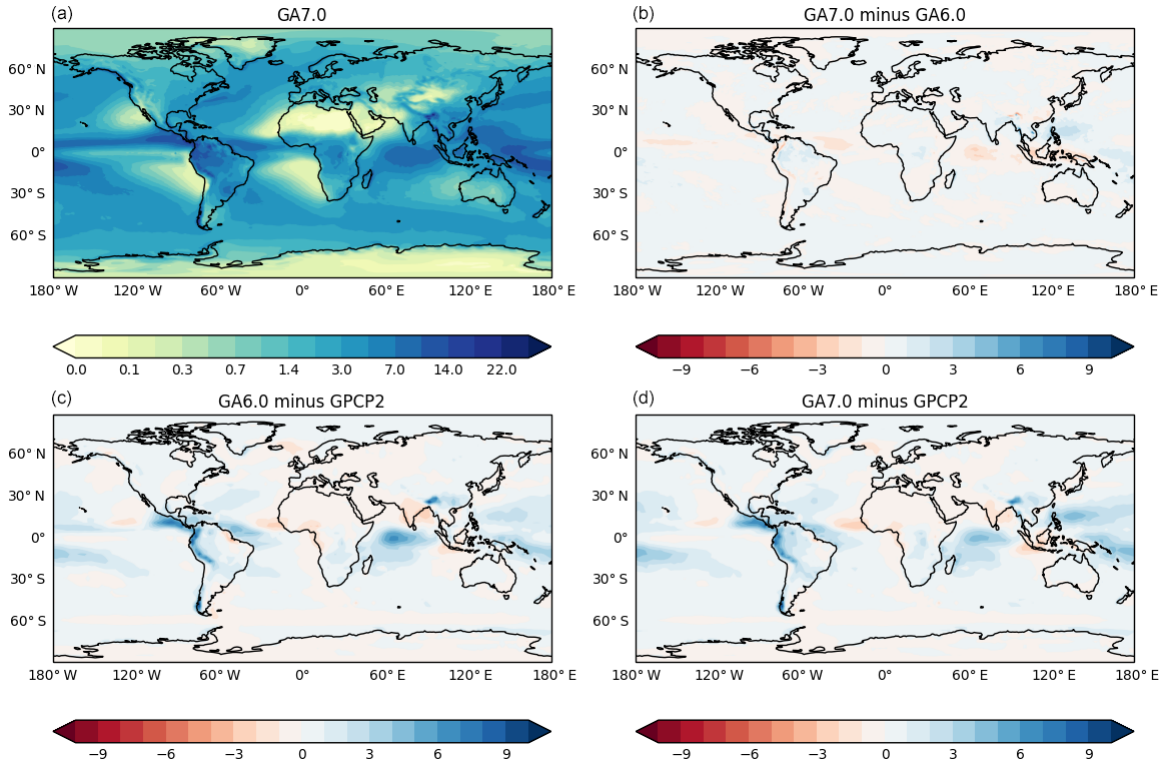

Figure 13. Annual mean precipitation rate ($\mathrm{mm\,day^{-1}}$) in the N216 atmosphere/land-only climate simulations presented in Fig. 12, showing GA7.0 **(a)**, the difference from GA6.0 **(b)**, and the bias compared to GPCP observations in GA6.0 **(c)** and GA7.0 **(d)**.

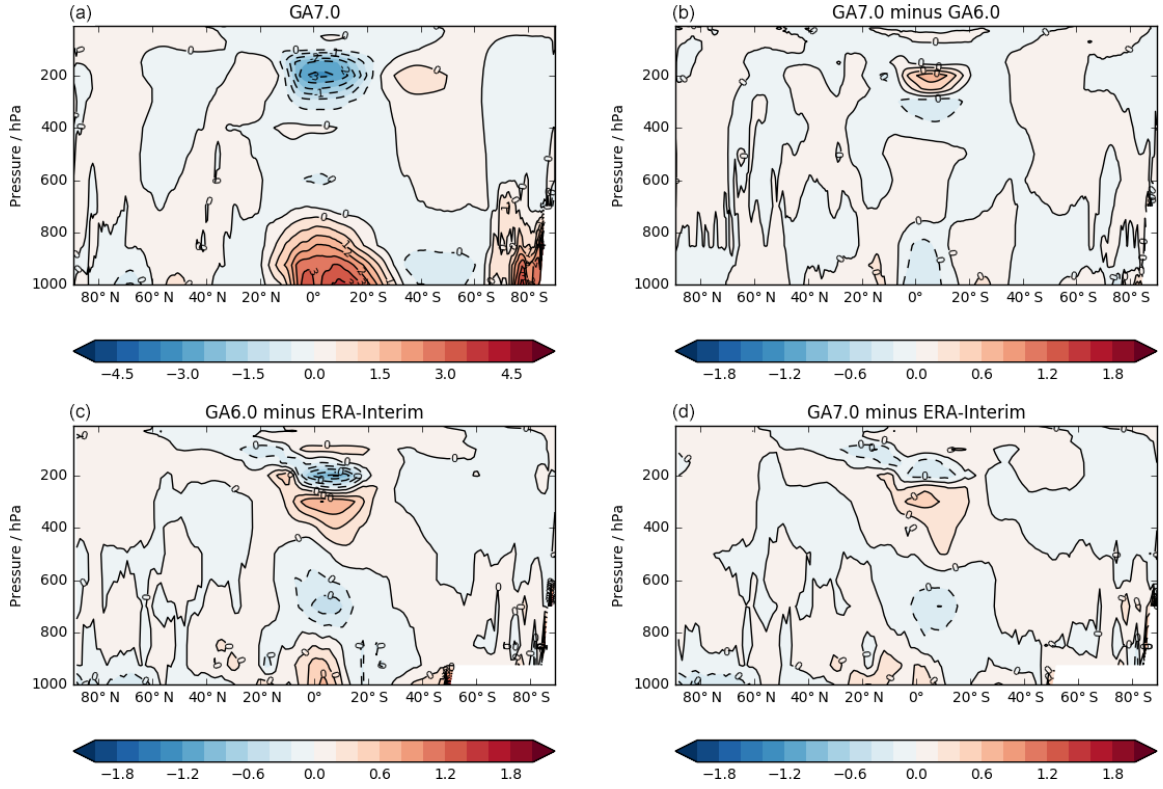

Figure 14. Zonal and time mean of the JJA meridional wind ($\mathrm{m\,s^{-1}}$) in the N216 atmosphere/land-only climate simulations presented in Fig. 12 compared to ERA-Interim reanalysis. The layout is the same as in Fig. 13.

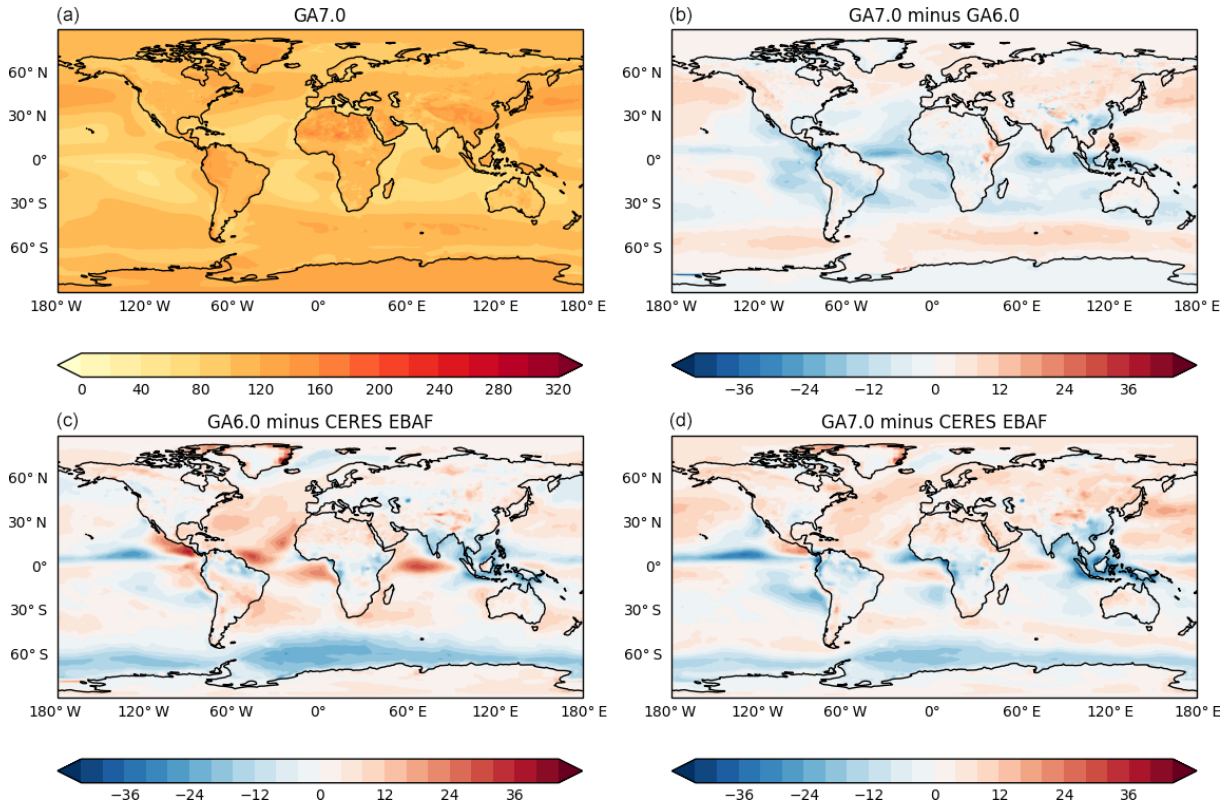

Figure 15. Annual mean top-of-atmosphere reflected SW radiation ($W\,m^{-2}$) in the 27-year N216 atmosphere/land-only climate simulations presented in Fig. 12 compared to Clouds and the Earth's Radiant Energy System (CERES) Energy Balanced and Filled (EBAF) dataset (Loeb et al., 2009). The layout is the same as in Fig. 13.

tions discussed above as well as in an equivalent pair of atmosphere/land-only climate simulations at N96 resolution ($\approx$ 135 km in the mid-latitudes). There is a consistent signal of GA7.0 being warmer than GA6.0 throughout the troposphere, which brings the model's climatology into better agreement with a number of reanalysis datasets. This comes from a combination of a number of changes in GA7.0, but the reduction in the upper-tropospheric cold bias, particularly in the tropics, is largely due to the improved numerics in the 6A convection scheme. This removes a long-standing bias in the model's temperature structure, which has been present for a number of development cycles. Near the tropical tropopause, the impact of GA7.0 on the temperature structure is more complicated; we discuss this in more detail in Sect. 4.3.

4.2 Aspects of the climatology improved through stochastic physics

As discussed in Sect. 3.10, the inclusion of the stochastic physics package in GA7.0 means that for the first time, these schemes will be used in long-range climate projections using a standard UM science configuration. In addition to improving the variability of the model, particularly as measured by the spread in an ensemble of predictions, these schemes also have an impact on the mean climatology (Sanchez et al., 2016).

Some of these improvements are highlighted by Fig. 18, which shows the mean JJA precipitation biases versus GPCP in the tropical eastern hemisphere. Over India and the Indian Ocean, we see an improvement in the long-standing bias of too much precipitation over the ocean and too little precipitation over the subcontinent. This improves another critical error in GA6.0, which has been particularly poor for a number of GA releases; whilst these regions stand out as needing further improvement, in N96 atmosphere/land-only simulations, these biases are now the smallest they have been since before the definition of Global Atmosphere 3.0 (Walters et al., 2011). Whilst the largest contribution to this improvement comes from the stochastic physics package, there were also contributions from other changes including the 6A convection scheme (GA ticket #64) and the improved warm rain microphysics (GA ticket #52). One region where we see an increase in the dry bias over tropical land in GA7.0 is over the Maritime Continent. These degradations with GA7.0 appear to be mostly due to a general shift in the precipitation patterns, both the general (and elsewhere) beneficial decrease in precipitation in this region due to the inclusion of stochastic physics, and a general (and elsewhere) beneficial decrease

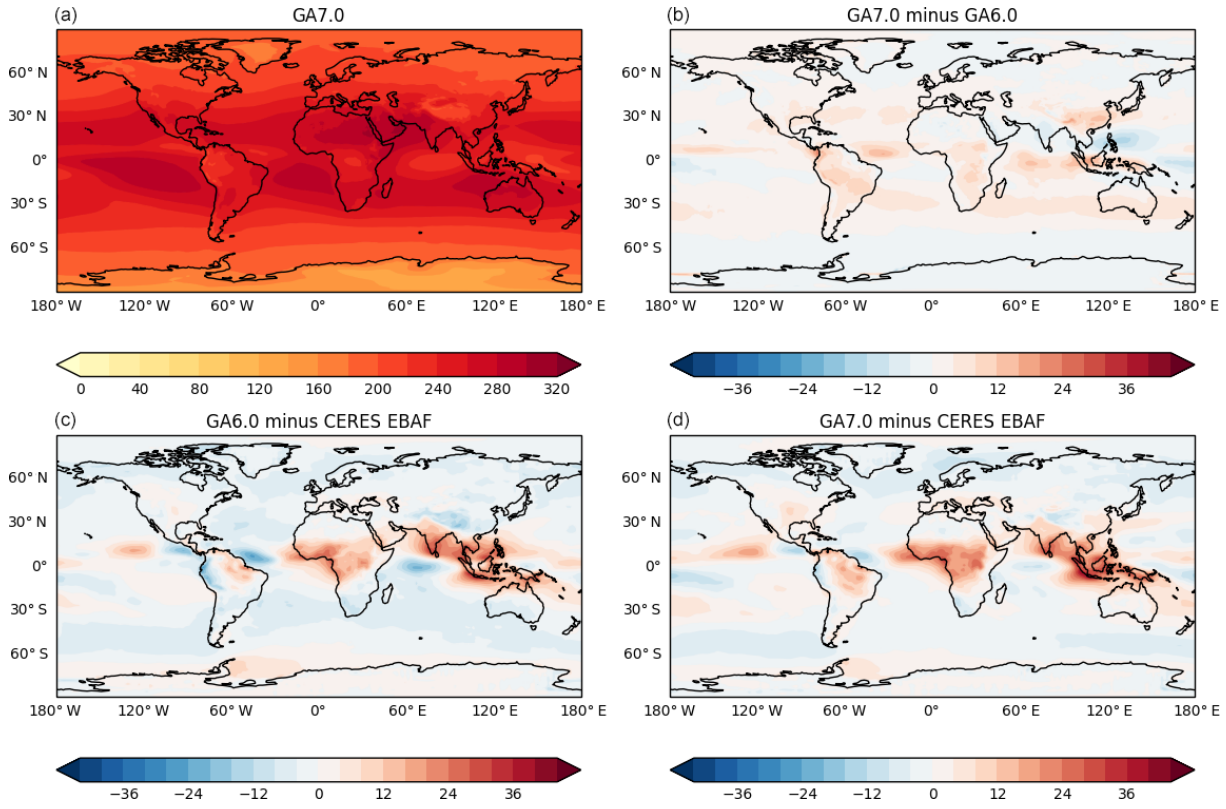

Figure 16. Annual mean top-of-atmosphere outgoing LW radiation ($W\,m^{-2}$) using the same simulations, observational dataset and layout as Fig. 15.

in precipitation over tropical land from the interaction of the convective cores with the radiation scheme (through GA ticket #44). We do not believe that these changes are due to degrading the underlying processes that cause this bias, which have been shown elsewhere to be related to more locally pertinent issues such as the representation of sea breezes and the interaction of the convection scheme with the model's smoothed mean orography (Birch et al., 2015; Rashid and Hirst, 2017).

Over Africa, the inclusion of stochastic physics leads not only to an improvement in the precipitation biases, as seen in Fig. 18, but also to a beneficial increase in the number of African easterly waves (AEWs).

Figure 19 shows the number of AEWs identified per season (July–September) from the 27-year atmosphere/land-only climate simulations discussed above. This shows that in GA7.0, the number of AEWs is in better agreement with ERA-Interim and also shows a slightly reduced resolution sensitivity; as a result, the mean number of AEWs identified in an N96 simulation with GA7.0 is greater than the number from an N216 simulation with GA6.0. Despite this improvement, there are still persistent biases in the mean state over northern Africa, such as too broad an African easterly jet and too southern a position for the continental ITCZ. This has an effect on the characteristics of AEWs, and the convection parametrisation is still not sensitive enough to the dynamics of the wave and associated moisture convergence, which results in deficiencies in the representation of the convection-circulation interaction and related wave growth (Tomassini et al., 2017).

4.3 Tropical tropopause layer biases and energy conservation

In the troposphere, Fig. 17 shows a consistent impact on the climatological temperature profile at both N96 and N216, with both resolutions being warmer in GA7.0, reducing the cold bias versus ERA-Interim. In the TTL, however, we see a contradictory signal, with a decreased warm bias at N96 but an increased warm bias at N216.

To understand this, let us first concentrate on the impact at N96. Hardiman et al. (2015) describe the TTL temperature and stratospheric water vapour biases in N96 GA6.0 simulations and show that the presence of a warm bias in the TTL was a common feature amongst many of the models that were submitted to CMIP5. This warm bias is closely associated with a moist bias in the stratosphere due to not enough moisture being freeze-dried out of air ascending through the coldest point in the vertical temperature profile. This can prove to be a particular problem in models with interactive chem-

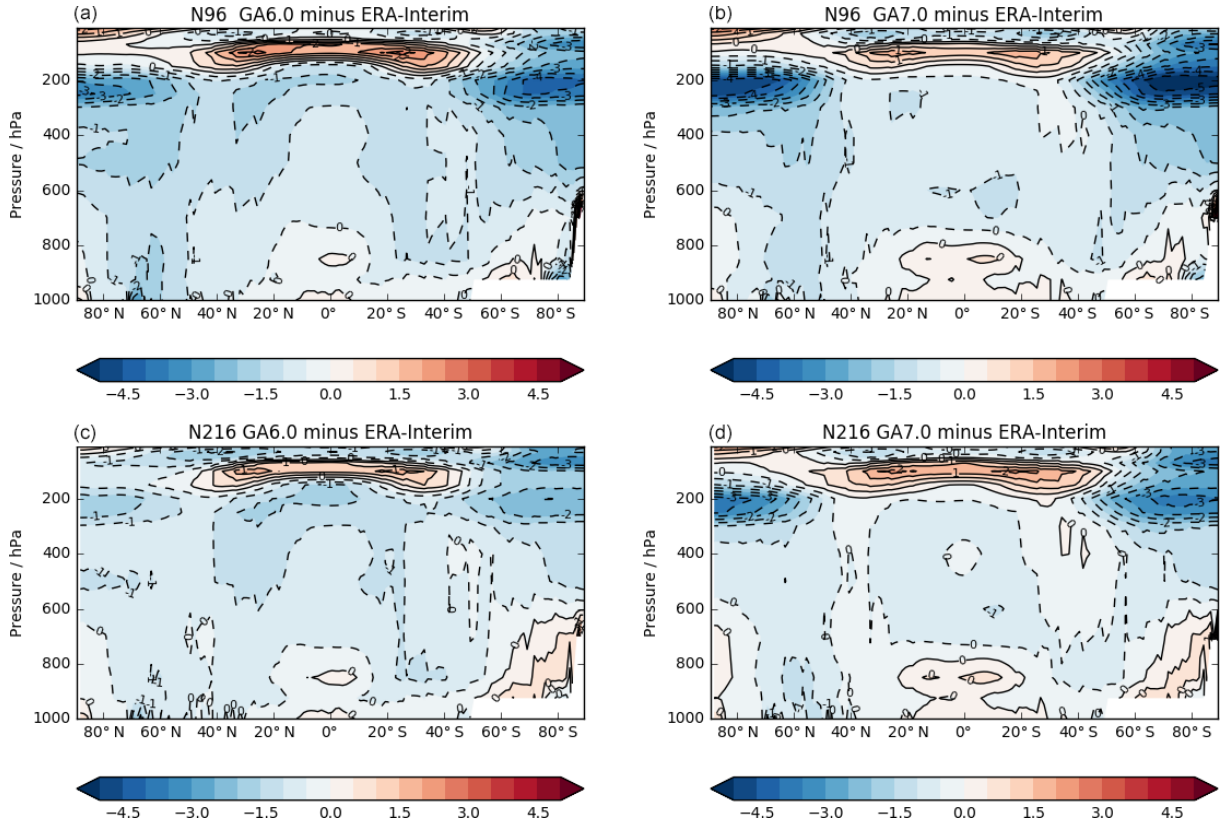

Figure 17. Annual mean zonal mean temperature biases (K) versus ERA-Interim in the 27-year N216 atmosphere/land-only climate simulations presented in Fig. 12 alongside results from equivalent simulations performed at N96 resolution. The rows show data from N96 **(a, b)** and N216 **(c, d)**, whilst the columns are data from GA6.0 **(a, c)** and GA7.0 **(b, d)**.

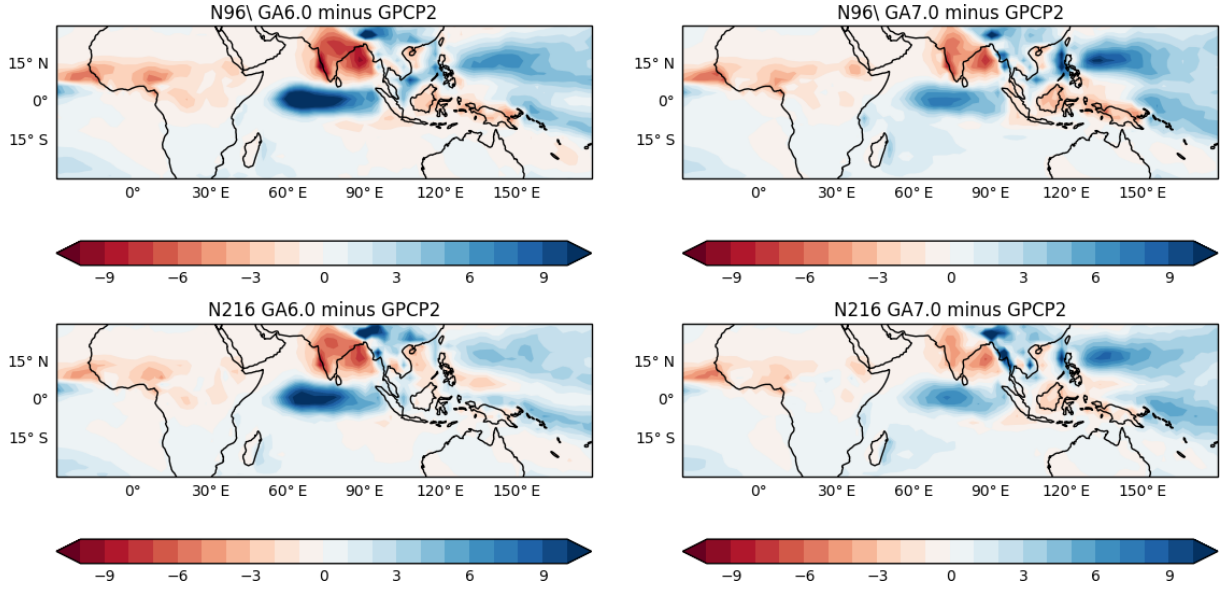

Figure 18. JJA precipitation rate biases versus GPCP over the Indian Ocean and the maritime continent (mm day^{-1}) from 27-year N96 and N216 atmosphere/land-only climate simulations of GA6.0 and GA7.0. The layout is the same as in Fig. 17.

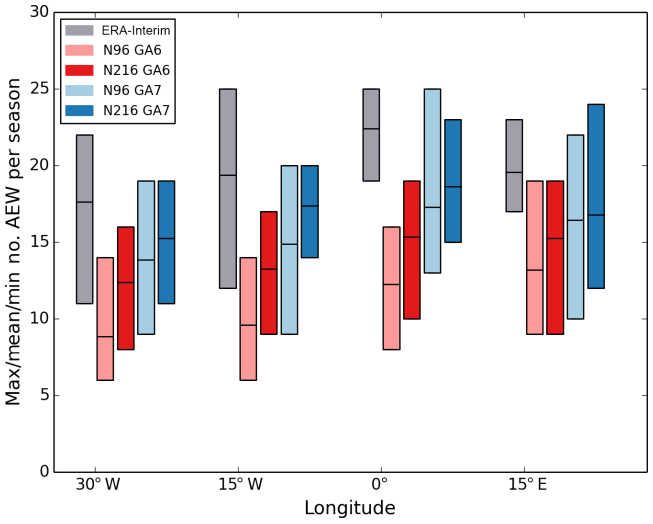

Figure 19. Average, maximum and minimum number of African easterly waves (AEWs) tracked per year (between July and September) in the 27-year N216 atmosphere/land-only climate simulations presented in Fig. 12 alongside results from equivalent simulations performed at N96 resolution. These waves are identified and tracked using the algorithm described in Bain et al. (2013).

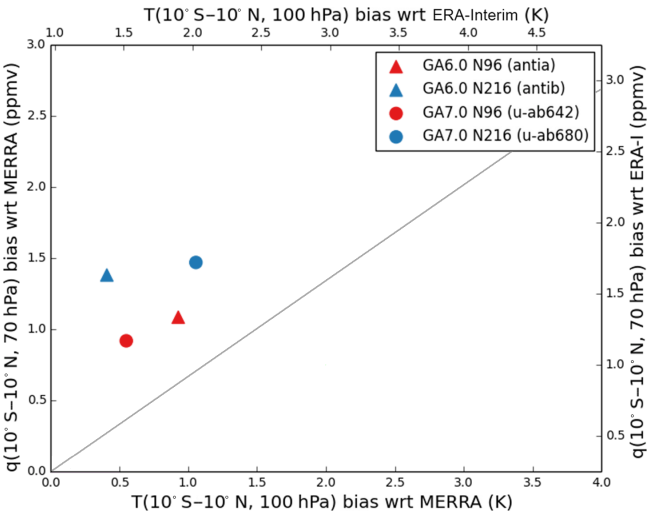

Figure 20. Tropical tropopause layer temperature biases and lower stratospheric humidity biases from 27-year N96 and N216 atmosphere/land-only climate simulations of GA6.0 and GA7.0 versus MERRA and ERA-Interim reanalyses (following Hardiman et al., 2015).

istry, as a stratospheric moisture bias can induce a bias in the ozone field, which in turn can feed back to further increase the warm bias. This was designated as a critical error in GA6.0, particularly at N96 resolution, which is the resolution at which the CMIP6 simulations of UKESM1 (with interactive chemistry) will be performed. Hardiman et al. (2015) developed a metric to measure the impact of model changes on TTL temperature and stratospheric moisture biases and demonstrated the impact of many of the changes proposed for inclusion in GA7.0. Reproduced for the simulations described above in Fig. 20, this compares the annual mean tropical temperature bias at 100 hPa (as a proxy for the bias in the "cold point" temperature) and the tropical specific humidity bias at 70 hPa (as a measure of the bias in moisture passing through the cold point into the lower stratosphere).

A careful monitoring of the impact of these changes, alongside the tuning described in Sect. 3.11, allowed us to ensure that the bias is improved in N96 simulations of GA7.0 to the extent that we do not expect a strong ozone feedback in UKESM1.

At resolutions of N216 and above, the impact of GA7.0 on the TTL bias is complicated by the inclusion of the conservation of mass-weighted potential temperature (GA ticket #146). As discussed in Sect. 3.1.2, this change removes a spurious positive source of energy, which was known to increase in magnitude with increasing model resolution. In GA6.0 climate simulations, this energy source was compensated by the global energy correction described in Sect. 2.13. The magnitude of this energy correction term is monitored

Table 8. Mean value of the global energy correction applied over the 27-year simulations at N96 and N216 presented above.

Global energy correction (Wm^{-2})			
Config.	N96	N216	N512[a]
GA6.0	−0.79	−2.72	−3.68
GA7.0	−0.61	−0.49	−0.27

[a] We also include the results from some shorter N512 resolution simulations using GA6.0 and GA7.0, which ran for 13 and 10 years respectively. These should be comparable, as this measure is stable to $\mathcal{O}(0.1\,Wm^{-2})$ in simulations of only a few years in length.

in all simulations and is usually expected to be $\mathcal{O}\pm(0.5$–$1.0)\,Wm^{-2}$.

Table 8 shows that whilst this is true at N96, in GA6.0 simulations at higher resolutions, the response of the energy correction scheme to the error in the temperature advection leads to the scheme being much more active, which was also designated as a critical error in GA6.0. The improved temperature advection reduces this sensitivity and hence addresses this problem. When the energy correction scheme stays within its expected bounds, its impact (not shown) is small enough not to significantly affect the model's climatology. In N216 simulations of GA6.0, however, the atmospheric cooling associated with the $\approx -2.5\,W\,m^{-2}$ correction was big enough to cool the TTL and spuriously reduce the warm bias. This means that the net impact of all the GA7.0 changes at N216, as seen in Figs. 17 and 20, is to increase the TTL warm bias at this resolution.

4.4 Predictive skill in short-range forecasts

The primary assessment of the predictive skill of NWP forecasts using GA7.0 has been performed using forecast-only "case studies" initialised from independent analyses. Figure 21 is a top-level summary of the difference in the RMSE between GA7.0 and GA6.0 for a number of fields and forecast ranges in a set of case studies at N768 resolution ($\approx$ 17 km in the mid-latitudes) and initialised from operational ECMWF analyses on 24 synoptically independent dates.

The RMSE for each field and forecast range is calculated against synoptic surface and radiosonde observations at the observation location and against verifying analyses on a common 2.5° global grid. When verifying against analyses, the ECMWF analysis fields are first converted into native UM prognostics, which are then used to calculate the various diagnostic fields; this ensures consistency both with the way in which the forecasts are initialised and with the way that particular diagnostics (e.g. PMSL) are calculated, which is particularly important in regions of high orography. The figure shows that the number of fields improved outweighs the number of fields degraded. In particular, there are improvements in Northern Hemisphere PMSL and 500 hPa geopotential height, which is primarily due to improved insulation of the surface under lying snow in DJF. There are also improvements to temperatures at 250 hPa, but mixed signals at lower levels. As with the model's long term climatology, the impact of GA7.0 on the model's short-range temperature error structure is complicated. Figure 22 shows the tropical temperature error profile calculated from both radiosonde observations and verifying analyses.

At 100 hPa we see the same improvement in the TTL warm bias seen in N96 climate simulations in Fig. 17; although these NWP forecasts are at much higher horizontal resolution than N96, they do not include the energy correction term that cooled higher-resolution GA6.0 climate simulations, and hence we do not see a compensating warming in moving from GA6.0 to GA7.0. Below this, again as in Fig. 17, GA7.0 is warmer than GA6.0 throughout most of the troposphere. Between 100 and 200 hPa this warming appears to be too great, but throughout most of the rest of the troposphere this is an improvement to a long-standing tropospheric cold bias. The exception to this is at 700 hPa, which remains too cool in GA7.0. Ujiie et al. (2017b) show that this cold "spike" is due to an overly simple representation of the melting of convective precipitation at the freezing level and propose improvements to this that will be implemented in a future GA release. The impact of GA7.0 on the general circulation is also similar between the model's long-range climatology and these short-range NWP forecasts. Figure 23 shows the tropical horizontal wind error profile from radiosonde observations and verifying analyses.

There is a decrease in the horizontal wind speed at 200–250 hPa and an increase in the horizontal wind speed at 100 hPa, which is consistent with higher divergent outflows due to deeper convection in the 6A convection scheme. This leads to an apparently large improvement in the 250 hPa vector wind error against analyses in Fig. 21 and a degradation in the 100 hPa vector wind error in Fig. 23. It is likely, however, that these apparent improvements and degradations are due, at least in part, to the characteristics of the UM becoming more or less like those of the forecast model used in generating the ECMWF operational analyses.

To make a more quantitative assessment of the performance of GA7.0 in short-range NWP forecasts, we would usually perform "assimilation trial" forecasts using a 4-D-Var or hybrid 4-D-Var data assimilation cycle based on the Met Office operational global analysis system (Clayton et al., 2013). Indeed, such trials were used during the early-to-middle stages of developing GA7.0/GL7.0. Later on, however, we encountered problems in making a fair comparison between GA7.0 and GA6.0, which meant that they were not used to constrain the final stages of development. The first problem was that prior to March 2016, the Met Office analysis at 850 hPa had a tendency to be warm compared to radiosonde observations due to the details of the bias correction scheme used in assimilating satellite radiances. This has since been addressed by introducing a variational bias correction scheme (VarBC), which brings the analysed global mean 850 hPa temperature both closer to that of other NWP centres and closer to that of radiosonde observations (Ujiie et al., 2017a). The combination of a warm analysis and a climatological cold bias in the operational GA6.1/GL6.1 meant that the model's mean 850 hPa temperature would drift towards the radiosonde observations with an increasing forecast range. As a result, test forecasts of prototype GA7 configurations, with their reduced cooling at lower levels, would appear too warm when compared to radiosonde observations when initialised from either operational Met Office analyses or pre-VarBC assimilation trials. The pre-operational trials of VarBC using GA6.1 showed that the cooler analyses reduced the rate of cooling towards the model's climatology, hence significantly improving its verification against its own analysis. Trials of GA7.0 using VarBC brought the model's climatology closer to its analysed value, hence reducing this drift even more. This is illustrated in Figs. 5 and 16 of Ujiie et al. (2017a).

The second problem encountered in producing trial forecasts based on GA7.0 was in the specification of the stationary background error covariance matrix $\boldsymbol{B}_c$. Data assimilation relies on having a suitable representation of these forecast errors, incorporating model, observation, initial condition and representativity errors. $\boldsymbol{B}_c$ is calibrated from a training dataset representing typical forecast errors, and in hybrid 4-D-Var, it makes an important contribution to the background error penalty and should ideally be consistent with the model used in the assimilation cycle. In practice, however, it is usually sufficient to use a $\boldsymbol{B}_c$ based on the control model when testing a model upgrade and later produce a $\boldsymbol{B}_c$ based on the new model for consistency. In our original tests

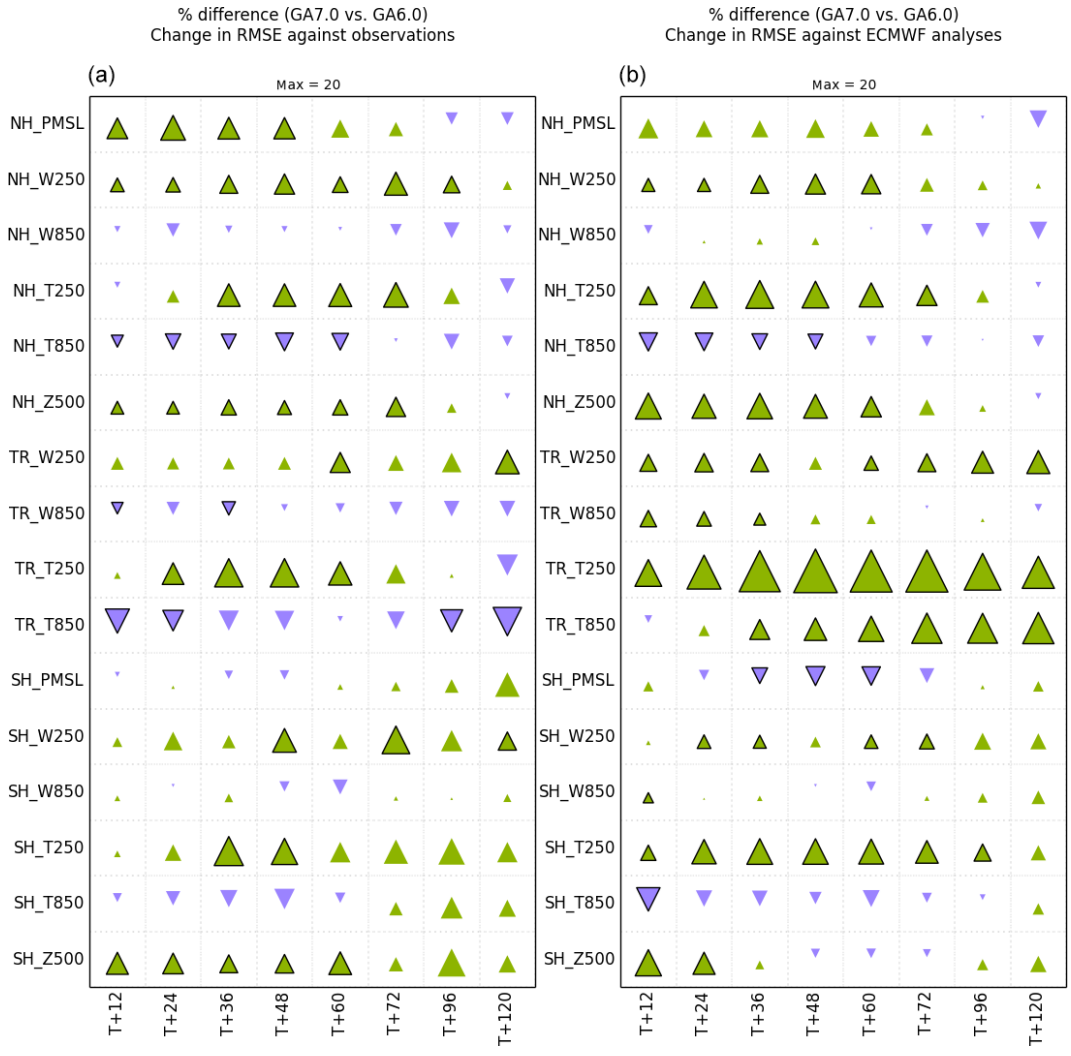

Figure 21. Percentage change in RMSE between GA7.0 and GA6.0 when verified against synoptic and radiosonde observations **(a)** and analyses **(b)** in a set of 24 N768 resolution forecast case studies run from operational ECMWF analyses. The rows represent RMSE differences for particular parameters in the Northern Hemisphere (NH), the tropics (TR) and the Southern Hemisphere (SH). The boundaries between these regions are at latitudes of ±20° for verification vs. observations and ±18.75° for verification vs analyses, which are calculated on a standard 2.5° grid. The parameters are pressure at mean sea level (PMSL), vector wind errors and temperature errors at 250 and 850 hPa (W250, W850, T250 and T850) and geopotential height at 500 hPa (Z500). The columns represent forecast ranges from 12 h (T+12) to 5 days (T+120). Green arrows pointing upwards represent a decrease in RMSE (i.e. an improvement), whilst purple down arrows represent a degradation. The area of the arrow denotes the size of the change with a 20 % change filling the width of the column, and a solid outline denotes that the change is statistically significant.

of GA7.0, this appeared not to be the case, and a series of tests (not shown) suggested that the interaction between the operational $\boldsymbol{B}_c$ and GA7.0 was detrimental to forecast performance, particularly at lead times of 2 days or less. The operational $\boldsymbol{B}_c$ was based on a training dataset produced by the ECMWF forecast model but evolved using the UM (Wlasak and Cullen, 2014), thus blending the forecast error characteristics of the two models. The impact of the covariance–model inconsistency appears to be smaller when $\boldsymbol{B}_c$ is calculated using training data produced by an experimental ensemble of four-dimensional ensemble variational data assimilations (Bowler et al., 2017; Inverarity et al., 2018), even when based on the previous GA6.1 configuration. A new $\boldsymbol{B}_c$ generated in this way will be made operational in late 2017, which we believe will allow us to revert to the strategy of staggered model and $\boldsymbol{B}_c$ updates described above. In time, the replacement of the stationary covariance matrix with one based solely on the history of recent forecasts may make it easier to test the impact of model upgrades on forecast quality.

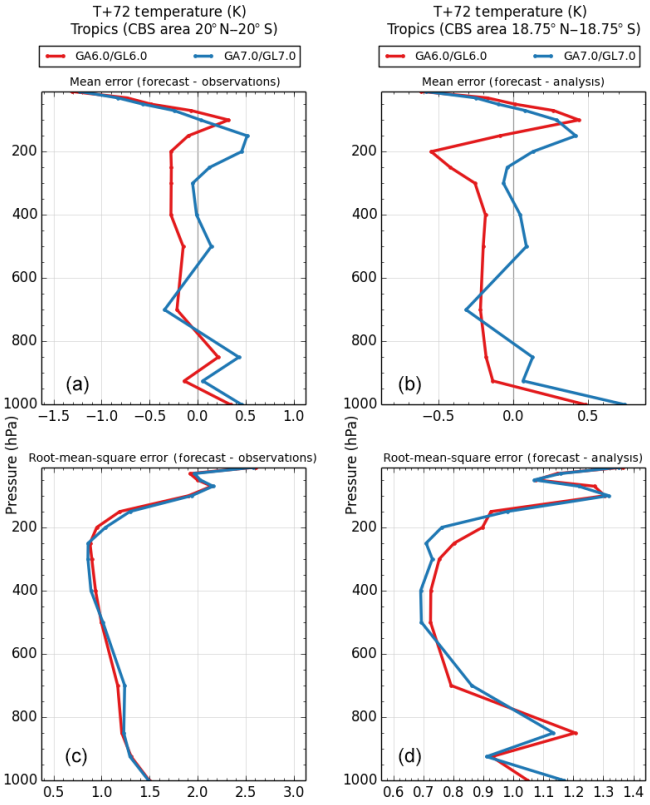

Figure 22. Profiles of 3-day (T+72) tropical temperature bias **(a, b)** and RMSE **(c, d)** versus radiosonde observations **(a, c)** and ECMWF analyses **(b, d)** from the N768 GA6.0 and GA7.0 case studies presented in Fig. 21.

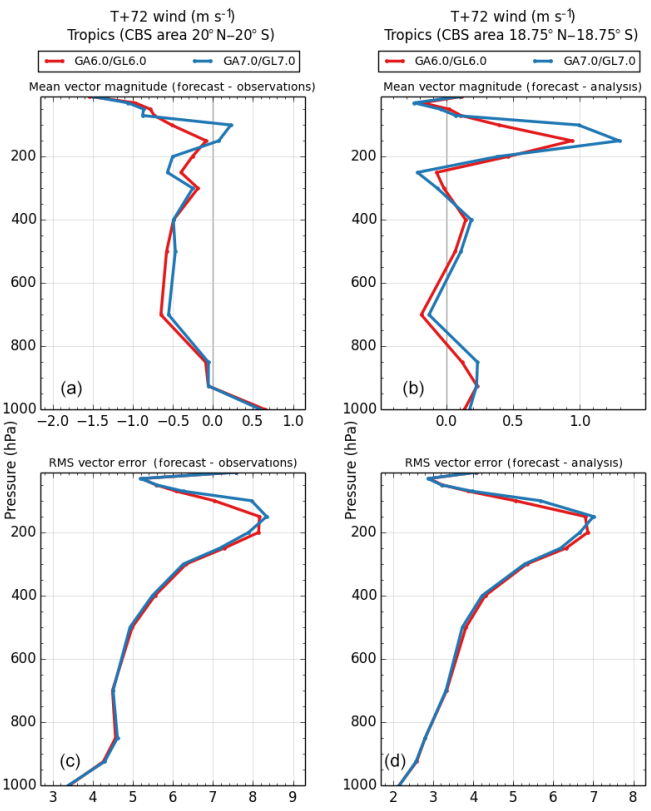

Figure 23. Profiles of 3-day (T+72) tropical wind speed bias **(a, b)** and vector wind RMSE **(c, d)** versus radiosonde observations (left) and ECMWF analyses (right) from the N768 GA6.0 and GA7.0 case studies presented in Fig. 21.

4.5 Problems identified with GA7.0/GL7.0

4.5.1 Overly low snow albedo in extremely cold conditions

The albedo of snow over land in GL7.0 is linked to the snow grain size as specified by the parametrisation of Marshall and Oglesby (1994). This leads to a rapid growth from a 50 µm grain size for fresh snow to 150 µm over a few days, even in very cold conditions below −30 °C, followed by slow grain growth for aged non-melting snow. GL7.0 thus has a lower albedo for cold snow than the temperature-dependent albedo in GL6.0. Whilst this appears to reduce the reflected SW bias versus CERES EBAF over Antarctica, as seen in Fig. 15, other evidence such as the observed radiative fluxes used in the GABLS4 (GEWEX Atmospheric Boundary Layer Study; Bazile et al., 2014) suggests that the model's Antarctic albedo of ∼ 0.78 is too low. This is consistent with snow grains growing too large, which is supported by measurements of snow specific surface area that imply grain sizes of ∼ 80 µm (Gallet et al., 2011), compared to the values of ∼ 150 µm seen in GL7.0. In NWP forecasts, this leads to a warm bias at low levels over Antarctica during austral summer, as shown in Fig. 24. In future GL releases, we plan to improve this by using the equi-temperature snow-grain-growth scheme of Taillandier et al. (2007).

4.5.2 Overly strong negative aerosol effective radiative forcing

As discussed in Sect. 3.11, the climate simulations that contributed to the development and tuning of GA7.0 were all simulations of the present-day climate. Atmosphere/land-only simulations were performed with time-varying emissions, trace gas concentrations and observed SSTs for years after 1981, and coupled simulations were performed over much longer periods but used perpetual year 2000 emissions and trace gas concentrations. Following the definition of GA7.0, however, its anthropogenic ERF was assessed over the historical period (1850–2000) in order to determine its suitability for climate change simulations. This revealed an extremely strong, negative aerosol ERF of $\approx -2.7\,\mathrm{W\,m^{-2}}$, which contributed to a total anthropogenic ERF (from greenhouse gases, aerosols, ozone and land use change) that was

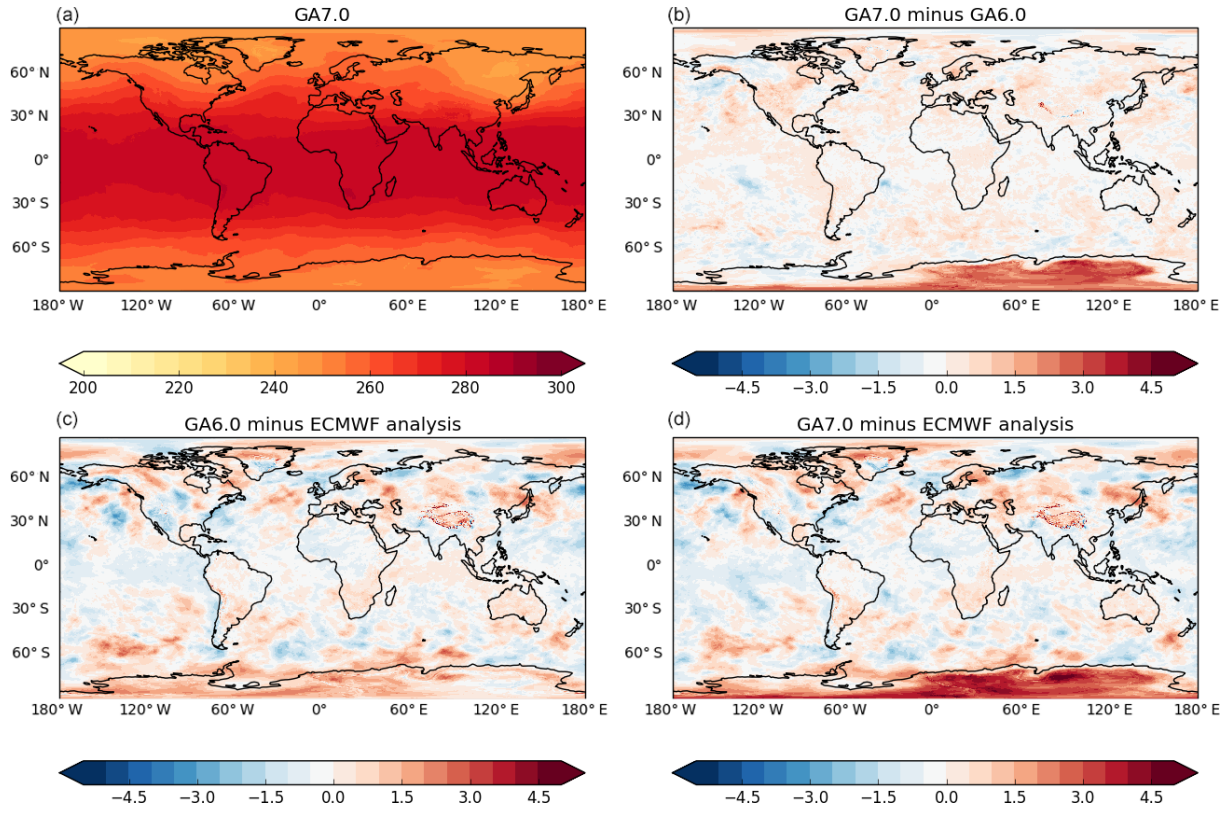

Figure 24. T+120 temperature (K) at 700 hPa meaned over the 12 pairs of forecasts included in Fig. 21 that were initialised in DJF. The panels show the mean GA7.0 forecast **(a)**, the difference between GA7.0 and GA6.0 forecasts **(b)**, and the bias compared to the verifying ECMWF analyses in GA6.0 **(c)** and GA7.0 **(d)**.

negative[4], with a value of $\approx -0.4\,\mathrm{W\,m^{-2}}$. This would have had an extremely detrimental impact on historical simulations using GA7.0. For CMIP6, this is addressed by developing the GA7.1 "branch" configuration (discussed below); beyond this, we aim to address this shortcoming by building the majority of the GA7.1 developments back into the Global Atmosphere trunk in a future release.

5 Additional developments and tunings included in the CMIP6 climate configuration Global Atmosphere 7.1

As discussed above, the very strong negative aerosol ERF in GA7.0 makes it unsuitable for use in historical climate change simulations, and hence in submissions to CMIP6. For this reason, we developed the GA7.1 branch configuration that reduced anthropogenic aerosol ERF whilst maintaining a present-day simulation similar to that from GA7.0. The aerosol ERF and subsequent development of the GA7.1 configuration, as well as the scientific justification for these developments, are fully documented in Mulcahy et al. (2018). GA7.1/GL7.0 is the atmosphere/land component of the Global Coupled model 3.1 (GC3.1) configuration (Williams et al., 2018), which will underpin the HadGEM3–GC3.1 physical model submission to CMIP6. GC3.1 will also be the physical model component of the UKESM1 Earth system model, which will also be submitted to CMIP6.

The differences between GA7.1 and GA7.0 are as follows.

1. A new parametrisation of spectral dispersion for the cloud droplet size distribution following Liu et al. (2008) was created. This parametrises the impact of the droplet number (and hence the aerosol loading) on the dispersion relation, as opposed to the simpler approach adopted in GA7.0 in which the spectral dispersion in continental and maritime cloud is specified according to the model's land sea mask (Martin et al., 1994).

2. An update was made to the complex refractive index of black carbon from $1.75–0.44i$ to the more recent estimate of $1.85–0.71i$ (Bond and Bergstrom, 2006; Bond et al., 2013).

3. More detailed lookup tables for aerosol optical properties in UKCA-Radaer were included, enabling more accurate spectral resolution of aerosol solar absorption.

[4]Chapter 8 of Working Group I's contribution to the Intergovernmental Panel on Climate Change Fifth Assessment Report (IPCC, 2013) states that "It is certain that the total anthropogenic ERF is positive."

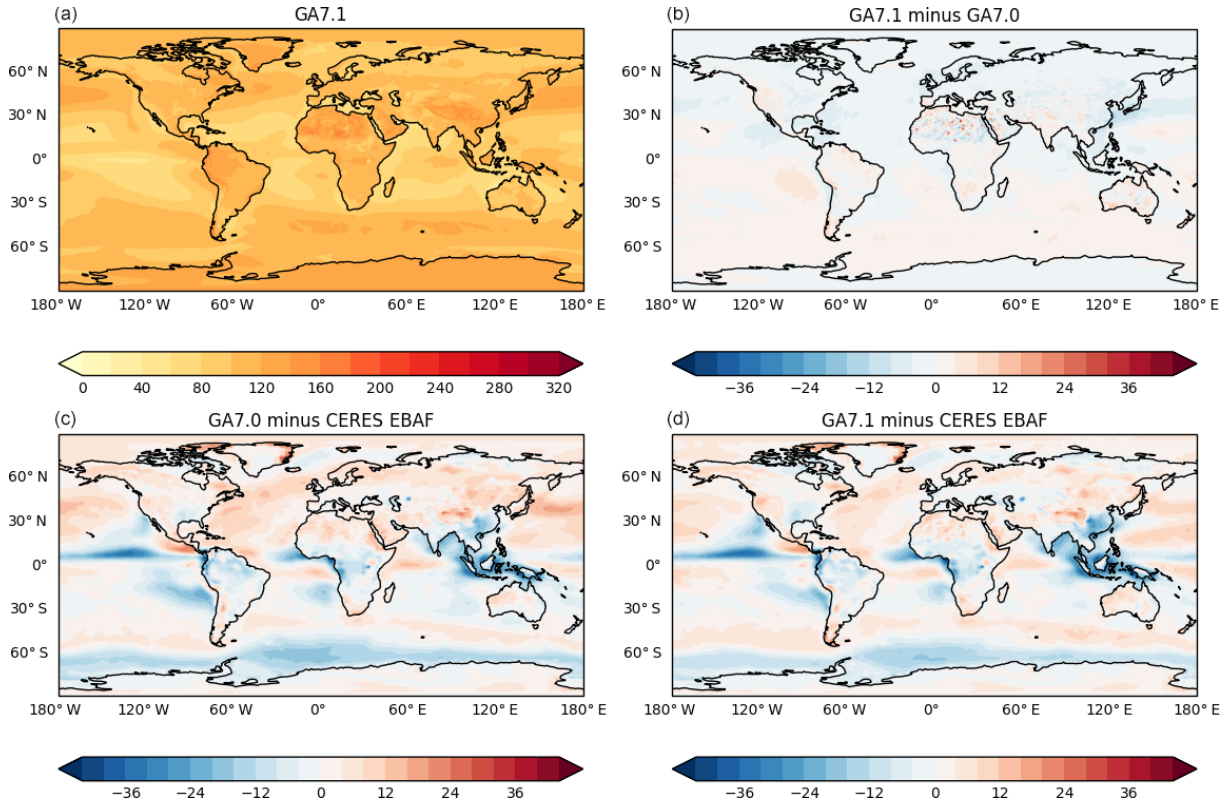

Figure 25. Annual mean top-of-atmosphere reflected SW radiation ($W\,m^{-2}$) in a pair of 20-year N216 atmosphere/land-only climate simulations using GA7.0 and GA7.1. The panels show GA7.1 **(a)**, the difference from GA7.0 **(b)** and the bias compared to CERES-EBAF observations in GA7.0 **(c)** and GA7.1 **(d)**.

Table 9. Identifiers for a set of GA7.0/GL7.0 reference simulations across a number of UM code versions and systems and applications. These suites are held on the Met Office Science Repository Service, which also holds the UM and JULES code. Identifiers marked in bold denote those used in the original assessment of the GA7.0 configuration. Note that in addition to these coupled UM–JULES simulations, a stand-alone reference JULES-GL7 simulation is available in suite u-bb316.

UM code base	Atmosphere/land-only climate			Coupled climate			Seasonal forecast	NWP case study suite				
	N96	N216	N512	N96	N216	N512	N216	N216	N320	N512	N768	N1280
vn10.3	**u-ab642** u-ab747	**u-ab680** u-ab770	u-ab261	**u-ab673**	**u-ab674**			**u-ac441**	**u-ac231**	**u-ac443**	**u-ac445**	**u-ad613**
vn10.4	u-ac283	u-ad442		u-ac349	u-ac695	u-ac699	**mi-an938**		u-ac493			
vn10.5	u-ae523	u-ae955		u-af082	u-af206				u-ae530			
vn10.6	u-ah389	u-ai936		u-ah815					u-ah414			
vn10.7	u-ak497								u-ak926			

4. Multiplicative scaling of the parametrised marine emission of dimethlysulfide (DMS) was included in GLOMAP-mode by $(1 + 0.7)$, where the factor 0.7 is designed to account for a missing source of primary marine organic aerosol in GLOMAP-mode.

5. Several improvements were made to the calculation of the TKE data passed to UKCA-Activate: (i) an explicit bug in the level indexing was corrected, (ii) the minimum value of TKE used was reduced by an order of magnitude following Boutle et al. (2018) and (iii) an explicit estimate of TKE in cumulus cloud was introduced.

6. Replacement of the climatological oceanic DMS concentration of Kettle et al. (1999) with the updated climatology of Lana et al. (2011).

7. Retuning of the parameters mp_dz_scal and cca_sh_knob in Table 7 back to their originally proposed values of 2.0 and 0.5 respectively.

Table 10. Identifiers for a set of GA7.1/GL7.0 reference climate simulations across a number of UM code versions. These suites are held on the Met Office Science Repository Service, which also holds the UM and JULES code. Here, ORCA0.25 denotes a $0.25° \times 0.25°$ NEMO ocean model resolution.

UM code base	Atmosphere/land-only climate		Coupled climate (ORCA0.25)	(ORCA0.25)
	N96	N216	N96	N216
vn10.6	u-ai955		u-ah981	u-ah984
vn10.7	u-al613	u-al616	u-ak896	u-al016

Of the changes listed above, 1, 2, 3, 5 and 6 are model developments that we aim to include in a future release of the GA trunk, whilst 4 and 7 are tunings that may or may not be revisited in the future. The development of GA7.1, including the scientific justification for these differences from GA7.0, is documented in more detail in Mulcahy et al. (2018).

Figure 25 compares the annual mean reflected SW from an N216-resolution present-day climate simulation using GA7.1, with an equivalent simulation using GA7.0. This shows that whilst the changes above reduce the aerosol ERF, the impact on the model's present-day climatology is small, particularly when compared with the impact of GA7.0 in Fig. 15. Where there are differences, these are generally beneficial, and in particular, the reduced contrast between cloud brightness in polluted and pristine air mass reduces the asymmetry in the reflected SW biases discussed in Sect. 4.1.

6 Conclusions

The Global Atmosphere 7.0 and Global Land 7.0 configurations consolidate a number of important incremental improvements to the UM and JULES into the GA and GL trunks, including an improved treatment of gaseous absorption in the radiation scheme, improvements to the treatment of warm rain and ice cloud, and an improvement to the numerics in the model's convection scheme. It also includes additional changes motivated by their impact on the model's largest errors as well as significant structural improvements that increase the complexity and improve the fidelity of climate simulations, namely the UKCA GLOMAP-mode aerosol scheme and the JULES multi-layer snow scheme. An assessment of GA7.0/GL7.0 (and separately of the GC3.0 coupled model configuration that uses it; Williams et al., 2018) shows that the new configurations significantly reduces the four "critical" errors identified in their precursors. Specifically, we see the following:

- a reduction in the climatological dry precipitation bias over the Indian subcontinent,
- a reduction in the tropical tropopause layer warm bias in climate simulations at the N96 horizontal resolution that will be used in UKESM1 and in NWP simulations at all resolutions,
- the removal of a source of energy non-conservation, reducing the size of the global energy correction term required in higher-resolution climate simulations, and
- a significant reduction in the warm SST bias in the Southern Ocean in coupled model simulations.

An initial assessment of the configuration on NWP timescales highlights a number of benefits, although there will need to be an upgrade to the data assimilation system's climatological background error covariances before a configuration based on GA7.0/GL7.0 can be implemented operationally. Finally, an estimate of the model's effective radiative forcing highlighted that the contribution due to anthropogenic aerosols was too strongly negative, which has been addressed by a small number of changes in the GA7.1 branch configuration, most of which are suitable for future inclusion in the GA trunk. This will allow GA7.1 and GL7.0 to be used as the physical atmosphere and land components in the HadGEM3–GC3.1 and UKESM1 climate models that will be submitted to CMIP6.

Code availability. Due to intellectual property rights restrictions, we cannot provide either the source code or documentation papers for the UM or JULES.

Obtaining the UM. The Met Office Unified Model is available for use under licence. A number of research organisations and national meteorological services use the UM in collaboration with the Met Office to undertake basic atmospheric process research, produce forecasts, develop the UM code, and build and evaluate Earth system models. For further information on how to apply for a licence, see http://www.metoffice.gov.uk/research/modelling-systems/unified-model (last access: 4 April 2019).

Obtaining JULES. JULES is available under licence, free of charge. For further information on how to gain permission to use JULES for research purposes see http://jules-lsm.github.io/access_req/JULES_access.html (last access: 4 April 2019).

Details of the simulations performed. UM and JULES simulations are compiled and run in suites developed using the Rose suite engine (http://metomi.github.io/rose/doc/rose.html, last access: 4 April 2019) and scheduled using the Cylc workflow engine (https://cylc.github.io/cylc/, last access: 4 April 2019). Both Rose and Cylc are available under version 3 of the GNU General Public License (GPL). In this framework, the suite contains the information required to extract and build the code as well as configure and run the simulations. Each suite is labelled with a unique identifier and is held in the same revision-controlled repository service in which we hold and develop the model's code. This means that these suites are available to any licensed user of both the UM and JULES. We also document a more complete set of reference GA7- and GL7-based simulations in Tables 9 and 10.

Appendix A: Description of data sets used in Fig. 8

The observations of N50 presented in Fig. 8 are collated from 19 observational campaigns and supplemented by additional ground station observations. The campaign data are derived from size distribution measurements taken during the following campaigns: ACE1 (Bates et al., 1998; Clarke et al., 1998), VOCALS (Hawkins et al., 2010; Wood et al., 2011; Allen et al., 2011), DOE ARM MAGIC (Lewis and Teixeira, 2015), CalNex (Ryerson et al., 2013), WACS (Quinn et al., 2014), NEAQS-2002 (Bates et al., 2005; Quinn and Bates, 2005), ARCTAS (McNaughton et al., 2011), ASCOS (Chang et al., 2011), ICEALOT (Frossard et al., 2011), AEROSOL99 (Bates et al., 2001), DYNAMO (DeWitt et al., 2013), INDOEX (Ramanathan et al., 2001; Quinn and Bates, 2005), PEM-Tropics-A (Fenn et al., 1999), PEM-Tropics-B (Raper et al., 2001), PASE (Hudson and Noble, 2009), NAURU99 (Long and McFarlane, 2012), ACE-ASIA (Huebert et al., 2003; Bates et al., 2004), NEAQS-2004 (Wang et al., 2007; Quinn et al., 2006) and TEXAQS06 (Bates et al., 2008). The ground station observations used are from Canada (Leaitch et al., 2013; Takahama et al., 2011; Jeong et al., 2010), South Africa (Vakkari et al., 2013), the Russian Arctic (Asmi et al., 2016), India (Hyvärinen et al., 2010), Antarctica (Fiebig et al., 2009) and European sites (Asmi et al., 2011). Campaign data were collated via the Global Aerosol Synthesis and Science Project (see reference for GASSP, 2017; Reddington et al., 2017). Ground station observations were collated via GASSP and public data on the EBAS database (see references for details; EBAS, 2019).

The EBAS database has largely been funded by the UNECE CLRTAP (EMEP) and AMAP and through NILU internal resources. Specific developments have been possible due to projects like EUSAAR (EU-FP5; EBAS web interface), EBAS Online (Norwegian Research Council INFRA; upgrading the database platform) and HTAP (European Commission DG-ENV; import and export routines to build a secondary repository in support of http://www.htap.org, last access: 4 April 2019). A large number of specific projects have supported development of data and meta data reporting schemes in dialog with data providers (EU; CREATE, ACTRIS and others). For a complete list of programmes and projects for which EBAS serves as a database, please consult the information box in the Framework filter of the web interface. These are all highly acknowledged for their support.

Supplement. The supplement related to this article is available online at: https://doi.org/10.5194/gmd-12-1909-2019-supplement.

Author contributions. DW led the development of the GA7/GL7 configurations and collated and edited the paper. Authors AJB–MW contributed to the development of the configurations and contributed significant text and/or figures. Authors JB–MZ made significant contributions to either the development or the assessment of the configurations presented in the paper.

Competing interests. The authors declare that they have no conflict of interest.

Acknowledgements. Mohit Dalvi, Nicola Gedney, Steven Hardiman, Andy Jones, Ben Johnson, Colin Johnson, Jane Mulcahy, Alistair Sellar and Rachel Stratton were supported by the Joint BEIS and Defra Met Office Hadley Centre Climate Programme (GA01101). Masashi Ujiie was a visiting scientist working at the Met Office on secondment from the Japan Meteorological Agency under agreement number P014013. The observational data used in Fig. 8 are described in Appendix A; we thank all of the researchers who collected and contributed these and other data used in the assessment of GA7/GL7.

The development and assessment of the Global Atmosphere/Global Land configurations are possible only through the hard work of a large number of people, both within and outside the Met Office, that exceeds the list of authors.

Review statement. This paper was edited by Richard Neale and reviewed by Peter Caldwell and one anonymous referee.

References

Abdul-Razzak, H. and Ghan, S. J.: A parameterization of aerosol activation: 2. Multiple aerosol types, J. Geophys. Res., 105, 6837–6844, https://doi.org/10.1029/1999JD901161, 2000.

Abel, S. J. and Boutle, I. A.: An improved representation of the raindrop size distribution for single-moment microphysics schemes, Q. J. Roy. Meteorol. Soc., 138, 2151–2162, https://doi.org/10.1002/qj.1949, 2012.

Abel, S. J. and Shipway, B. J.: A comparison of cloud-resolving model simulations of trade wind cumulus with aircraft observations taken during RICO, Q. J. Roy. Meteorol. Soc., 133, 781–794, https://doi.org/10.1002/qj.55, 2007.

Adler, R. F., Huffman, G. J., Chang, A., Ferraro, R., Xie, P.-P., Janowiak, J., Rudolf, B., Schneider, U., Curtis, S., Bolvin, D., Gruber, A., Susskind, J., Arkin, P., and Nelkin, E.: The version-2 Global Precipitation Climatology Project (GPCP) monthly precipitation analysis (1979–present), J. Hydrometeor., 4, 1147–1167, https://doi.org/10.1175/1525-7541(2003)004<1147:TVGPCP>2.0.CO;2, 2003.

Allan, R. and Ansell, T.: A new globally complete monthly historical gridded mean sea level pressure dataset (HadSLP2): 1850–2004, J. Climate, 19, 5816–5842, https://doi.org/10.1175/JCLI3937.1, 2006.

Allen, G., Coe, H., Clarke, A., Bretherton, C., Wood, R., Abel, S. J., Barrett, P., Brown, P., George, R., Freitag, S., McNaughton, C., Howell, S., Shank, L., Kapustin, V., Brekhovskikh, V., Kleinman, L., Lee, Y.-N., Springston, S., Toniazzo, T., Krejci, R., Fochesatto, J., Shaw, G., Krecl, P., Brooks, B., McMeeking, G., Bower, K. N., Williams, P. I., Crosier, J., Crawford, I., Connolly, P., Allan, J. D., Covert, D., Bandy, A. R., Russell, L. M., Trembath, J., Bart, M., McQuaid, J. B., Wang, J., and Chand, D.: South East Pacific atmospheric composition and variability sampled along 20° S during VOCALS-REx, Atmos. Chem. Phys., 11, 5237–5262, https://doi.org/10.5194/acp-11-5237-2011, 2011.

Amundsen, D. S., Tremblin, P., Manners, J., Baraffe, I., and Mayne, N. J.: Treatment of overlapping gaseous absorption with the correlated-*k* method in hot Jupiter and brown dwarf atmosphere models, Astron. Astrophys., 598, A97, https://doi.org/10.1051/0004-6361/201629322, 2017.

Anderson, E. A.: A point energy and mass balance model of a snow cover, Tech. Rep. NWQ 19, NOAA, Office of Hydrology, National Weather Service, Silver Spring, MD, USA, available at: https://repository.library.noaa.gov/view/noaa/6392 (last access: 4 April 2019), 1976.

Andres, R. J. and Kasgnoc, A. D.: A time-averaged inventory of subaerial volcanic sulfur emissions, J. Geophys. Res., 103, 25251–25261, https://doi.org/10.1029/98JD02091, 1998.

Arakawa, A. and Lamb, V. R.: Computational design of the basic dynamic processes of the UCLA general circulation model, Methods Comput. Phys., 17, 173–265, 1977.

Asmi, A., Wiedensohler, A., Laj, P., Fjaeraa, A.-M., Sellegri, K., Birmili, W., Weingartner, E., Baltensperger, U., Zdimal, V., Zikova, N., Putaud, J.-P., Marinoni, A., Tunved, P., Hansson, H.-C., Fiebig, M., Kivekäs, N., Lihavainen, H., Asmi, E., Ulevicius, V., Aalto, P. P., Swietlicki, E., Kristensson, A., Mihalopoulos, N., Kalivitis, N., Kalapov, I., Kiss, G., de Leeuw, G., Henzing, B., Harrison, R. M., Beddows, D., O'Dowd, C., Jennings, S. G., Flentje, H., Weinhold, K., Meinhardt, F., Ries, L., and Kulmala, M.: Number size distributions and seasonality of submicron particles in Europe 2008–2009, Atmos. Chem. Phys., 11, 5505–5538, https://doi.org/10.5194/acp-11-5505-2011, 2011.

Asmi, E., Kondratyev, V., Brus, D., Laurila, T., Lihavainen, H., Backman, J., Vakkari, V., Aurela, M., Hatakka, J., Viisanen, Y., Uttal, T., Ivakhov, V., and Makshtas, A.: Aerosol size distribution seasonal characteristics measured in Tiksi, Russian Arctic, Atmos. Chem. Phys., 16, 1271–1287, https://doi.org/10.5194/acp-16-1271-2016, 2016.

Bain, C. L., Williams, K. D., Milton, S. F., and Heming, J. T.: Objective tracking of African Easterly Waves in Met Office models, Q. J. Roy. Meteorol. Soc., 140, 47–57, https://doi.org/10.1002/qj.2110, 2013.

Baran, A. J. and Labonnote, L.-C.: A self-consistent scattering model for cirrus. I: the solar region, Q. J. Roy. Meteorol. Soc., 133, 1899–1912, https://doi.org/10.1002/qj.164, 2007.

Baran, A. J., Hill, P., Furtado, K., Field, P., and Manners, J.: A coupled cloud physics-radiation parameterization of the bulk optical properties of cirrus and its impact on the Met Office Unified Model Global Atmosphere 5.0 configuration, J. Climate, 27, 7725–7752, https://doi.org/10.1175/JCLI-D-13-00700.1, 2014.

Baran, A. J., Hill, P., Walters, D., Hardman, S. C., Furtado, K., Field, P. R., and Manners, J.: The impact of two coupled cirrus microphysics-radiation parameterizations on the temperature and specific humidity biases in the tropical tropopause layer in a climate model, J. Climate, 29, 5299–5316, https://doi.org/10.1175/JCLI-D-15-0821.1, 2016.

Barker, H. and Li, Z.: Improved simulation of clear-sky radiative transfer in the CCC-GCM, J. Climate, 8, 2213–2223, https://doi.org/10.1175/1520-0442(1995)008<2213:ISOCSS>2.0.CO;2, 1995.

Bates, T. S., Huebert, B. J., Gras, J. L., Griffiths, F. B., and Durkee, P. A.: title = International Global Atmospheric Chemistry (IGAC), project's first, Aerosol Characterization Experiment (ACE 1): overview, J. Geophys. Res.-Atmos., 103, 16297–16318, https://doi.org/10.1029/97JD03741, 1998.

Bates, T. S., Quinn, P. K., Coffman, D. J., Johnson, J. E., Miller, T. L., Covert, D. S., Wiedensohler, A., Leinert, S., Nowak, A., and Neusüss, C.: Regional physical and chemical properties of the marine boundary layer aerosol across the Atlantic during Aerosols99: An overview, J. Geophys. Res.-Atmos., 106, 20767–20782, https://doi.org/10.1029/2000JD900578, 2001.

Bates, T. S., Quinn, P. K., Coffman, D. J., Covert, D. S., Miller, T. L., Johnson, J. E., Carmichael, G. R., Guazzotti, S. A., Sodeman, D. A., Prather, K. A., Rivera, M., Russell, L. M., and and Merrill, J. T.: Marine boundary layer dust and pollution transport associated with the passage of a frontal system over eastern Asia, J. Geophys. Res., 109, D19S19, https://doi.org/10.1029/2003JD004094, 2004.

Bates, T. S., Quinn, P. K., Coffman, D. J., Johnson, J. E., and Middlebrook, A. M.: The Dominance of Organic Aerosols in the Marine Boundary Layer over the Gulf of Maine during NEAQS 2002 and their Role in Aerosol Light Scattering, J. Geophys. Res., 110, D18202, https://doi.org/10.1029/2005JD005797, 2005.

Bates, T. S., Quinn, P. K., Coffman, D., Schulz, K., Covert, D. S., Johnson, J. E., Williams, E. J., Lerner, B. M., Angevine, W. M., Tucker, S. C., Brewer, W. A., and Stohl, A.: Boundary layer aerosol chemistry during TexAQS/GoMACCS 2006: Insights into aerosol sources and transformation processes, J. Geophys. Res.-Atmos., 113, D7, https://doi.org/10.1029/2008JD010023, 2008.

Batjes, N. H.: Harmonized soil profile data for applications at global and continental scales: updates to the WISE database, Soil Use Manage., 25, 124–127, https://doi.org/10.1111/j.1475-2743.2009.00202.x, 2009.

Bazile, E., Couvreux, F., Le Moigne, P., Genthon, C., Traullé, O., Maurel, W., Barral, H., Canut, G., Holtslag(4), A. A. M., and Svensson, G.: available at: http://www.umr-cnrm.fr/aladin/meshtml/GABLS4/GABLS4.html (last access: 25 October 2017), 2014.

Beare, R. J.: The role of shear in the morning transition boundary layer, Bound.-Lay. Meteorol., 129, 395–410, https://doi.org/10.1007/s10546-008-9324-8, 2008.

Beljaars, A. C. M. and Holtslag, A. A. M.: Flux parametrization over land surfaces for atmospheric models, J. Appl. Meteorol., 30, 327–341, https://doi.org/10.1175/1520-0450(1991)030<0327:FPOLSF>2.0.CO;2, 1991.

Bellouin, N., Rae, J., Jones, A., Johnson, C., Haywood, J., and Boucher, O.: Aerosol forcing in the Climate Model Intercomparison Project (CMIP5) simulations by HadGEM2-ES and the role of ammonium nitrate, J. Geophys. Res., 116, D20206, https://doi.org/10.1029/2011JD016074, 2011.

Bellouin, N., Mann, G. W., Woodhouse, M. T., Johnson, C., Carslaw, K. S., and Dalvi, M.: Impact of the modal aerosol scheme GLOMAP-mode on aerosol forcing in the Hadley Centre Global Environmental Model, Atmos. Chem. Phys., 13, 3027–3044, https://doi.org/10.5194/acp-13-3027-2013, 2013.

Bengtsson, L. and Körich, H.: Impact of a stochastic parametrization of cumulus convection, using cellular automata, in a mesoscale ensemble prediction system, Q. J. Roy. Meteorol. Soc., 142, 1150–1159, https://doi.org/10.1002/qj.2720, 2016.

Bengtsson, L., Steinheimer, M., Bechtold, P., and Geleyn, J. F.: A stochastic parametrization for deep convection using cellular automata, Q. J. Roy. Meteorol. Soc., 139, 1533–1543, https://doi.org/10.1002/qj.2108, 2013.

Berner, J., Jung, T., and Palmer, T. N.: Systematic error model error: the impact of increased horizontal resolution versus improved stochastic and deterministic parameterizations, J. Climate, 66, 603–626, https://doi.org/10.1175/JCLI-D-11-00297.1, 2012.

Berrisford, P., Dee, D., Fielding, K., Fuentes, M., Kållberg, P., Kobayashi, S., and Uppala, S.: The ERA-Interim archive, Tech. Rep. 1, ERA report series, ECMWF, Reading, UK, 2009.

Best, M. J.: Representing urban areas within operational numerical weather prediction models, Bound.-Lay. Meteorol., 114, 91–109, https://doi.org/10.1007/s10546-004-4834-5, 2005.

Best, M. J., Pryor, M., Clark, D. B., Rooney, G. G., Essery, R. L. H., Ménard, C. B., Edwards, J. M., Hendry, M. A., Gedney, N., Mercado, L. M., Sitch, S., Blyth, E., Boucher, O., Cox, P. M., Grimmond, C. S. B., and Harding, R. J.: The Joint UK Land Environment Simulator (JULES), model description – Part 1: Energy and water fluxes, Geosci. Model Dev., 4, 677–699, https://doi.org/10.5194/gmd-4-677-2011, 2011.

Beven, K. J. and Kirkby, M. J.: A physically based, variable contributing area model of basin hydrology, Hydrol. Sci. Bull., 24, 43–69, https://doi.org/10.1080/02626667909491834, 1979.

Birch, C. E., Roberts, M. J., Garcia-Carreras, L., Ackerley, D., Reeder, M. J., Lock, A. P., and Schiemann, R.: Sea-breeze dynamics and convection initiation: The influence of convective parameterization in weather and climate model biases, J. Climate, 28, 8093–8108, https://doi.org/10.1175/JCLI-D-14-00850.1, 2015.

Bodas-Salcedo, A., Webb, M. J., Brooks, M. E., Ringer, M. A., Williams, K. D., Milton, S. F., and Wilson, D. R.: Evaluating cloud systems in the Met Office global forecast model using simulated CloudSat radar reflectivities, J. Geophys. Res., 113, D00A13, https://doi.org/10.1029/2007JD009620, 2008.

Bodas-Salcedo, A., Williams, K. D., Field, P. R., and Lock, A. P.: The surface downwelling solar radiation surplus over the Southern Ocean in the Met Office model: the role of midlatitude cyclone clouds, J. Climate, 25, 7467–7486, https://doi.org/10.1175/JCLI-D-11-00702.1, 2012.

Bodas-Salcedo, A., Williams, K. D., Ringer, M. A., Beau, I., Cole, J. N. S., Dufresne, J.-L., Koshiro, T., Stevens, B., Wang, Z., and Yokohata, T.: Origins of the solar radiation biases over the Southern Ocean in CFMIP2 models, J. Climate, 27, 41–56, https://doi.org/10.1175/JCLI-D-13-00169.1, 2014.

Bond, T. C. and Bergstrom, R. W.: Light Absorption by Carbonaceous Particles: An Investigative Review, Aerosol Sci. Technol., 40, 27–67, https://doi.org/10.1080/02786820500421521, 2006.

Bond, T. C., Doherty, S. J., Fahey, D. W., Forster, P. M., Berntsen, T., DeAngelo, B. J., Flanner, M. G., Ghan, S., Kärcher, B., Koch, D., Kinne, S., Kondo, Y., Quinn, P. K., Sarofim, M. C., Schultz, M. G., Schulz, M., Venkataraman, C., Zhang, H., Zhang, S., Bellouin, N., Guttikunda, S. K., Hopke, P. K., Jacobson, M. Z., Kaiser, J. W., Klimont, Z., Lohmann, U., Schwarz, J. P., Shindell, D., Storelvmo, T., Warren, S. G., and Zender, C. S.: Bounding the role of black carbon in the climate system: A scientific assessment, J. Geophys. Res.-Atmos., 11, 5380–5552, https://doi.org/10.1002/jgrd.50171, 2013.

Bosilovich, M. G.: NASA's modern era retrospective-analysis for research and applications: Integrating Earth observations, Earthzine, available at: https://earthzine.org/nasas-modern-era-retrospective-analysis/ (last access: 4 April 2019), 2008.

Boutle, I., Price, J., Kudzotsa, I., Kokkola, H., and Romakkaniemi, S.: Aerosol-fog interaction and the transition to well-mixed radiation fog, Atmos. Chem. Phys., 18, 7827–7840, https://doi.org/10.5194/acp-18-7827-2018, 2018.

Boutle, I. A. and Abel, S. J.: Microphysical controls on the stratocumulus topped boundary-layer structure during VOCALS-REx, Atmos. Chem. Phys., 12, 2849–2863, https://doi.org/10.5194/acp-12-2849-2012, 2012.

Boutle, I. A., Abel, S. J., Hill, P. G., and Morcrette, C. J.: Spatial variability of liquid cloud and rain: observations and microphysical effects, Q. J. Roy. Meteorol. Soc., 140, 583–594, https://doi.org/10.1002/qj.2140, 2014a.

Boutle, I. A., Eyre, J. E. J., and Lock, A. P.: Seamless stratocumulus simulation across the turbulent gray zone, Mon. Weather Rev., 142, 1655–1668, https://doi.org/10.1175/MWR-D-13-00229.1, 2014b.

Bowler, N. E., Arribas, A., Mylne, K. R., Robertson, K. B., and Beare, S. E.: The MOGREPS short-range ensemble prediction system, Q. J. Roy. Meteorol. Soc., 134, 703–722, https://doi.org/10.1002/qj.234, 2008.

Bowler, N. E., Arribas, A., Beare, S. E., and Mylne, K. R.: The local ETKF and SKEB: upgrades to the MOGREPS short-range ensemble prediction system, Q. J. Roy. Meteorol. Soc., 135, 767–776, https://doi.org/10.1002/qj.394, 2009.

Bowler, N. E., Clayton, A. M., Jardak, M., Lee, E., Lorenc, A. C., Piccolo, C., Pring, S. R., Wlasak, M. A., Barker, D. M., Inverarity, G. W., and Swinbank, R.: Inflation and localization tests in the development of an ensemble of 4D-ensemble variational assimilations, Q. J. Roy. Meteorol. Soc., 143, 1280–1302, https://doi.org/10.1002/qj.3004, 2017.

Brohan, P., Kennedy, J. J., Harris, I., Tett, S. F. B., and Jones, P. D.: Uncertainty estimates in regional and global observed temperature changes: a new dataset from 1850, J. Geophys. Res., 111, D12106, https://doi.org/10.1029/2005JD006548, 2006.

Brown, A., Milton, S., Cullen, M., Golding, B., Mitchell, J., and Shelly, A.: Unified modeling and prediction of weather and climate: a 25 year journey, B. Am. Meteorol. Soc., 93, 1865–1877, https://doi.org/10.1175/BAMS-D-12-00018.1, 2012.

Brown, A. R.: The sensitivity of large-eddy simulations of shallow cumulus convection to resolution and subgrid model, Q. J. Roy. Meteorol. Soc., 125, 469–482, https://doi.org/10.1002/qj.49712555405, 1999.

Brown, A. R., Beare, R. J., Edwards, J. M., Lock, A. P., Keogh, S. J., Milton, S. F., and Walters, D. N.: Upgrades to the boundary-layer scheme in the Met Office numerical weather prediction model, Bound.-Lay. Meteorol., 128, 117–132, https://doi.org/10.1007/s10546-008-9275-0, 2008.

Burke, E. J., Dankers, R., Jones, C. D., and Wiltshire, A. J.: A retrospective analysis of pan Arctic permafrost using the JULES land surface model, Clim. Dynam., 41, 1025–1038, https://doi.org/10.1007/s00382-012-1648-x, 2013.

Bushell, A. C., Wilson, D. R., and Gregory, D.: A description of cloud production by non-uniformly distributed processes, Q. J. Roy. Meteorol. Soc., 129, 1435–1455, https://doi.org/10.1256/qj.01.110, 2003.

Calonne, N., Flin, F., Morin, S., Lesaffre, B., Rolland du Roscoat, S., and Geindreau, C.: Numerical and experimental investigations of the effective thermal conductivity of snow, Geophys. Res. Lett., 38, L23501, https://doi.org/10.1029/2011GL049234, 2011.

Chang, R. Y.-W., Leck, C., Graus, M., Müller, M., Paatero, J., Burkhart, J. F., Stohl, A., Orr, L. H., Hayden, K., Li, S.-M., Hansel, A., Tjernström, M., Leaitch, W. R., and Abbatt, J. P. D.: Aerosol composition and sources in the central Arctic Ocean during ASCOS, Atmos. Chem. Phys., 11, 10619–10636, https://doi.org/10.5194/acp-11-10619-2011, 2011.

Charney, J. G. and Phillips, N. A.: Numerical integration of the quasi-geostrophic equations for barotropic and simple baroclinic flows, J. Meteorol., 10, 71–99, https://doi.org/10.1175/1520-0469(1953)010<0071:NIOTQG>2.0.CO;2, 1953.

Charnock, H.: Wind stress on a water surface, Q. J. Roy. Meteorol. Soc., 81, 639–640, https://doi.org/10.1002/qj.49708135027, 1955.

Cionni, I., Eyring, V., Lamarque, J. F., Randel, W. J., Stevenson, D. S., Wu, F., Bodeker, G. E., Shepherd, T. G., Shindell, D. T., and Waugh, D. W.: Ozone database in support of CMIP5 simulations: results and corresponding radiative forcing, Atmos. Chem. Phys., 11, 11267–11292, https://doi.org/10.5194/acp-11-11267-2011, 2011.

Clarke, A. D., Varner, J. L., Eisele, F., Mauldin, R. L., Tanner, D., and Litchy, M.: Particle production in the remote marine atmosphere: Cloud outflow and subsidence during ACE 1, J. Geophys. Res.-Atmos., 103, 16397–16409, https://doi.org/10.1029/97JD02987, = 1998.

Clark, D. B., Mercado, L. M., Sitch, S., Jones, C. D., Gedney, N., Best, M. J., Pryor, M., Rooney, G. G., Essery, R. L. H., Blyth, E., Boucher, O., Cox, P. M., and Harding, R. J.: The Joint UK Land Environment Simulator (JULES), model description – Part 2: Carbon fluxes and vegetation, Geosci. Model Dev., 4, 701–722, https://doi.org/10.5194/gmd-4-701-2011, 2011.

Clayton, A. M., Lorenc, A. C., and Barker, D. M.: Operational implementation of a hybrid ensemble/4D-Var global data assimilation system at the Met Office, Q. J. Roy. Meteorol. Soc., 139, 1445–1461, https://doi.org/10.1002/qj.2054, 2013.

Cotton, R. J., Field, P. R., Ulanowski, Z., Kaye, P. H., Hirst, E., Greenaway, R. S., Crawford, I., Crosier, J., and Dorsey, J.: The effective density of small ice particles obtained from in situ aircraft observations of mid-latitude cirrus, Q. J. Roy. Meteorol. Soc., 139, 1923–1934, https://doi.org/10.1002/qj.2058, 2013.

Cox, C. and Munk, W.: Measurement of the Roughness of the Sea Surface from Photographs of the Sun's Glitter, J. Opt. Soc. Am., 44, 838–850, https://doi.org/10.1364/JOSA.44.000838, 1954.

Cusack, S., Slingo, A., Edwards, J. M., and Wild, M.: The radiative impact of a simple aerosol climatology on the Hadley Centre atmospheric GCM, Q. J. Roy. Meteorol. Soc., 124, 2517–2526, https://doi.org/10.1002/qj.49712455117, 1998.

Daumont, D., Brion, J., Charbonnier, J., and Malicet, J.: Ozone UV spectroscopy I: Absorption cross-sections at room temperature, J. Atmos. Chem., 15, 145–155, https://doi.org/10.1007/BF00053756, 1992.

Dawson, A. and Palmer, T. N.: Simulating weather regimes: impact of model resolution and stochastic parameterization, Clim. Dynam., 44, 2177–2193, https://doi.org/10.1007/s00382-014-2238-x, 2015.

Derbyshire, S. H., Maidens, A. V., Milton, S. F., Stratton, R. A., and Willett, M. R.: Adaptive detrainment in a convective parametrization, Q. J. Roy. Meteorol. Soc., 137, 1856–1871, https://doi.org/10.1002/qj.875, 2011.

DeWitt, H. L., Coffman, D. J., Schulz, K. J., Alan Brewer, W., Bates, T. S., and Quinn, P. K.: Atmospheric aerosol properties over the equatorial Indian Ocean and the impact of the Madden–Julian Oscillation, J. Geophys. Res.-Atmos., 118, 5736–5749, https://doi.org/10.1002/jgrd.50419, 2013.

Dharssi, I., Vidale, P. L., Verhoef, A., Macpherson, B., Jones, C., and Best, M.: New soil physical properties implemented in the Unified Model at PS18, Tech. Rep. 528, Forecasting R&D, Met Office, Exeter, UK, 2009.

Doblas-Reyes, F. J., Weisheimer, A., Déqué, M., Keenlyside, N., McVean, M., Murphy, J. M., Rogel, P., Smith, D., and Palmer, T. N.: Addressing model uncertainty in seasonal and annual dynamical seasonal forecasts, Q. J. Roy. Meteorol. Soc., 135, 1538–1559, https://doi.org/10.1002/qj.464, 2009.

Donelan, M. A., Dobson, F. W., Smith, S. D., and Anderson, R. J.: On the dependence of sea surface roughness on wave development, J. Phys. Oceanogr., 23, 2143–2149, https://doi.org/10.1175/1520-0485(1993)023<2143:OTDOSS>2.0.CO;2, 1993.

Dyer, A. J. and Hicks, B. B.: Flux-gradient relationships in the constant flux layer, Q. J. Roy. Meteorol. Soc., 96, 715–721, https://doi.org/10.1002/qj.49709641012, 1970.

EBAS: http://ebas.nilu.no, last access: 12 March 2019.

Eckermann, S. D.: Explicitly stochastic parameterization of nonorographic gravity wave drag, J. Atmos. Sci., 68, 1749–1765, https://doi.org/10.1175/2011JAS3684.1, 2011.

Edson, J. B.: Review of air-sea transfer processes, in: ECMWF workshop on atmosphere-ocean interactions, Reading, UK, 10–12 November, 2008, 7–24, European Centre for Medium-Range Weather Forecasts, 2009.

Edson, J. B., Jampana, V., Weller, R. A., Biggore, S. P., Plueddemann, A. J., Fairall, C. W., Miller, S. D., Mahrt, L., Vickers, D., and Hersbach, H.: On the exchange of momentum over the open ocean, J. Phys. Oceanogr., 43, 1589–1610, https://doi.org/10.1175/JPO-D-12-0173.1, 2013.

Edwards, J. M.: Efficient calculation of infrared fluxes and cooling rates using the two-stream equations, J. Atmos. Sci., 53, 1921–1932, https://doi.org/10.1175/1520-0469(1996)053<1921:ECOIFA>2.0.CO;2, 1996.

Edwards, J. M. and Slingo, A.: Studies with a flexible new radiation code. I: Choosing a configuration for a large-scale model, Q. J. Roy. Meteorol. Soc., 122, 689–719, https://doi.org/10.1002/qj.49712253107, 1996.

Essery, R., Pomeroy, J., Parviainen, J., and Storck, P.: Sublimation of snow from coniferous forests in a climate model, J. Climate, 16, 1855–1864, https://doi.org/10.1175/1520-0442(2003)016<1855:SOSFCF>2.0.CO;2, 2003a.

Essery, R. L. H., Best, M. J., Betts, R. A., Cox, P. M., and Taylor, C. M.: Explicit representation of subgrid heterogeneity in a GCM land surface scheme, J. Hydrometeor., 4, 530–543, https://doi.org/10.1175/1525-7541(2003)004<0530:EROSHI>2.0.CO;2, 2003b.

Eyring, V., Bony, S., Meehl, G. A., Senior, C., Stevens, B., and Stouffer, R. J. Taylor, K. E.: Overview of the Coupled Model Intercomparison Project Phase 6 (CMIP6) experimental design and organisation, Geosci. Model Dev. Discuss., 8, 10539–10583, https://doi.org/10.5194/gmdd-8-10539-2015, 2015.

Fairall, C. W., Bradley, E. F., Hare, J. E., Grachev, A. A., and Edson, J. B.: Bulk parameterization of air-sea fluxes: updates and verification for the COARE algorithm, J. Climate, 16, 571–591, https://doi.org/10.1175/1520-0442(2003)016<0571:BPOASF>2.0.CO;2, 2003.

Falloon, P. D. and Betts, R. A.: The impact of climate change on global river flow in HadGEM1 simulations, Atmos. Sci. Lett., 7, 62–68, https://doi.org/10.1002/asl.133, 2006.

Fenn, M. A., Browell, E. V., Butler, C. F., Grant, W. B., Kooi, S. A., Clayton, M. B., Gregory, G. L., Newell, R. E., Zhu, Y., Dibb, J. E., Fuelberg, H. E., Anderson, B. E., Bandy, A. R., Blake, D. R., Bradshaw, J. D., Heikes, B. G., Sachse, G. W., Sandholm, S. T., Singh, H. B., Talbot, R. W., and Thornton, D. C.: Ozone and aerosol distributions and air mass characteristics over the South Pacific during the burning season, J. Geophys. Res.-Atmos., 104, 16197–16212, https://doi.org/10.1029/1999JD900065, 1999.

Fiebig, M., Lunder, C. R., and Stohl, A.: Tracing biomass burning aerosol from South America to Troll Research Station, Antarctica, Geophys. Res. Lett., 36, L14815, https://doi.org/10.1029/2009GL038531, 2009.

Field, P. R., Heymsfield, A. J., and Bansemer, A.: Snow Size Distribution Parameterization for Midlatitude and Tropical Ice Clouds, J. Atmos. Sci., 64, 4346–4365, https://doi.org/10.1175/2007JAS2344.1, 2007.

Field, P. R., Hill, A. A., Furtado, K., and Korolev, A.: Mixed-phase clouds in a turbulent environment. Part 2: Analytic treatment, Q. J. Roy. Meteorol. Soc., 140, 870–880, https://doi.org/10.1002/qj.2175, 2014.

Ford, D. A., Edwards, K. P., Lea, D., Barciela, R. M., Martin, M. J., and Demaria, J.: Assimilating GlobColour ocean colour data into a pre-operational physical-biogeochemical model, Ocean Sci., 8, 751–771, https://doi.org/10.5194/os-8-751-2012, 2012.

Fritsch, J. M. and Chappell, C. F.: Numerical prediction of convectively driven mesoscale pressure systems. Part I: convective parameterization, J. Atmos. Sci., 37, 1722–1733, https://doi.org/10.1175/1520-0469(1980)037<1722:NPOCDM>2.0.CO;2, 1980.

Frossard, A. A., Shaw, P. M., Russell, L. M., Kroll, J. H., Canagartna, M., Worsnop, D., Quinn, P. K., and Bates, T. S.: Springtime Arctic haze contributions of submicron organic particles

from European and Asian combustion sources, J. Geophys. Res., 116, D05205, https://doi.org/10.1029/2010JD015178, 2011.

Furtado, K., Field, P. R., Cotton, R., and Baran, A. J.: The sensitivity of simulated high clouds to ice crystal fall speed, shape and size distribution, Q. J. Roy. Meteorol. Soc., 141, 1546–1559, https://doi.org/10.1002/qj.2457, 2015.

Furtado, K., Field, P. R., Boutle, I. A., Morcrette, C. J., and Wilkinson, J. M.: A physically based subgrid parameterization for the production and maintenance of mixed-phase clouds in a general circulation model, J. Atmos. Sci., 73, 279–291, https://doi.org/10.1175/JAS-D-15-0021.1, 2016.

Gallet, J.-C., Domine, F., Arnaud, L., Picard, G., and Savarino, J.: Vertical profile of the specific surface area and density of the snow at Dome C and on a transect to Dumont D'Urville, Antarctica – albedo calculations and comparison to remote sensing products, The Cryosphere, 5, 631–649, https://doi.org/10.5194/tc-5-631-2011, 2011.

Garcia-Carreras, L., J., P. D., Marsham, J. H., Rosenberg, P. D., Brooks, I. M., Lock, A. P., Marenco, F., McQuaid, J. B., and Hobby, M.: The turbulent structure and diurnal growth of the Saharan atmospheric boundary layer, J. Atmos. Sci., 72, 693–713, https://doi.org/10.1175/JAS-D-13-0384.1, 2015.

GASSP: Global Aerosol Synthesis and Science Project, available at: http://gassp.org.uk, last access: 25 October, 2017.

Gedney, N. and Cox, P. M.: The sensitivity of global climate model simulations to the representation of soil moisture heterogeneity, J. Hydrometeor., 4, 1265–1275, https://doi.org/10.1175/1525-7541(2003)004<1265:TSOGCM>2.0.CO;2, 2003.

Godfrey, J. S. and Beljaars, A. C. M.: On the turbulent fluxes of buoyancy, heat and moisture at the air-sea interface at low wind speeds, J. Geophys. Res., 96, 22043–22048, https://doi.org/10.1029/91JC02015, 1991.

Gorshelev, V., Serdyuchenko, A., Weber, M., Chehade, W., and Burrows, J. P.: High spectral resolution ozone absorption cross-sections – Part 1: Measurements, data analysis and comparison with previous measurements around 293 K, Atmos. Meas. Tech., 7, 609–624, https://doi.org/10.5194/amt-7-609-2014, 2014.

Grant, A. L. M.: Cloud-base fluxes in the cumulus-capped boundary layer, Q. J. Roy. Meteorol. Soc., 127, 407–421, https://doi.org/10.1002/qj.49712757209, 2001.

Grant, A. L. M. and Brown, A. R.: A similarity hypothesis for shallow-cumulus transports, Q. J. Roy. Meteorol. Soc., 125, 1913–1936, https://doi.org/10.1002/qj.49712555802, 1999.

Grant, A. L. M. and Lock, A. P.: The turbulent kinetic energy budget for shallow cumulus convection, Q. J. Roy. Meteorol. Soc., 130, 401–422, https://doi.org/10.1256/qj.03.50, 2004.

Gregory, D. and Allen, S.: The effect of convective downdraughts upon NWP and climate simulations, in: Ninth conference on numerical weather prediction, Denver, Colorado, 122–123, 1991.

Gregory, D. and Rowntree, P. R.: A massflux convection scheme with representation of cloud ensemble characteristics and stability dependent closure, Mon. Weather Rev., 118, 1483–1506, https://doi.org/10.1175/1520-0493(1990)118<1483:AMFCSW>2.0.CO;2, 1990.

Gregory, D., Kershaw, R., and Inness, P. M.: Parametrization of momentum transport by convection II: Tests in single-column and general circulation models, Q. J. Roy. Meteorol. Soc., 123, 1153–1183, https://doi.org/10.1002/qj.49712354103, 1997.

Hardiman, S. C., Boutle, I. A., Bushell, A. C., Butchart, N., Cullen, M. J. P., Field, P. R., Furtado, K., Manners, J. C., Milton, S. F., Morcrette, C., O'Connor, F. M., Shipway, B. J., Smith, C., Walters, D. N., Willett, M. R., Williams, K. D., Wood, N., Abraham, N. L., Keeble, J., Maycock, A. C., Thuburn, J., and Woodhouse, M. T.: Processes controlling tropical tropopause temperature and stratospheric water vapor in climate models, J. Climate, 28, 6516–6535, https://doi.org/10.1175/JCLI-D-15-0075.1, 2015.

Hastings, D. A., Dunbar, P. K., Elphingstone, G. M., Bootz, M., Murakami, H., Maruyama, H., Masaharu, H., Holland, P., Payne, J., Bryant, N. A., Logan, T. L., Muller, J.-P., Schreier, G., and MacDonald, J. S.: The Global Land One-kilometer Base Elevation (GLOBE) Digital Elevation Model, Version 1.0, Digital data base on the World Wide Web, available at: http://www.ngdc.noaa.gov/mgg/topo/globe.html (last access: 25 October 2017), 1999.

Hawkins, L. N., Russell, L. M., Covert, D. S., Quinn, P. K., and Bates, T. S.: Carboxylic acids, sulfates, and organosulfates in processed continental organic aerosol over the Southeast Pacific Ocean during VOCALS-REx 2008 J. Geophys. Res., 115, D132012010, https://doi.org/10.1029/2009JD013276, 2010.

Hill, A. A., Field, P. R., Furtado, K., Korolev, A., and Shipway, B. J.: Mixed-phase clouds in a turbulent environment. Part 1: Large-eddy simulation experiments, Q. J. Roy. Meteorol. Soc., 140, 855–869, https://doi.org/10.1002/qj.2177, 2014.

Hill, A. A., Shipway, B. J., and Boutle, I. A.: How sensitive are aerosol-precipitation interactions to the warm rain representation?, J. Adv. Model. Earth Syst., 7, 987–1004, https://doi.org/10.1002/2014MS000422, 2015.

Hill, P. G., Manners, J., and Petch, J. C.: Reducing noise associated with the Monte Carlo Independent Column Approximation for weather forecasting models, Q. J. Roy. Meteorol. Soc., 137, 219–228, https://doi.org/10.1002/qj.732, 2011.

Hill, P. G., Hogan, R. J., Manners, J., and Petch, J. C.: Parametrizing the horizontal inhomogeneity of ice water content using CloudSat data products, Q. J. Roy. Meteorol. Soc., 138, 1784–1793, https://doi.org/10.1002/qj.1893, 2012.

Hill, P. G., Morcrette, C. J., and Boutle, I. A.: A regime-dependent parametrization of subgrid-scale cloud water content variability, Q. J. Roy. Meteorol. Soc., 141, 1975–1986, https://doi.org/10.1002/qj.2506, 2015.

Hogan, R. J. and Illingworth, A. J.: Parameterizing ice cloud inhomogeneity and the overlap of inhomogeneities using cloud radar data, J. Atmos. Sci., 60, 756–767, https://doi.org/10.1175/1520-0469(2003)060<0756:PICIAT>2.0.CO;2, 2003.

Holben, B. N., Tanre, D., Smirnov, A., Eck, T. F., Slutsker, I., Abuhassan, N., Newcomb, W. W., Schafer, J., Chatenet, B., Lavenue, F., Kaufman, Y. J., Castle, J. V., Setzer, A., Markham, B., Clark, D., Frouin, R., Halthore, R., Karnieli, A., O'Neill, N. T., Pietras, C., Pinker, R. T., Voss, K., and Zibordi, G.: An emerging ground-based aerosol climatology: Aerosol Optical Depth from AERONET, J. Geophys. Res., 106, 12067–12097, https://doi.org/10.1029/2001JD900014, 2001.

Holtslag, A. A. M. and Moeng, C.-H.: Eddy diffusivity and countergradient transport in the convective atmospheric boundary layer, J. Atmos. Sci., 48, 1690–1698, https://doi.org/10.1175/1520-0469(1991)048<1690:EDACTI>2.0.CO;2, 1991.

Houldcroft, C., Grey, W., Barnsley, M., Taylor, C., Los, S., and North, P.: New vegetation albedo parameters and global fields of background albedo derived from MODIS for

use in a climate model, J. Hydrometeorol., 10, 183–198, https://doi.org/10.1175/2008JHM1021.1, 2008.

Hourdin, F., Mauritsen, T., Gettelman, A., Golaz, J.-C., Balaji, V., Duan, Q., Folini, D., Ji, D., Klocke, D., Qian, Y., Rauser, F., Rio, C., Tomassini, L., Watanabe, M., and Williamson, D.: The art and science of climate model tuning, B. Am. Meteorol. Soc., 98, 589–602, https://doi.org/10.1175/BAMS-D-15-00135.1, 2017.

Huebert, B. J., Bates, T., Russell, P. B., Shi, G., Kim, Y. J., Kawamura, K., Carmichael, G., and Nakajima, T.: An overview of ACE-Asia: Strategies for quantifying the relationships between Asian aerosols and their climatic impacts, journal = "J Geophys Res Atmos.", volume = 108, pages = D23, doi = 10.1029/2003JD003550, 2003.

Hudson, J. G. and Noble, S.: CCN and cloud droplet concentrations at a remote ocean site, Geophys. Res. Lett., 36, L13812 https://doi.org/10.1029/2009GL038465, 2009.

Hyder, P., Edwards, J. M., Allan, R. P., Hewitt, H. T., Bracegirdle, T. J., Gregory, J. M., Wood, R. A., Meijers, A. J. S., Mulcahy, J., Field, P., Furtado, K., Bodas-Salcedo, A., Williams, K. D., Copsey, D., Josey, S. A., Liu, C., Roberts, C. D., Sanchez, C., Ridley, J., Thorpe, L., Hardiman, S. C., Mayer, M., Berry, D. I., and Belcher, S. E.: Critical Southern Ocean climate model biases traced to atmospheric model cloud errors, Nat. Commun., 9, 3625, https://doi.org/10.1038/s41467-018-05634-2, 2018.

Hyvärinen, A.-P., Lihavainen, H., Komppula, M., Panwar, T. S., Sharma, V. P., Hooda, R. K., and Viisanen, Y.: Aerosol measurements at the Gual Pahari EUCAARI station: preliminary results from in-situ measurements, Atmos. Chem. Phys., 10, 7241–7252, https://doi.org/10.5194/acp-10-7241-2010, 2010.

Illingworth, A. J., Hogan, R. J., O'Connor, E. J., Bouniol, D., Delanoë, J., Pelon, J., Protat, A., Brooks, M. E., Gaussiat, N., Wilson, D. R., Donovan, D. P., Klein Baltink, H., van Zadelhoff, G.-J., Eastment, J. D., Goddard, J. W. F., Wrench, C. L., Haeffelin, M., Krasnov, O. A., Russchenberg, H. W. J., Piriou, J.-M., Vinit, F., Seifert, A., Tompkins, A. M., and U, W.: Cloudnet-continuous evaluation of cloud profiles in seven operational models using ground-based observations, B. Am. Meteorol. Soc., 88, 883–898, https://doi.org/10.1175/BAMS-88-6-883, 2007.

Inverarity, G. W., Wlasak, M. A., Jardak, M., and Lorenc, A. C.: Deterministic data assimilation developments – July 2017, Tech. Rep. 625, Forecasting Research, Met Office, Exeter, UK, 2018.

IPCC: Climate Change 2013: The Physical Science Basis. Contribution of Working Group I to the Fifth Assessment Report of the Intergovernmental Panel on Climate Change, Cambridge University Press, Cambridge, United Kingdom and New York, NY, USA, https://doi.org/10.1017/CBO9781107415324, 2013.

Jeong, C.-H., Evans, G. J., McGuire, M. L., Chang, R. Y.-W., Abbatt, J. P. D., Zeromskiene, K., Mozurkewich, M., Li, S.-M., and Leaitch, W. R.: Particle formation and growth at five rural and urban sites, Atmos. Chem. Phys., 10, 7979–7995, https://doi.org/10.5194/acp-10-7979-2010, 2010.

Jin, Z., Qiao, Y., Wang, Y., Fang, Y., and Yi, W.: A new parameterization of spectral and broadband ocean surface albedo, Opt. Expres, 19, 26429–26443, https://doi.org/10.1364/OE.19.026429, 2011.

Johansen, O.: Thermal conductivity of soils, Ph.D. thesis, University of Trondheim, Norway, 1975.

Kettle, A. J., Andreae, M. O., Amouroux, D., Andreae, T. W., Bates, T. S., Berresheim, H., Bingemer, H., Boniforti, R., Curran, M. A. J., DiTullio, G. R., Helas, G., Jones, G. B., Keller, M. D., Kiene, R. P., Leck, C., Levasseur, M., Malin, G., Maspero, M., Matrai, P., McTaggart, A. R., Mihalopoulos, N., Nguyen, B. C., Novo, A., Putaud, J. P., Rapsomanikis, S., Roberts, G., Schebeske, G., Sharma, S., Simó, R., Staubes, R., Turner, S., and Uher, G.: A global database of sea surface dimethyl sulfide (DMS) measurements and a procedure to predict sea surface DMS as a function of latitude, longitude, and month, Global Biogeochem. Cy., 13, 399–444, https://doi.org/10.1029/1999GB900004, 1999.

Khairoutdinov, M. and Kogan, Y.: A new cloud physics parameterization in a large-eddy simulation model of marine stratocumulus, Mon. Weather Rev., 128, 229–243, https://doi.org/10.1175/1520-0493(2000)128<0229:ANCPPI>2.0.CO;2, 2000.

Klein, S. A., McCoy, R. B., Morrison, H., Ackerman, A. S., Avramov, A., Boer, G. d., Chen, M., Cole, J. N. S., Del Genio, A. D., Falk, M., Foster, M. J., Fridlind, A., Golaz, J.-C., Hashino, T., Harrington, J. Y., Hoose, C., Khairoutdinov, M. F., Larson, V. E., Liu, X., Luo, Y., McFarquhar, G. M., Menon, S., Neggers, R. A. J., Park, S., Poellot, M. R., Schmidt, J. M., Sednev, I., Shipway, B. J., Shupe, M. D., Spangenberg, D. A., Sud, Y. C., Turner, D. D., Veron, D. E., Salzen, K. v., Walker, G. K., Wang, Z., Wolf, A. B., Xie, S., Xu, K.-M., Yang, F., and Zhang, G.: Intercomparison of model simulations of mixed-phase clouds observed during the ARM mixed-phase arctic cloud experiment. I: single-layer cloud, Q. J. Roy. Meteorol. Soc., 135, 979–1002, https://doi.org/10.1002/qj.416, 2009.

Lamarque, J.-F., Bond, T. C., Eyring, V., Granier, C., Heil, A., Klimont, Z., Lee, D., Liousse, C., Mieville, A., Owen, B., Schultz, M. G., Shindell, D., Smith, S. J., Stehfest, E., Van Aardenne, J., Cooper, O. R., Kainuma, M., Mahowald, N., McConnell, J. R., Naik, V., Riahi, K., and van Vuuren, D. P.: Historical (1850–2000) gridded anthropogenic and biomass burning emissions of reactive gases and aerosols: methodology and application, Atmos. Chem. Phys., 10, 7017–7039, https://doi.org/10.5194/acp-10-7017-2010, 2010.

Lana, A., Bell, T. G., Simó, R., Vallina, S. M., Ballabrera-Poy, J., Kettle, A. J., Dachs, J., Bopp, L., Saltzman, E. S., Stefels, J., Johnson, J. E., and Liss, P. S.: An updated climatology of surface dimethlysulfide concentrations and emission fluxes in the global ocean, Global Biogeochem. Cy., 25, GB1004, https://doi.org/10.1029/2010GB003850, 2011.

Leaitch, W. R., Sharma, S., Huang, L., Toom–Sauntry, D., Chivulescu, A., Macdonald, A. M., von Salzen, K., Pierce, J. R., Bertram, A. K., Schroder, J. C., Shantz, N. C., Chang, R. Y.-W., and Norman, A.-L.: Dimethyl sulfide control of the clean summertime Arctic aerosol and cloud, Elem. Sci. Anth., 1, 17, https://doi.org/10.12952/journal.elementa.000017, 2013.

Lean, J., Rottman, G., Harder, J., and Kopp, G.: SORCE Contributions to New Understanding of Global Change and Solar Variability, in: The Solar Radiation and Climate Experiment (SORCE): Mission Description and Early Results, edited by: Rottman, G., Woods, T., and George, V., 27–53, Springer New York, New York, NY, https://doi.org/10.1007/0-387-37625-9_3, 2005.

Legates, D. R. and Willmott, C. J.: Mean seasonal and spatial variability in global surface air temperature, Theor. Appl. Climatol., 41, 11–21, https://doi.org/10.1007/BF00866198, 1990a.

Legates, D. R. and Willmott, C. J.: Mean seasonal and spatial variability in gauge-corrected, global precipitation, Int. J. Climatol., 10, 111–127, https://doi.org/10.1002/joc.3370100202, 1990b.

Lewis, E. R. and Teixeira, J.: Dispelling clouds of uncertainty, Eos, 96, https://doi.org/10.1029/2015EO031303, 2015.

Liu, Y., Daum, P. H., Guo, H., and Peng, Y.: Dispersion bias, dispersion effect, and the aerosol-cloud conundrum, Environ. Res. Lett., 3, 045021, https://doi.org/10.1088/1748-9326/3/4/045021, 2008.

Lock, A. P.: The numerical representation of entrainment in parametrizations of boundary layer turbulent mixing, Mon. Weather Rev., 129, 1148–1163, https://doi.org/10.1175/1520-0493(2001)129<1148:TNROEI>2.0.CO;2, 2001.

Lock, A. P., Brown, A. R., Bush, M. R., Martin, G. M., and Smith, R. N. B.: A new boundary layer mixing scheme. Part I: Scheme description and single-column model tests, Mon. Weather Rev., 128, 3187–3199, https://doi.org/10.1175/1520-0493(2000)128<3187:ANBLMS>2.0.CO;2, 2000.

Loeb, N. G., Wielicki, B. A., Doelling, D. R., Smith, G. L., Keyes, D. F., Kato, S., Manalo-Smith, N., and Wong, T.: Toward optimal closure of the Earth's top-of-atmosphere radiation budget, J. Climate, 22, 748–766, https://doi.org/10.1175/2008JCLI2637.1, 2009.

Long, C. N. and McFarlane, S. A.: Quantification of the Impact of Nauru Island on ARM Measurements, J. Appl. Meteorol. Climatol., 51, 628–636, https://doi.org/10.1175/JAMC-D-11-0174.1, 2012.

Lott, F. and Miller, M. J.: A new subgrid-scale orographic drag parametrization: Its formulation and testing, Q. J. Roy. Meteorol. Soc., 123, 101–127, https://doi.org/10.1002/qj.49712353704, 1997.

Loveland, T. R., Reed, B. C., Brown, J. F., Ohlen, D. O., Zhu, Z., Yang, L., and Merchant, J. W.: Development of a global land cover characteristics database and IGBP DISCover from 1 km AVHRR data, Int. J. Remote Sens., 21, 1303–1330, https://doi.org/10.1080/014311600210191, 2000.

MacKay, M. D. and Bartlett, P. A.: Estimating canopy snow unloading timescales from daily observations of albedo and preciptation, Geophys. Res. Lett., 33, L19405, https://doi.org/10.1029/2006GL027521, 2006.

MacLachlan, C., Arribas, A., Peterson, K. A., Maidens, A., Fereday, D., Scaife, A. A., Gordon, M., Vellinga, M., Williams, A., Comer, R. E., Camp, J., Xavier, P., and Madec, G.: Global Seasonal forecast system version 5 (GloSea5): a high-resolution seasonal forecast system, Q. J. Roy. Meteorol. Soc., 141, https://doi.org/10.1002/qj.2396, 2014.

Madden, R. A. and Julian, P. R.: Detection of a 40–50 day oscillation in the zonal wind in the tropical Pacific, J. Atmos. Sci., 28, 702–708, https://doi.org/10.1175/1520-0469(1971)028<0702:DOADOI>2.0.CO;2, 1971.

Malicet, J., Daumont, D., Charbonnier, J., Parisse, C., Chakir, A., and Brion, J.: Ozone UV spectroscopy. II. Absorption cross-sections and temperature dependence, J. Atmos. Chem., 21, 263–273, https://doi.org/10.1007/BF00696758, 1995.

Mann, G. W., Carslaw, K. S., Spracklen, D. V., Ridley, D. A., Manktelow, P. T., Chipperfield, M. P., Pickering, S. J., and Johnson, C. E.: Description and evaluation of GLOMAP-mode: a modal global aerosol microphysics model for the UKCA composition-climate model, Geosci. Model Dev., 3, 519–551, https://doi.org/10.5194/gmd-3-519-2010, 2010.

Manners, J., Thelen, J.-C., Petch, J., Hill, P., and Edwards, J. M.: Two fast radiative transfer methods to improve the temporal sampling of clouds in numerical weather prediction and climate models, Q. J. Roy. Meteorol. Soc., 135, 457–468, https://doi.org/10.1002/qj.956, 2009.

Manners, J., Vosper, S. B., and Roberts, N.: Radiative transfer over resolved topographic features for high-resolution weather prediction, Q. J. Roy. Meteorol. Soc., 138, 720–733, https://doi.org/10.1002/qj.956, 2012.

Manners, J., Edwards, J. M., Hill, P., and Thelen, J.-C.: SOCRATES (Suite Of Community RAdiative Transfer codes based on Edwards and Slingo) Technical Guide, Met Office, UK, available at: https://code.metoffice.gov.uk/trac/socrates (last access: 25 October 2017), 2015.

Maritorena, S., d'Andon, O. H. F., Mangin, A., and Siegel, D. A.: Merged satellite ocean color data products using a bio-optical model: characteristics, benefits and issues, Remote Sens. Environ., 114, 1791–1804, https://doi.org/10.1016/j.rse.2010.04.002, 2010.

Marshall, S. and Oglesby, R. J.: An improved snow hydrology for GCMs. Part 1: snow cover fraction, albedo, grain size, and age, J. Climate, 10, 21–37, https://doi.org/10.1007/BF00210334, 1994.

Marthews, T. R., Dadson, S. J., Lehner, B., Abele, S., and Gedney, N.: High-resolution global topographic index values, Dataset made available under the terms of the Open Government Licence, available at: https://catalogue.ceh.ac.uk/documents/6b0c4358-2bf3-4924-aa8f-793d468b92be (last access: 25 October 2017), 2015.

Martin, G. M., Johnson, D. W., and Spice, A.: The measurement and parameterization of effective radius of droplets in warm stratocumulus clouds, J. Atmos. Sci., 51, 1823–1942, https://doi.org/10.1175/1520-0469(1994)051<1823:TMAPOE>2.0.CO;2, 1994.

Maycock, A. C. and Shine, K. P.: Stratospheric water vapor and climate: sensitivity to the representation in radiation codes, J. Geophys. Res.-Atmos., 117, D13102, https://doi.org/10.1029/2012JD017484, 2012.

McCabe, A. and Brown, A. R.: The role of surface heterogeneity in modelling the stable boundary layer, Bound.-Lay. Meteorol., 122, 517–534, https://doi.org/10.1007/s10546-006-9119-8, 2007.

McNaughton, C. S., Clarke, A. D., Freitag, S., Kapustin, V. N., Kondo, Y., Moteki, N., Sahu, L., Takegawa, N., Schwarz, J. P., Spackman, J. R., Watts, L., Diskin, G., Podolske, J., Holloway, J. S., Wisthaler, A., Mikoviny, T., de Gouw, J., Warneke, C., Jimenez, J., Cubison, M., Howell, S. G., Middlebrook, A., Bahreini, R., Anderson, B. E., Winstead, E., Thornhill, K. L., Lack, D., Cozic, J., and Brock, C. A.: Absorbing aerosol in the troposphere of the Western Arctic during the 2008 ARCTAS/ARCPAC airborne field campaigns, Atmos. Chem. Phys., 11, 7561–7582, https://doi.org/10.5194/acp-11-7561-2011, 2011.

Mercado, L. M., Huntingford, C., Gash, J. H. C., Cox, P. M., and Jogireddy, V.: Improving the representation of radiative interception and photosynthesis for climate model applications, Tellus, B59, 553–565, https://doi.org/10.1111/j.1600-0889.2007.00256.x, 2007.

Miller, D. A. and White, R. A.: A conterminous United States multilayer soil characteristics dataset for regional climate and hydrology modeling, Earth Interact., 2, 1–26, https://doi.org/10.1175/1087-3562(1998)002<0001:ACUSMS>2.3.CO;2, 1998.

Mlawer, E. J., Payne, V. H., Moncet, J.-L., Delamere, J. S., Alvarado, M. J., and Tobin, D. C.: Development and recent evaluation of the MT_CKD model of continuum absorption, Philos. Trans. R. Soc. Lond. A, 370, 2520–2556, https://doi.org/10.1098/rsta.2011.0295, 2012.

Morcrette, C. J.: Improvements to a prognostic cloud scheme through changes to its cloud erosion parametrization, Atmos. Sci. Let., 13, 95–102, https://doi.org/10.1002/asl.374, 2012.

Morgenstern, O., Braesicke, P., O'Connor, F. M., Bushell, A. C., Johnson, C. E., Osprey, S. M., and Pyle, J. A.: Evaluation of the new UKCA climate-composition model – Part 1: The stratosphere, Geosci. Model Dev., 2, 43–57, https://doi.org/10.5194/gmd-2-43-2009, 2009.

Mulcahy, J. P., Jones, C., Sellar, A., Johnson, B., Boutle, I. A., Jones, A., Andrews, T., Rumbold, S. T., Mollard, J., Bellouin, N., Johnson, C. E., Williams, K. D., Grosvenor, D. P., and McCoy, D. T.: Improved Aerosol Processes and Effective Radiative Forcing in HadGEM3 and UKESM1, JAMES, 10, 2786–2805, https://doi.org/10.1029/2018MS001464, 2018.

Muller, J.-P., López, G., Watson, G., Shane, N., Kennedy, T., Yuen, P., Lewis, P., Fischer, J., Guanter, L., Domench, C., Preusker, R., North, P., Heckel, A., Danne, O., Krämer, U., Zühlke, M., Brockmann, C., and Pinnock, S.: The ESA GlobAlbedo project for mapping the Earth's land surface albedo for 15 years from European sensors, presented at IEEE Geoscience and Remote Sensing Symposium (IGARSS) 2012, IEEE, Munich, Germany, 22–27 July 2012, available at: http://www.mssl.ucl.ac.uk/~pcy/papers/Muller-GlobAlbedo-abstractV4.pdf (last access: 25 October 2017), 2012.

Nachtergaele, F., van Velthuizen, H., Verelst, L., Batjes, N., Dijkshoorn, K., van Engelen, V., Fischer, G., Jones, A., Montanarella, L., Petri, M., Prieler, S., Teixeira, E., Wiberg, D., and Shi, X.: Harmonized World Soil Database (version 1.0), FAO, Rome, Italy and IIASA, Laxenburg, Austria, 2008.

Neggers, R. A. J., Ackerman, A. S., Angevine, W. M., Bazile, E., Beau, I., Blossey, P. N., Boutle, I. A., de Bruijn, C., Cheng, A., van der Dussen, J., Fletcher, J., Dal Gesso, S., Jam, A., Kawai, H., Cheedela, S. K., Larson, V. E., Lefebvre, M.-P., Lock, A. P., Meyer, N. R., de Roode, S. R., de Rooy, W., Sandu, I., Xiao, H., and Xu, K.-M.: Single-Column Model Simulations of Subtropical Marine Boundary-Layer Cloud Transitions Under Weakening Inversions, JAMES, 9, 2385–2412, https://doi.org/10.1002/2017MS001064, 2017.

Nicholls, S.: The dynamics of stratocumulus: Aircraft observations and comparisons with a mixed layer model, Q. J. Roy. Meteorol. Soc., 110, 783–820, https://doi.org/10.1002/qj.49711046603, 1984.

O'Connor, F. M., Johnson, C. E., Morgenstern, O., Abraham, N. L., Braesicke, P., Dalvi, M., Folberth, G. A., Sanderson, M. G., Telford, P. J., Voulgarakis, A., Young, P. J., Zeng, G., Collins, W. J., and Pyle, J. A.: Evaluation of the new UKCA climate-composition model – Part 2: The troposphere, Geosci. Model Dev., 7, 41–91, https://doi.org/10.5194/gmd-7-41-2014, 2014.

Oki, T.: Validating the runoff from LSP-SVAT models using a global river routing network by one degree mesh, in: AMS 13th Conference on Hydrology, Long Beach, California, 2–7 February 1997, 319–322, 1997.

Oki, T. and Sud, Y. C.: Design of Total Runoff Integrating Pathways (TRIP) – A global river channel network, Earth Interact., 2, 1–36, https://doi.org/10.1175/1087-3562(1998)002<0001:DOTRIP>2.3.CO;2, 1998.

Oreopoulos, L. and Cahalan, R. F.: Cloud inhomogeneity from MODIS, J. Climate, 18, 5110–5124, https://doi.org/10.1175/JCLI3591.1, 2005.

Oreopoulos, L., Mlawer, E., Delamere, J., Shippert, T., Cole, J., Fomin, B., Iacono, M., Jin, Z., Li, J., Manners, J., Räisänen, P., Rose, F., Zhang, Y., Wilson, M. J., and Rossow, W. B.: The continual intercomparison of radiation codes: results from phase I, J. Geophys. Res.-Atmos., 117, D06118, https://doi.org/10.1029/2011JD016821, 2012.

Palmer, T. N., Buizza, R., Doblas-Reyes, F. J., Jung, T., Leutbecher, M., Shutts, G., Steinheimer, M., and A, A. W.: Stochastic parametrization and model uncertainty, Tech. Rep. 1, ECMWF RD Technical Memorandum, ECMWF, Reading, UK, 2009.

Pearson, K. J., Lister, G. M. S., Birch, C. E., Allan, R. P., Hogan, R. J., and Woolnough, S. J.: Modelling the diurnal cycle of tropical convection across the "grey zone", Q. J. Roy. Meteorol. Soc., 140, 491–499, https://doi.org/10.1002/qj.2145, 2014.

Pincus, R., Mlawer, E. J., Oreopoulos, L., Ackerman, A. S., Baek, S., Brath, M., Buehler, S. A., Cady-Pereira, K. E., Cole, J. N. S., Dufresne, J.-L., Kelley, M., Li, J., Manners, J., Paynter, D. J., Roehrig, R., Sekiguchi, M., and Schwarzkopf, D. M.: Radiative flux and forcing parameterization error in aerosol-free clear skies, Geophys. Res. Lett., 42, 5485–5492, https://doi.org/10.1002/2015GL064291, 2015.

Plant, R. S. and Craig, G. C.: A stochastic parameterization for deep convection based on equilibrium statistics, J. Atmos. Sci., 65, 87–105, https://doi.org/10.1175/2007JAS2263.1, 2008.

Ptashnik, I. V., McPheat, R. A., Shine, K. P., Smith, K. M., and Williams, R. G.: Water vapor self-continuum absorption in near-infrared windows derived from laboratory measurements, J. Geophys. Res.-Atmos., 116, D16305, https://doi.org/10.1029/2011JD015603, 2011.

Ptashnik, I. V., McPheat, R. A., Shine, K. P., Smith, K. M., and Williams, R. G.: Water vapour foreign-continuum absorption in near-infrared windows from laboratory measurements, Philos. Trans. R. Soc. Lond. A, 370, 2557–2577, https://doi.org/10.1098/rsta.2011.0218, 2012.

Quinn, P. K. and Bates, T. S.: Regional aerosol properties: Comparisons of boundary layer measurements from ACE 1, ACE 2, Aerosols99, INDOEX, ACE Asia, TARFOX, and NEAQS, J. Geophys. Res., 110, D14202, https://doi.org/10/1024/2004JD004755, 2005.

Quinn, P. K., Bates, T. S., Schulz, K. S., Coffman, D. J., Frossard, A. A., Russell, L. M., Keene, W. C., and Kieber, D. J.: Contribution of sea surface carbon pool to organic matter enrichment in sea spray aerosol, Nat. Geosci., 7, 228–232, https://doi.org/10.1038/ngeo2092, 2014.

Quinn, P. K., Bates, T. S., Coffman, D., Onasch, T. B., Worsnop, D., Baynard, T., de Gouw, J. A., Goldan, P. D., Kuster, W. C., Williams, E., Roberts, J. M., Lerner, B., Stohl, A., Pettersson, A., and Lovejoy, E. R.: Impacts of sources and aging

on submicrometer aerosol properties in the marine boundary layer across the Gulf of Maine, J. Geophys. Res., 111, D23S36, https://doi.org/10.1029/2006JD007582, 2006.

Ramanathan, V., Crutzen, P. J., Lelieveld, J., Mitra, A. P., Althausen, D., Anderson, J., Andreae, M. O., Cantrell, W., Cass, G. R., Chung, C. E., Clarke, A. D., Coakley, J. A., Collins, W. D., Conant, W. C., Dulac, F., Heintzenberg, J., Heymsfield, A. J., Holben, B., Howell, S., Hudson, J., Jayaraman, A., Kiehl, J. T., Krishnamurti, T. N., Lubin, D., McFarquhar, G., Novakov, T., Ogren, J. A., Podgorny, I. A., Prather, K., Priestley, K., Prospero, J. M., Quinn, P. K., Rajeev, K., Rasch, P., Rupert, S., Sadourny, R., Satheesh, S. K., Shaw, G. E., Sheridan, P., and Valero, F. P. J.: Indian Ocean Experiment: An integrated analysis of the climate forcing and effects of the great Indo-Asian haze, J. Geophys. Res.-Atmos., 106, 28371–28398, https://doi.org/10.1029/2001JD900133, 2001.

Raper, J. L., Kleb, M. M., Jacob, D. J., Davis, D. D., Newell, R. E., Fuelberg, H. E., Bendura, R. J., Hoell, J. M., and McNeal, R. J.: Pacific Exploratory Mission in the Tropical Pacific: PEM-Tropics B, March–April 1999, J. Geophys. Res.-Atmos. 106, 32401–32425, https://doi.org/10.1029/2000JD900833, 2001.

Rashid, H. A. and Hirst, A. C.: Mechanisms of improved rainfall simulation over the Maritime Continent due to increased horizontal resolution in an AGCM, Clim. Dynam., 49, 1747–1764, https://doi.org/10.1007/s00382-016-3413-z, 2017.

Rauber, R. M., Stevens, B., Ochs, H. T., Knight, C., Albrecht, B. A., Blyth, A. M., Fairall, C. W., Jensen, J. B., Lasher-Trapp, S. G., Mayol-Bracero, O. L., Vali, G., Anderson, J. R., Baker, B. A., Bandy, A. R., Burnet, E., Brenguier, J. L., Brewer, W. A., Brown, P. R. A., Chuang, P., Cotton, W. R., Di Girolamo, L., Geerts, B., Gerber, H., Goke, S., Gomes, L., Heikes, B. G., Hudson, J. G., Kollias, P., Lawson, R. P., Krueger, S. K., Lenschow, D. H., Nuijens, L., O'Sullivan, D. W., Rilling, R. A., Rogers, D. C., Siebesma, A. P., Snodgrass, E., Stith, J. L., Thornton, D. C., Tucker, S., Twohy, C. H., and Zuidema, P.: Rain in shallow cumulus over the ocean: the RICO campaign, B. Am. Meteorol. Soc., 88, 1912–1928, https://doi.org/10.1175/BAMS-88-12-1912, 2007.

Reddington, C. L., Carslaw, K. S., Stier, P., Schutgens, N., Coe, H., Liu, D., Allan, J., Browse, J., Pringle, K. J., Lee, L. A., Yoshioka, M., Johnson, J. S., Regayre, L. A., Spracklen, D. V., Mann, G. W., Clarke, A., Hermann, M., Henning, S., Wex, H., Kristensen, T. B., Leaitch, W. R., Pöschl, U., Rose, D., Andreae, M. O., Schmale, J., Kondo, Y., Oshima, N., Schwarz, J. P., Nenes, A., Anderson, B., Roberts, G. C., Snider, J. R., Leck, C., Quinn, P. K., Chi, X., Ding, A., Jimenez, J. L., and Zhang, Q.: The Global Aerosol Synthesis and Science Project (GASSP): Measurements and modeling to reduce uncertainty, B. Am. Meteorol. Soc., 98, 1857–1877, https://doi.org/10.1175/BAMS-D-15-00317.1, 2017.

Redelsperger, J.-L., Guichard, F., and Mondon, S.: A parametrization of mesoscale enhancement of surface fluxes for large-scale models, J. Climate, 13, 402–421, https://doi.org/10.1175/1520-0442(2000)013<0402:APOMEO>2.0.CO;2, 2000.

Rooney, G. G. and Jones, I. D.: Coupling the 1-D lake model FLake to the community land-surface model JULES, Boreal Env. Res., 15, 501–512, 2010.

Rothman, L. S., Gordon, I. E., Babikov, Y., Barbe, A., Chris Benner, D., Bernath, P. F., Birk, M., Bizzocchi, L., Boudon, V., Brown, L. R., Campargue, A., Chance, K., Cohen, E. A., Coudert, L. H., Devi, V. M., Drouin, B. J., Fayt, A., Flaud, J.-M., Gamache, R. R., Harrison, J. J., Hartmann, J.-M., Hill, C., Hodges, J. T., Jacquemart, D., Jolly, A., Lamouroux, J., Le Roy, R. J., Li, G., Long, D. A., Lyulin, O. M., Mackie, C. J., Massie, S. T., Mikhailenko, S., Müller, H. S. P., Naumenko, O. V., Nikitin, A. V., Orphal, J., Perevalov, V., Perrin, A., Polovtseva, E. R., Richard, C., Smith, M. A. H., Starikova, E., Sung, K., Tashkun, S., Tennyson, J., Toon, G. C., Tyuterev, V. G., and Wagner, G.: The HITRAN2012 molecular spectroscopic database, J. Quant. Spectrosc. Radiat. Transfer, 130, 4–50, https://doi.org/10.1016/j.jqsrt.2013.07.002, 2013.

Ryerson, T. B., Andrews, A. E., Angevine, W. M., Bates, T. S., Brock, C. A., Cairns, B.,Cohen, R. C., Cooper, O. R., de Gouw, J. A., Fehsenfeld, F. C., Ferrare, R. A., Fischer, M. L., Flagan, R. C., Goldstein, A. H., Hair, J. W., Hardesty, R. M., Hostetler, C. A., Jimenez, J. L., Langford, A. O., McCauley, E., McKeen, S. A., Molina, L. T., Nenes, A., Oltmans, S. J., Parrish, D. D., Pederson, J. R., Pierce, R. B., Prather, K., Quinn, P. K., Seinfeld, J. H., Senff, C. J., Sorooshian, A., Stutz, J., Surratt, J. D., Trainer, M., Volkamer, R., Williams, E. J., and Wofsy, S. C.: The 2010 California Research at the Nexus of air quality and climate change (CalNex) field study, J. Geophys. Res.-Atmos., 118, 5830–5866, https://doi.org/10.1002/jgrd.50331, 2013.

Samanta, A., Ganguly, S., Schull, M. A., Shabanov, N. V., Knyazikhin, Y., and Myneni, R. B.: Collection 5 MODIS LAI/FPAR Products, Presented at AGU Fall Meeting, San Francisco, USA, 15–19 December, 2008, 2012.

Sanchez, C., Williams, K. D., Shutts, G. J., McDonald, R. E., Hinton, T. J., Senior, C. A., and Wood, N.: Towards the development of a robust model hierarchy: investigation of dynamical limitations at low resolution and possible solutions, Q. J. Roy. Meteorol. Soc., 139, 75–84, https://doi.org/10.1002/qj.1971, 2013.

Sanchez, C., Williams, K. D., and Collins, M.: Improved stochastic physics schemes for global weather and climate models, Q. J. Roy. Meteorol. Soc., 142, 147–159, https://doi.org/10.1002/qj.2640, 2016.

Sayer, A. M., Munchak, L. A., Hsu, N. C., Levy, R. C., Bettenhausen, C., and M.-J., J.: MODIS Collection 6 aerosol products: Comparison between Aqua's e-Deep Blue, Dark Target, and "merged" data sets, and usage recommendations, J. Geophys. Res., 119, 13,965–13,989, https://doi.org/10.1002/2014JD022453, 2014.

Scaife, A. A., Butchart, N., Warner, C. D., and Swinbank, R.: Impact of a spectral gravity wave parametrization on the stratosphere in the Met Office Unified Model, J. Atmos. Sci., 59, 1473–1489, https://doi.org/10.1175/1520-0469(2002)059<1473:IOASGW>2.0.CO;2, 2002.

Schmidt, G. A., Bader, D., Donner, L. J., Elsaesser, G. S., Golaz, J.-C., Hannay, C., Molod, A., Neale, R. B., and Saha, S.: Practice and philosophy of climate model tuning across six US modeling centers, Geosci. Model Dev., 10, 3207–3223, https://doi.org/10.5194/gmd-10-3207-2017, 2017.

Schutgens, N., Tsyro, S., Gryspeerdt, E., Goto, D., Weigum, N., Schulz, M., and Stier, P.: On the spatio-temporal representativeness of observations, Atmos. Chem. Phys., 17, 9761–9780, https://doi.org/10.5194/acp-17-9761-2017, 2017.

Sellers, P. J.: Canopy reflectance, photosynthesis and reflection, Int. J. Rem. Sens., 6, 1335–1372, https://doi.org/10.1080/01431168508948283, 1985.

Serdyuchenko, A., Gorshelev, V., Weber, M., Chehade, W., and Burrows, J. P.: High spectral resolution ozone absorption cross-sections – Part 2: temperature dependence, Atmos. Meas. Tech., 7, 625–636, https://doi.org/10.5194/amt-7-625-2014, 2014.

Shonk, J. K. P. and Hogan, R. J.: Effect of improving representation of horizontal and vertical cloud structure on the Earth's radiation budget. Part II: The global effects, Q. J. Roy. Meteorol. Soc., 136, 1205–1215, https://doi.org/10.1002/qj.646, 2010.

Slater, A. G., Lawrence, D. M., and Koven, C. D.: Process-level model evaluation: A snow and heat transfer metric, The Cryosphere, 11, 989–996, https://doi.org/10.5194/tc-11-989-2017, 2017.

Slingo, J. M.: The development and verification of a cloud prediction scheme for the ECMWF model, Q. J. Roy. Meteorol. Soc., 113, 899–927, https://doi.org/10.1002/qj.49711347710, 1987.

Smith, S. D.: Coefficients for sea surface wind stress, heat flux, and wind profiles as a function of wind speed and temperature, J. Geophys. Res., 93, 15467–15472, https://doi.org/10.1029/JC093iC12p15467, 1988.

Smith, R. N. B.: A scheme for predicting layer cloud and their water content in a general circulation model, Q. J. Roy. Meteorol. Soc., 116, 435–460, https://doi.org/10.1002/qj.49711649210, 1990.

Soloviev, A. V., Lukas, R., Donelan, M. A., Haus, B. K., and Ginis, I.: The air-sea interface and surface stress under tropical cyclones, Sci. Rep., 4, 5306, https://doi.org/10.1038/srep0536, 2014.

Stephens, G. L., L'Ecuyer, T., Forbes, R., Gettlemen, A., Golaz, J.-C., Bodas-Salcedo, A., Suzuki, K., Gabriel, P., and Haynes, J.: Dreary state of precipitation in global models, J. Geophys. Res., 115, D24211, https://doi.org/10.1029/2010JD014532, 2010.

Stirling, A. J. and Stratton, R. A.: Entrainment processes in the diurnal cycle of deep convection over land, Q. J. Roy. Meteorol. Soc., 138, 1135–1149, https://doi.org/10.1002/qj.1868, 2012.

Stratton, R. A., Stirling, A., and Derbyshire, S.: Changes and developments to Convective Momentum Transport (CMT) parametrization based on analysis of CRM and SCM, Tech. Rep. 530, Forecsating R&D, Met Office, Exeter, UK, 2009.

Suselj, K., Teixeira, J., and Matheou, G.: Eddy diffusivity/mass flux and shallow cumulus boundary layer: an updraft PDF multiple mass flux scheme, J. Atmos. Sci., 69, 1513–1533, https://doi.org/10.1175/JAS-D-11-090.1, 2012.

Taillandier, A.-S., Domine, F., Simpson, W. R., Sturm, M., and Douglas, T. A.: Rate of decrease of the specific surface area of dry snow: Isothermal and temperature gradient conditions, J. Geophys. Res.-Earth Surf., 112, F03003, https://doi.org/10.1029/2006JF000514, 2007.

Takahama, S., Schwartz, R. E., Russell, L. M., Macdonald, A. M., Sharma, S., and Leaitch, W. R.: Organic functional groups in aerosol particles from burning and non-burning forest emissions at a high-elevation mountain site, Atmos. Chem. Phys., 11, 6367–6386, https://doi.org/10.5194/acp-11-6367-2011, 2011.

Tennant, W. J., Shutts, G. J., Arribas, A., and Thompson, S. A.: Using a stochastic kinetic energy backscatter scheme to improve MOGREPS probabilistic forecast skill, Mon. Weather Rev., 139, 1190–1206, https://doi.org/10.1175/2010MWR3430.1, 2011.

Tiedtke, M.: Representation of clouds in large-scale models, Mon. Weather Rev., 121, 3040–3061, https://doi.org/10.1175/1520-0493(1993)121<3040:ROCILS>2.0.CO;2, 1993.

Tomassini, L., Parker, D. J., Stirling, A., Bain, C., Senior, C., and Milton, S.: The interaction between moist diabatic processes and the atmospheric circulation in African Easterly Wave propagation, Q. J. Roy. Meteorol. Soc., 143, 3207–3227, https://doi.org/10.1002/qj.3173, 2017.

Ujiie, M., Walters, D., Cameron, J., Bell, W., and Eyre, J.: Systematic errors in the Met Office's global analysis and their influence on initial forecast error growth, Tech. rep., Forecsating R&D, Met Office, Exeter, UK, 2017a.

Ujiie, M., Willet, M., Walters, D., Bushell, A., and Milton, S.: An improvement to the melting of precipitation in the Met Office Unified Model's convection scheme and its impact on the tropical performance, Tech. rep., Forecsating R&D, Met Office, Exeter, UK, 2017b.

Untch, A. and Simmons, A. J.: Increased stratospheric resolution in the ECMWF forecasting system, ECMWF Newsletter 82, ECMWF, Reading, UK, 1999.

Uppala, S. M., Kållberg, P. W., Simmons, A. J., Andrae, U., V. Da Costa Bechtold, Fiorino, M., Gibson, J. K., Haseler, J., Hernandez, A., Kelly, G. A., Li, X., Onogi, K., Saarinen, S., Sokka, N., Allan, R. P., Andersson, E., Arpe, K., Balmaseda, M. A., Beljaars, A. C. M., van de Berg, L., Bidlot, J., Bormann, N., Caires, S., Chevallier, F., Dethof, A., Dragosavac, M., Fisher, M., Fuentes, M., Hagemann, S., Hólm, E., Hoskins, B. J., Isaksen, L., Janssen, P. A. E. M., Jenne, R., Mcnally, A. P., Mahfouf, J.-F., Morcrette, J.-J., Rayner, N. A., Saunders, R. W., Simon, P., Sterl, A., Trenberth, K. E., Untch, A., Vasiljevic, D., Viterbo, P., and Woollen, J.: The ERA-40 re-analysis, Q. J. Roy. Meteorol. Soc., 131, 2961–3012, https://doi.org/10.1256/qj.04.176, 2005.

Vakkari, V., Beukes, J. P., Laakso, H., Mabaso, D., Pienaar, J. J., Kulmala, M., and Laakso, L.: Long-term observations of aerosol size distributions in semi-clean and polluted savannah in South Africa, Atmos. Chem. Phys., 13, 1751–1770, https://doi.org/10.5194/acp-13-1751-2013, 2013.

van der Werf, G. R., Randerson, J. T., Giglio, L., Collatz, G. J., Mu, M., Kasibhatla, P. S., Morton, D. C., DeFries, R. S., Jin, Y., and van Leeuwen, T. T.: Global fire emissions and the contribution of deforestation, savanna, forest, agricultural, and peat fires (1997–2009), Atmos. Chem. Phys., 10, 11707–11735, https://doi.org/10.5194/acp-10-11707-2010, 2010.

van Genuchten, M. T.: A closed-form equation for predicting the hydraulic conductivity of unsaturated soils, Soil Sci. Soc. Am. J., 44, 892–898, https://doi.org/10.2136/sssaj1980.03615995004400050002x, 1980.

Van Weverberg, K., Boutle, I. A., Morcrette, C. J., and Newsom, R. K.: Towards retrieving critical relative humidity from ground-based remote-sensing observations, Q. J. Roy. Meteorol. Soc., 142, 2867–2881, https://doi.org/10.1002/qj.2874, 2016.

Vionnet, V., Brun, E., Morin, S., Boone, A., Faroux, S., Moigne, P. L., Martin, E., and Willemet, J.-M.: The detailed snowpack scheme Crocus and its implementation in SURFEX v7.2, Geosci. Model Dev., 5, 773–791, https://doi.org/10.5194/gmd-5-773-2012, 2012.

Vosper, S. B.: Mountain waves and wakes generated by South Georgia: implications for drag parametrization, Q. J. Roy. Meteorol. Soc., 141, 2813–2827, https://doi.org/10.1002/qj.2566, 2015.

Walters, D., Boutle, I., Brooks, M., Melvin, T., Stratton, R., Vosper, S., Wells, H., Williams, K., Wood, N., Allen, T., Bushell, A., Copsey, D., Earnshaw, P., Edwards, J., Gross, M., Hardiman, S., Harris, C., Heming, J., Klingaman, N., Levine, R., Manners, J., Martin, G., Milton, S., Mittermaier, M., Morcrette, C., Riddick, T., Roberts, M., Sanchez, C., Selwood, P., Stirling, A., Smith, C., Suri, D., Tennant, W., Vidale, P. L., Wilkinson, J., Willett, M., Woolnough, S., and Xavier, P.: The Met Office Unified Model Global Atmosphere 6.0/6.1 and JULES Global Land 6.0/6.1 configurations, Geosci. Model Dev., 10, 1487–1520, https://doi.org/10.5194/gmd-10-1487-2017, 2017.

Walters, D. N., Best, M. J., Bushell, A. C., Copsey, D., Edwards, J. M., Falloon, P. D., Harris, C. M., Lock, A. P., Manners, J. C., Morcrette, C. J., Roberts, M. J., Stratton, R. A., S. Webster, J. M. W., Willett, M. R., Boutle, I. A., Earnshaw, P. D., Hill, P. G., MacLachlan, C., Martin, G. M., Moufouma-Okia, W., Palmer, M. D., Petch, J. C., Rooney, G. G., Scaife, A. A., and Williams, K. D.: The Met Office Unified Model Global Atmosphere 3.0/3.1 and JULES Global Land 3.0/3.1 configurations, Geosci. Model Dev., 4, 919–941, https://doi.org/10.5194/gmd-4-919-2011, 2011.

Walters, D. N., Williams, K. D., Boutle, I. A., Bushell, A. C., Edwards, J. M., Field, P. R., Lock, A. P., Morcrette, C. J., Stratton, R. A., Wilkinson, J. M., Willett, M. R., Bellouin, N., Bodas-Salcedo, A., Brooks, M. E., Copsey, D., Earnshaw, P. D., Harris, C. M., Levine, R. C., MacLachlan, C., Manners, J. C., Martin, G. M., Milton, S. F., Palmer, M. D., Roberts, M. J., Rodríguez, J. M., Tennant, W. J., and Vidale, P.: The Met Office Unified Model Global Atmosphere 4.0 and JULES Global Land 4.0 configurations, Geosci. Model Dev., 7, 361–386, https://doi.org/10.5194/gmd-7-361-2014, 2014.

Wang, W., Rood, M. J., Carrico, C. M., Covert, D. S., Quinn, P. K., and Bates, T. S.: Aerosol optical properties along the northeast coast of North America during the New England Air Quality Study – Intercontinental Transport and Chemical Transformation 2004 campaign and the influence of aerosol composition, J. Geophys. Res.-Atmos., 112, D10, https://doi.org/10.1029/2006JD007579, 2007.

Warner, C. D. and McIntyre, M. E.: An ultrasimple spectral parametrization for nonorographic gravity waves, J. Atmos. Sci., 58, 1837–1857, https://doi.org/10.1175/1520-0469(2001)058<1837:AUSPFN>2.0.CO;2, 2001.

Weisheimer, A., Palmer, T. N., and Doblas-Reyes, F. J.: Assessment of representations of model uncertainty in monthly and seasonal forecast ensembles, Geophys. Res. Lett., 38, L16703, https://doi.org/10.1029/2011GL048123, 2011.

Weisheimer, A., Cortia, S., Palmer, T., and Vitart, F.: Addressing model error through atmospheric stochastic physical parametrizations: impact on the coupled ECMWF seasonal forecasting system, Philos. Trans. R. Soc. Lond. A, 372, 20130290, https://doi.org/10.1098/rsta.2013.0290, 2014.

Wentz, F. J. and Spencer, R. W.: SSM/I rain retrievals within a unified all-weather ocean algorithm, J. Atmos. Sci., 55, 1613–1627, https://doi.org/10.1175/1520-0469(1998)055<1613:SIRRWA>2.0.CO;2, note: SSM/I data are produced by Remote Sensing Systems and sponsored by the NASA Earth Science MEaSUREs DISCOVER Project, available at: http://www.remss.com (last access: 25 October 2017), 1998.

West, R. E. L., Stier, P., Jones, A., Johnson, C. E., Mann, G. W., Bellouin, N., Partridge, D. G., and Kipling, Z.: The importance of vertical velocity variability for estimates of the in direct aerosol effects, Atmos. Chem. Phys., 14, 6369–6393, https://doi.org/10.5194/acp-14-6369-2014, 2014.

Williams, K. D. and Bodas-Salcedo, A.: A multi-diagnostic approach to cloud evaluation, Geosci. Model Dev., 10, 2547–2566, https://doi.org/10.5194/gmd-10-2547-2017, 2017.

Williams, K. D., Bodas-Salcedo, A., Déqué, M., Fermepin, S., Medeiros, B., Watanabe, M., Jakob, C., Klein, S. A., Senior, C. A., and Williamson, D. L.: The transpose-AMIP ii experiment and its application to the understanding of Southern Ocean cloud biases in climate models, J. Climate, 26, 3258–3274, https://doi.org/10.1175/JCLI-D-12-00429.1, 2013.

Williams, K. D., Copsey, D., Blockley, E. W., Bodas-Salcedo, A., Calvert, D., Comer, R., Davis, P., Graham, T., Hewitt, H. T., Hill, R., Hyder, P., Ineson, S., Johns, T. C., Keen, A. B., Lee, R. W., Megann, A., Milton, S. F., Rae, J. G. L., Roberts, M. J., Scaife, A. A., Schiemann, R., Storkey, D., Thorpe, L., Watterson, I. G., Walters, D. N., West, A., Wood, R. A., Woollings, T., and Xavier, P. K.: The Met Office Global Coupled model 3.0 and 3.1 (GC3.0 and GC3.1) configurations, JAMES, 10, 357–380, https://doi.org/10.1002/2017MS001115, 2018.

Wilson, D. R. and Ballard, S. P.: A microphysically based precipitation scheme for the UK Meteorological Office Unified Model, Q. J. Roy. Meteorol. Soc., 125, 1607–1636, https://doi.org/10.1002/qj.49712555707, 1999.

Wilson, D. R., Bushell, A. C., Kerr-Munslow, A. M., Price, J. D., and Morcrette, C. J.: PC2: A prognostic cloud fraction and condensation scheme. I: Scheme description, Q. J. Roy. Meteorol. Soc., 134, 2093–2107, https://doi.org/10.1002/qj.333, 2008a.

Wilson, D. R., Bushell, A. C., Kerr-Munslow, A. M., Price, J. D., Morcrette, C. J., and Bodas-Salcedo, A.: PC2: A prognostic cloud fraction and condensation scheme. II: Climate model simulations, Q. J. Roy. Meteorol. Soc., 134, 2109–2125, https://doi.org/10.1002/qj.332, 2008b.

Wlasak, M. A. and Cullen, M. J. P.: Modelling static 3-D spatial background error covariances – the effect of vertical and horizontal transform order, Adv. Sci. Res., 11, 63–67, https://doi.org/10.5194/asr-11-63-2014, 2014.

Wood, N. and Mason, P. J.: The pressure force induced by neutral, turbulent flow over hills, Q. J. Roy. Meteorol. Soc., 127, 759–777, https://doi.org/10.1002/qj.49711951402, 1993.

Wood, N., Diamantakis, M., and Staniforth, A.: A monotonically-damping second-order-accurate unconditionally-stable numerical scheme for diffusion, Q. J. Roy. Meteorol. Soc., 133, 1559–1573, https://doi.org/10.1002/qj.116, 2007.

Wood, N., Staniforth, A., White, A., Allen, T., Diamantakis, M., Gross, M., Melvin, T., Smith, C., Vosper, S., Zerroukat, M., and Thuburn, J.: An inherently mass-conserving semi-implicit semi-Lagrangian discretization of the deep-atmosphere global non-hydrostatic equations, Q. J. Roy. Meteorol. Soc., 140, 1505–1520, https://doi.org/10.1002/qj.2235, 2014.

Wood, R., Mechoso, C. R., Bretherton, C. S., Weller, R. A., Huebert, B., Straneo, F., Albrecht, B. A., Coe, H., Allen, G., Vaughan, G., Daum, P., Fairall, C., Chand, D., Gallardo Klenner, L., Garreaud, R., Grados, C., Covert, D. S., Bates, T. S., Krejci, R., Russell,

L. M., de Szoeke, S., Brewer, A., Yuter, S. E., Springston, S. R., Chaigneau, A., Toniazzo, T., Minnis, P., Palikonda, R., Abel, S. J., Brown, W. O. J., Williams, S., Fochesatto, J., Brioude, J., and Bower, K. N.: The VAMOS Ocean-Cloud-Atmosphere-Land Study Regional Experiment (VOCALS-REx): goals, platforms, and field operations, Atmos. Chem. Phys., 11, 627–654, https://doi.org/10.5194/acp-11-627-2011, 2011.

Woodward, S.: Mineral dust in HadGEM2, Tech. Rep. 87, Hadley Centre, Met Office, Exeter, UK, 2011.

Xie, P. and Arkin, P. A.: Global precipitation: A 17-year monthly analysis based on gauge observations, satellite estimates, and numerical model outputs, B. Am. Meteorol. Soc., 78, 2539–2558, https://doi.org/10.1175/1520-0477(1997)078<2539:GPAYMA>2.0.CO;2, 1997.

Yen, Y.-C.: Review of the thermal properties of snow, ice and sea ice, Tech. Rep. 81-10, Cold Regions Research and Engineering Laboratory, Hanover, NH, 1981.

Zerroukat, M.: A simple mass conserving semi-Lagrangian scheme for transport problems, J. Comput. Phys., 229, 9011–9019, https://doi.org/10.1016/j.jcp.2010.08.017, 2010.

Zerroukat, M. and Allen, T.: On the monotonic and conservative transport on overset/Yin-Yang grids, J. Comput. Phys., 302, 285–299, https://doi.org/10.1016/j.jcp.2015.09.006, 2015.

Zhang, Y. and Klein, S. A.: Factors controlling the vertical extent of fair-weather shallow cumulus clouds over land: investigation of diurnal-cycle observations collected at the ARM Southern Great Plains site, J. Atmos. Sci., 70, 1297–1315, https://doi.org/10.1175/JAS-D-12-0131.1, 2013.

Zhong, W. and Haigh, J. D.: An efficient and accurate correlated-k parameterization of infrared radiative transfer for troposphere–stratosphere–mesosphere GCMs, Atmos. Sci. Lett., 1, 125–135, https://doi.org/10.1006/asle.2000.0022, 2000.